

DOCTORAL THESIS

Ti-B Based Composites by Spark Plasma Sintering and Selective Laser Melting

Le Liu

TALLINN UNIVERSITY OF TECHNOLOGY
DOCTORAL THESIS
47/2021

**Ti-B Based Composites by Spark
Plasma Sintering and Selective
Laser Melting**

LE LIU



TALLINN UNIVERSITY OF TECHNOLOGY

School of Engineering

Department of Mechanical and Industrial Engineering

This dissertation was accepted for the defence of the degree 10/09/2021

Supervisor:

Prof. Irina Hussainova
School of Engineering
Tallinn University of Technology
Tallinn, Estonia

Co-supervisor:

Dr. Sofiya Aydiyanyan
School of Engineering
Tallinn University of Technology
Tallinn, Estonia

Opponents:

Prof. Olga Kurapova
Institute of Chemistry
Saint Petersburg University
Saint Petersburg, Russia

Dr. Manel Rodríguez Ripoll
Austrian Center of Competence for Tribology
(AC²T) GmbH
Wiener Neustadt, Austria

Defence of the thesis: 14/10/2021, Tallinn

Declaration:

Hereby I declare that this doctoral thesis, my original investigation and achievement, submitted for the doctoral degree at Tallinn University of Technology has not been submitted for doctoral or equivalent academic degree.

Le Liu

signature



European Union
European Regional
Development Fund



Investing
in your future

Copyright: Le Liu, 2021

ISSN 2585-6898 (publication)

ISBN 978-9949-83-744-1 (publication)

ISSN 2585-6901 (PDF)

ISBN 978-9949-83-745-8 (PDF)

Printed by Koopia Niini & Rauam

TALLINNA TEHNIKAÜLIKOOL
DOKTORITÖÖ
47/2021

Sädepaagutus- ja selektiivse lasersulatus- tehnoloogia abil valmistatud Ti-B baasil komposiitmaterjalid

LE LIU



Contents

List of publications	7
Author's contribution to the publications	8
Introduction	9
List of abbreviations	10
1 The review of the literature	11
1.1 Ti-B system	11
1.2 Consolidation of Ti-B based materials	13
1.3 Spark plasma sintering	14
1.4 Powder bed fusion (PBF): Selective laser melting (SLM)	15
1.4.1 Powder bed fusion overview	15
1.4.2 Selective laser melting	16
1.4.3 Power requirements for SLM	17
1.5 Self-propagating high-temperature synthesis	18
1.6 Objectives of the study	19
2 Materials and methods	20
2.1 Feedstock preparation and design of the systems	20
2.1.1 Mechanical mixing	21
2.1.2 SHS of Ti-B, Ti-B-Si composite powders	21
2.2 Spark plasma sintering	21
2.3 Selective laser melting	22
2.4 Characterization	23
3 Results and discussion	24
3.1 Feedstocks	24
3.1.1 Feedstock 1. Commercial Ti and TiB ₂ powder mixtures	24
3.1.2 Feedstock 2. SHS-ed powder from Ti-B for SPS	24
3.1.3 Feedstock 3. SHS-ed powder from Ti-B-Si for SLM	26
3.2 Spark plasma sintering	27
3.2.1 SPS of commercial Ti and TiB ₂ powder mixtures (Feedstock 1)	27
3.2.2 SPS of SHS-ed Ti-B powder (Feedstock 2)	29
3.3 Selective laser melting	31

3.3.1	SLM of commercial Ti and TiB ₂ Powder mixtures (Feedstock 1).....	31
3.3.2	SLM of SHS-ed Ti-B-Si powder (Feedstock 3).....	35
4	Conclusions.....	39
5	Future work.....	41
	Acknowledgements.....	47
	Abstract.....	48
	Lühikokkuvõte.....	49
	List of publications not included in this thesis	50
	Patents	52
	Appendix.....	53
	Curriculum vitae.....	113
	Elulookirjeldus.....	114

List of publications

- I. Kumar, R., Antonov, M., **Liu, L.**, Hussainova, I. (2021). Sliding Wear Performance of in-situ Spark Plasma Sintered Ti-TiB_w Composite at Temperatures up to 900°C. *Wear*, 203663.
- II. Kumar, R., **Liu, L.**, Antonov, M., Ivanov, R., Hussainova, I. (2021). Hot sliding wear of 88wt% TiB-Ti composite from SHS produced powders. *Materials*, 14(5), 1242.
- III. **Liu, L.**, Minasyan, T., Ivanov, R., Aydinyan, S., Hussainova, I. (2020). Selective laser melting of TiB₂-Ti composite with high content of ceramic phase. *Ceramics International*, 46(13), 21128-21135.
- IV. **Liu, L.**, Minasyan, T., Kamboj, N., Aydinyan, S., Hussainova, I. (2020). Bio-inspired TiB₂-TiB-TiN lattices by selective laser melting. *Materials Letters*, 277, 128337.
- V. **Liu, L.**, Aydinyan, S., Minasyan, T., Hussainova, I. (2020). SHS Produced TiB₂-Si Powders for Selective Laser Melting of Ceramic-Based Composite. *Applied Sciences*, 10 (9), 3283.

Author's contribution to the publications

- I. Design of experiments. Powder preparation. Sample sintering. Results analysis.
- II. Design of experiments. Powder preparation. Conducting experiments. Data analysis. Manuscript preparation.
- III. First author. Experimental design. Powder preparation. Conducting experiments. Parameter optimization. Results analysis. Manuscript preparation.
- IV. First author. Experimental design. Powder preparation. 3D modeling. Conducting experiments. Results analysis. Manuscript preparation.
- V. First author. Experimental design. Powder synthesis. Conducting experiments. Parameter optimization. Results analysis. Manuscript preparation.

Introduction

Current demands for tribological and biomedical advances to decrease wear and increase strength encounter with challenges posed by increased use of engineered materials and enhanced functionality. In this context, the preparation of ready availability of “tailored-to-use” materials for consolidation appears to be one of the main issues. The consolidation technologies of the spark plasma sintering (SPS) and selective laser melting (SLM) constantly mature, creating new business values, opening new scientific horizons, conquering new geographies, and hence, requiring input materials with known specifications, which in turn requires reliable methods for powder synthesis [1], [2], [3].

Recently, titanium based materials (titanium-based alloys, titanium-boron based composites, etc.) grab leading position in aviation, automotive, metallurgy and medicine [4], [5], [6]. Due to the outstanding properties of high specific modulus, melting point, excellent hardness, elastic modulus, good thermal and electrical conductivity, abrasion resistance and chemical inertness, titanium-boron based materials drew attention for elevated-temperature structural and wear applications [7]. The manufacturing of the end-products with consistent and predictable properties requires input materials with exact specifications, which in turn requires reliable methods for powder synthesis [8], [9]. In addition, the synthesis and consolidation methods of titanium-boron based materials are decisive for the properties (chemical, physical, mechanical and tribological) and define their application field. The motivation for this work is the urgent need in a knowledge-based design of the powder materials suitable for advanced consolidation, as well as development a technological route for their fabrication. The aim of the thesis is to design, develop and synthesize Ti-B based feedstock well suited for consolidation (SPS/SLM) and subsequently produce the bulk, porous and complex shaped reliable items using the powders developed. From these perspectives the highly productive and energy-efficient self-propagating high-temperature synthesis (SHS) method [10], [11] has precedence over other synthesis methods for the Ti-B based powder preparation, as SHS allows to tailor particle size and morphology by changing the precursors’ ratio, reactor chamber pressure, etc.

Hereby, the following primary tasks were considered: (i) combustion synthesis of Ti-B based composite powder feedstock of special morphology suitable for SPS and SLM processing (ii) SPS processing of ceramic based bulks and SLM processing/optimization of bulk and lattice structures (iii) characterization of phase and microstructure transformation features during SHS, SPS and SLM processes and tribological properties of fabricated SPS compacts at a high temperature.

To fulfill the tasks the phase and microstructure characteristics were examined in accordance with the synthesis and consolidation methods of a material. The main applications of Ti-B products and the further use in modern industrial spheres are detailed. For instance, the composites of TiB_2 -TiB-TiN regarded as potential substitutes to fill and reconstruct bone cavities or areas of bone loss caused by traumas or other disease. In-situ spark plasma sintering of Ti-TiB_w composite lead to the material exhibiting substantially improved sliding wear performance at high temperatures. TiB-Ti composite from SHS produced powder and consolidated via SPS demonstrated enhanced hot sliding wear behavior.

List of abbreviations

Abbreviation	Full Description
AM	Additive manufacturing
BJ	Binder jetting
CAD	Computer aided design
CT	Computed tomography
CoF	Coefficient of friction
CPR-3.5L	Constant pressure reactor -3.5 litres
CS	Combustion synthesis
CTE	Coefficient of thermal expansion
DMLS	Direct metal laser sintering
D10	The diameter defining 10% finer from particle size distribution curve
D50	The diameter defining 50% finer from particle size distribution curve
D90	The diameter defining 90% finer from particle size distribution curve
EBM	Electron beam melting
EDS	Energy Dispersive X-Ray Spectroscopy
HIP	Hot isostatic pressing
HP	Hot pressing
HV	Vickers hardness number
IFT	Indentation fracture toughness
GA	Gas atomization
LC	Laser current
LED	Laser energy density
PA	Plasma atomization
PBF	Powder-bed fusion
PSD	Particle size distribution
sccm	Standard cubic centimeters per minute
SEM	Scanning electron microscope
SHS	Self-propagating high-temperature synthesis
SLM	Selective laser melting
SLS	Selective laser sintering
SPS	Spark plasma sintering
T _{ad}	Adiabatic temperature
T _c	Combustion temperature
T _m	Melting temperature
U _c	Combustion velocity (propagating speed)
U _{cooling}	Cooling speed
U _{heating}	Heating speed
vol.%	Volume percentage
WA	Water atomization
wt.%	Weight percentage
YAG	Yttrium aluminum garnet

1 The review of the literature

Ti-B based composite materials have been garnered the interest of research community owing to their outstanding characteristics, essentially the high melting point, exceptional hardness, good thermal conductivity, high electrical conductivity, wear resistance, chemical stability for high temperature structural and wear applications [7], [12]. They are indispensable for cutting tools, armor materials, jet engine parts, dies, as a control rod material for high temperature nuclear reactors and other high-temperature ceramic components [13]. Moreover, the Ti-B based ceramic composites are believed to be attractive as a weight-saving parts for aerospace applications [14]. Recently, TiB_2 drew attention for elevated-temperature structural applications, metal melting crucibles and electrode materials due to good oxidation resistance (in dry air atmosphere at temperatures up to $1100^\circ C$), as well as for resistance to creep tension during oxidation [15].

However, only very limited successful experiments on consolidation of Ti-B ceramic based composites are available in literature, because of poor sinterability. Moreover, complex shaping of Ti-B based ceramics remains a problem in winning industrial applications because of the brittleness and poor fracture toughness, which makes them difficult to fabricate, especially for producing complex geometry parts. The synthesis and consolidation methods of titanium-boron based materials were certified to be critically decisive for their properties (chemical, physical, and mechanical) and application fields. The presented thesis surveys the possibility of development of bulk and complex geometry Ti-B ceramic based composite materials, with particular emphasis on microstructure features as a function of the technological method of synthesizing material on its consolidation behavior and the preparation of bulk Ti-B ceramic based composite materials for high-temperature tribological applications.

1.1 Ti-B system

In Ti-B system equilibrium compounds found in the phase diagram (Fig. 1.1) are TiB_2 (MB2_C32) and TiB (MB_B27). Their main properties are listed in Table 1.1.

Table 1.1 Properties of TiB_2 and TiB [15], [16].

Material	Density ($g \cdot cm^{-3}$)	Melting point ($^\circ C$)	Hardness (GPa)	Elastic modulus (GPa)	Coefficient of thermal expansion ($^\circ C^{-1}$)	Thermal conductivity ($W \cdot m^{-1} \cdot K^{-1}$)	Electrical conductivity ($\mu\Omega \cdot cm$)
TiB_2	4.52	3230	27	565	7.2×10^{-6}	60-120	10-40
TiB	4.56	2200	18	371	7.15×10^{-6}	-	-

Based on thermodynamic modeling of the Ti-B system [17], at low amounts of titanium (up to 2 moles) in the $xTi + 2B$ mixture, the formation of TiB and TiB_2 is probable, but TiB_2 has higher stability. At higher amounts of titanium (>2 mol) TiB is the only product of the process. Accordingly, the pure TiB_2 formation becomes possible only at the exact stoichiometric composition of initial mixture ($Ti + 2B$). Molten Ti reacts with TiB_2 , and TiB forms from the melt by a peritectic reaction according to $L + TiB_2 \rightarrow TiB$ equation (at $2190 \pm 20^\circ C$).

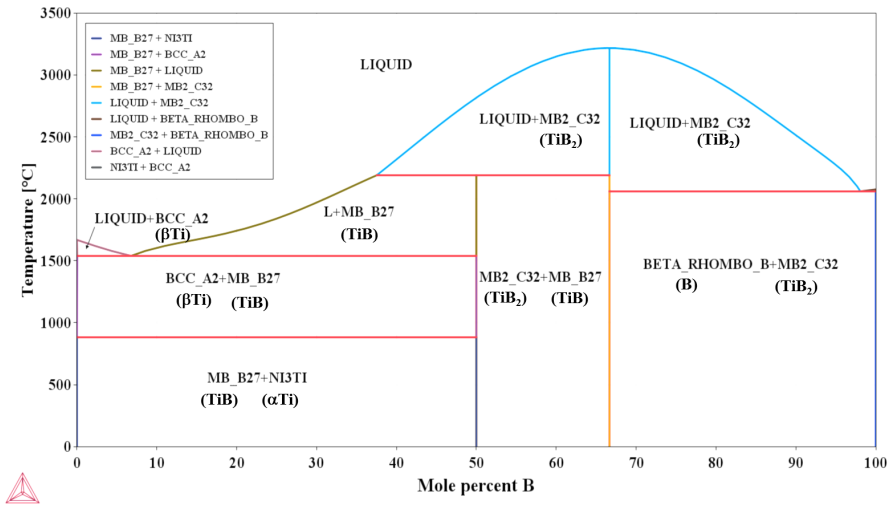


Figure 1.1 Ti-B phase diagram (Calculated by Thermo-Calc software).

The Gibbs free energy of formation (ΔG_f° at 273K) for the reactions in the Ti-B system (solid-solution phase) was calculated using the following relations: $\text{Ti} + \text{B} \rightarrow \text{TiB}$ and $\text{Ti} + 2\text{B} \rightarrow \text{TiB}_2$, which compared with experimental data make about $-160 \text{ kJ}\cdot\text{mol}^{-1}$ and $-275 \text{ kJ}\cdot\text{mol}^{-1}$, respectively (Fig. 1.2). Variation of ΔG against temperature for $\text{Ti} + \text{B} \rightarrow \text{TiB}$ and $\text{Ti} + 2\text{B} \rightarrow \text{TiB}_2$ reactions from 0°C to 3000°C represents gradual increase of ΔG values from -160 up to $-85 \text{ kJ}\cdot\text{mol}^{-1}$ and -275 to $-165 \text{ kJ}\cdot\text{mol}^{-1}$, correspondingly for TiB and TiB_2 formation.

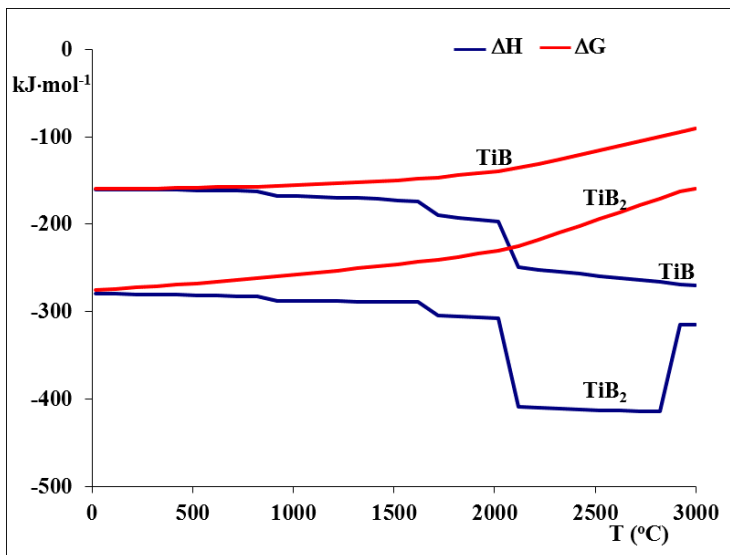


Figure 1.2 Variation of ΔG and ΔH against temperature for $\text{Ti} + \text{B} \rightarrow \text{TiB}$ and $\text{Ti} + 2\text{B} \rightarrow \text{TiB}_2$ reactions from 0°C to 3000°C (Calculated by HSC-5.0 software).

It is obvious that the Gibbs free energies of formation of both borides are negative, but lower values of ΔG favor TiB_2 formation during direct $\text{Ti}+\text{B}$ reaction.

TiB_2 has hexagonal symmetry (C32) with space group P6/mmm and TiB exists in FeB-type (B27) structure with primitive orthorhombic (Pnma) crystal [18]. It is reported that TiB also can be in NaCl structure [19]. Besides TiB_2 and TiB , experimental studies evidenced the existence of Ti_3B_4 with a special orthorhombic Ta_3B_4 -type structure. Ti_3B_4 is seldom mentioned and considered as a middle product or byproduct due to the high temperature peritectic reactions $\text{L}+\text{TiB}_2\leftrightarrow\text{Ti}_3\text{B}_4$ (2473K) and $\text{L}+\text{Ti}_3\text{B}_4\leftrightarrow\text{TiB}$ (2453K), and Ti_3B_4 is only stable to temperatures as low as 1690°C [20]. According to the first-principal calculations Ti_2B intermetallic compound also exists [21].

TiB_2 is the most stable compound in Ti-B system and mostly used in industries. The preparation methods of titanium diboride powder are decisive for the properties (chemical, physical, and mechanical) and define its application field. Several methods have been utilized in the synthesis of TiB_2 so far [22], [23]. Among them are:

- (1) Direct reactions of elemental titanium with boron $\text{Ti}+2\text{B}\rightarrow\text{TiB}_2$ (i) in the furnace, (ii) in the self-propagating high-temperature synthesis (SHS) reactor and (iii) by mechanical alloying.
- (2) Carbothermal reduction or hydrogen reduction from titanium and boron oxides.
- (3) Borocarbothermic reduction: $2\text{TiO}_2 + \text{B}_4\text{C} + 3\text{C} \rightarrow 2\text{TiB}_2 + 4\text{CO}$.
- (4) Solid state reaction: $\text{TiO}_2 + 3\text{NaBH}_4 \rightarrow \text{TiB}_2 + 2\text{Na}(\text{g},\text{l}) + \text{NaBO}_2 + 6\text{H}_2(\text{g})$.
- (5) Solvothermal reaction: $\text{TiCl}_4 + 2\text{B} + 4\text{Na} \rightarrow \text{TiB}_2 + 4\text{NaCl}$.
- (6) Metallothermal reduction: titanium and boron oxides reduced by Mg or Al.

1.2 Consolidation of Ti-B based materials

Despite the attractive properties, the application of TiB_2 is rather narrow on account, due to low sinterability caused by the formation of oxide layer on the surface and lack of machinability regarded to low fracture toughness at room temperature. Despite TiB_2 can be densified by liquid phase sintering with numerous metallic additives Cr, Ni, Fe, Cu etc. [14], [24], [25], [26], however the presence of metallic phase causes degradation of properties at elevated temperatures. While non-metallic additives (mainly SiC , Si_3N_4 , B_4C , TiC , WC , TiN , MoSi_2 , and ZrB_2) improve sinterability of TiB_2 without worsening the high temperature properties [27], [28], [29], [30], [31], [32], [33], [34], [35]. However, in this case the sintering process requires application of very high temperatures. The rundown of consolidation of TiB_2 based composites is given in Table 1.2. TiB preferably exists in Ti matrix composite, the consolidation of TiB -Ti composites is briefed in Table 1.3.

For the fabrication of Ti-B based composites with high content of ceramic phase, the combine of advanced synthesis (such as self-propagating high-temperature synthesis) and consolidation methods may offer new attractive technological possibilities and economic advantages, i.e. higher activity during sintering, a high chemical purity, a high content of combined boron, a controlled morphology of particle surfaces, facilitating in-situ chemical reactions, formation of materials into different shapes, etc.

Table 1.2 Consolidation of TiB₂ based composites.

System	Sintering method	Temperature (°C)	Relative density (%)	Hardness (GPa)	Reference
TiB ₂ -Cr	Pressureless sintering	1900	-	-	[24]
TiB ₂ -Ni	SPS	1150-1300	99.8	25	[25]
TiB ₂ -Fe	HIP	1500-1650	97.8-99.1	15.1-22.6	[14]
TiB ₂ -Cu	SPS	1100, 1200	96	-	[26]
TiB ₂ -SiC	SPS	1600-1800	97.1	27.4	[27]
TiB ₂ -TiC	HP	2477	99	22.6-23.9	[29]
TiB ₂ -SiC	HP	2000	99.3	23.6	[30]
TiB ₂ -Ti ₃ AlC ₂	HP	1500	98.5	25	[34]
ZrB ₂ -TiB ₂	SPS	1400	>95	34	[35]

Table 1.3 Consolidation of TiB-Ti composites.

Material	Process	Relative density (%)	Hardness (GPa)	IFT (MPa·m ^{1/2})	Reference
TiB-91.65vol.%Ti	SLM	99.5	4.02	-	[36]
TiB ₂ -TiB _w -90.4wt.%Ti	SPS	>97.5	5.86	-	[31]
TiB _w -60wt.%Ti	SPS	99.6	-	9.35	[37]
TiB-33vol.%Ti	Ball Milling + Reaction HP	-	13.51	-	[4]
TiB-30wt.%Ti	SHS + HIP	98.45	11.5	6.15	[38]
TiB-20wt.%Ti	SHS + HIP	97.57	10.6	5.23	[38]

1.3 Spark plasma sintering

The most works on densification of Ti-B based materials (Table 1.2 and Table 1.3) have been done using hot-pressing (HP), hot isostatic pressing (HIP) and spark plasma sintering (SPS). As shown in Fig. 1.3, consolidation by HP is achieved by the application of heat and uniaxial pressure simultaneously, while HIP applies isostatic pressure to materials using compressed gas [39], [40]. Compare with the other consolidation methods, the SPS process is an unique consolidation technique in heating process by using a high pulse and low voltage current directly through the sample [41], [42]. As a result, the heating efficiency of SPS is much higher and the heating speed can reach up to 1000 °C·min⁻¹. During the SPS process, Joule heat is produced by pulsed direct current passing through graphite mold and/or powder particles. The temperature is controlled

by thermocouple or pyrometer. The uniaxial pressure is applied during the heating process and controlled by a hydraulic system. SPS is already proved to be suitable for sintering a wide range of materials, including pure metals, alloys, ceramics and composites [41]. The processing of bulk ceramics via SPS method leads to the refinement of microstructure which in turn contributes to the enhancement of mechanical (hardness and strength) and physical (thermal and electrical) properties. Regardless the several advantages of SPS, it is not yet capable to process parts with intricate inner features, as they depend on the geometry of the mold.

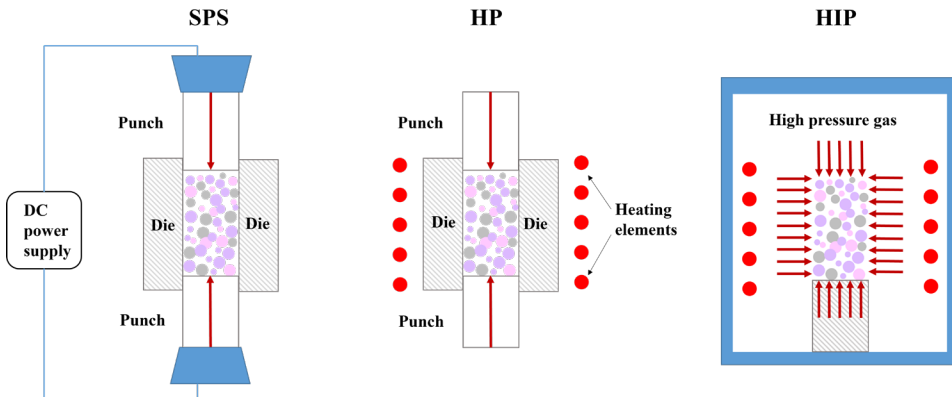


Figure 1.3 Scheme of Spark plasma sintering (SPS), Hot pressing (HP) device and hot isostatic pressure (HIP) devices.

1.4 Powder bed fusion (PBF): Selective laser melting (SLM)

1.4.1 Powder bed fusion overview

Additive manufacturing (AM) exhibits great potential of manufacturing advanced parts of intricate geometry for mechanics, aerospace, and other fields [43], [44], [45], [46]. AM is suitable for the construction of complex shapes, as it can transfer the digital 3D model to 2D layers and build the parts layer-by-layer [47]. Different types of AM technologies have been developed to meet the requirements of advanced materials engineering. The AM classification according to the process mechanism is presented according to ISO/ASTM 52900 in seven categories, and two of them are based on powder bed processes, namely binder Jetting (BJ) and powder bed fusion (PBF, Fig. 1.4) [48], [49], [50], [51], [52].

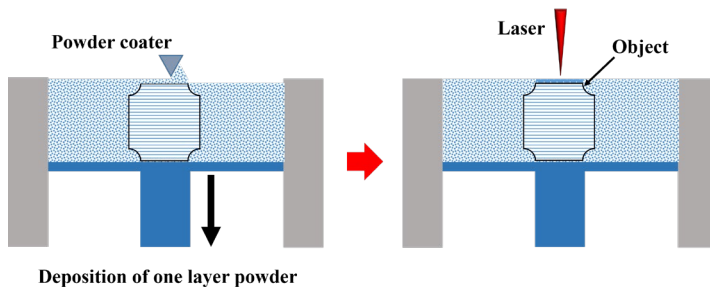


Figure 1.4 Scheme of powder bed fusion process.

In powder-bed fusion processes, thermal energy selectively consolidates desired sections of a powder material layer by layer [53]. The powder particles of each layer are fused together with a laser beam, electron beam or a binder. Fresh layer of powder is spread by a coater in between each fusion of layers. A platform lowers the model step by step and a green body builds from the powder bed. The excess powder is recycled after treatment (such as sieving). The main disadvantage of natural supports is that for hollow part it must be designed with an open or escape hole for removal of the excess material.

PBF includes the following commonly used printing techniques: electron beam melting (EBM), selective laser melting (SLM), selective laser sintering (SLS) and direct metal laser sintering (DMLS) [54]. EBM operates in a vacuum chamber with an electron beam generated in an electron beam gun [53]. Selective laser sintering and selective laser melting are both the layer-wise material addition techniques by consolidating successive layers of powder using the energy of laser beam, however different fusion mechanisms occur during the process (sintering or melting) [55]. In the direct SLS of ceramics, the high heating and cooling rates cause brittleness and poor fracture toughness of obtained shapes, so it may include a multi-step technology, such as the manufacturing of a green body with subsequent removal of binder and densifying in a furnace [56], [57]. Direct metal laser sintering (DMLS) is the same as SLS, but only metals are utilized.

1.4.2 Selective laser melting

As one of the most well-developed PBF technologies, SLM allows the producing of complex shapes and structures through the solidification of powder layer by layer [58]. The working process of SLM is as follows: powder material is applied in thin layers and melted at the predetermined areas using thermal energy supplied through a powerful laser beam. Following the melting of all selected locations of the target layer, the work platform is lowered, as a result new powder layer can be supplied repeatedly by the wiper, until the complete shape formation of the samples. Laser melting of metal powders requires Nd:YAG lasers or more commonly Yb:YAG-fiber lasers, which generate a laser beam with 1.06-1.07 μm wavelength, that is closer to the high absorptivity range of the most metallic powders.

The main advantages of SLM method are fine resolution, good strength and high quality of the product, while the process is costly, the produced part usually comprises a support that needs to be removed by post processing [59].

SLM technology has been used mostly for manufacturing metallic materials and metal-based composites. Metal-ceramic composites can be produced by SLM through mixing metal binders with ceramic powders, or through in-situ chemical reactions. The in-situ formation of metal-ceramic composites are far more advantageous compared to pre-mixed composites, because of the enhanced wettability between ceramic and metal, as well as fine and homogeneous distribution of ceramic or newly generated phases. But only limited systems are suitable for in-situ reactions, as the amount of energy generated from the chemical reaction is difficult to control. Another promising solution is to develop composite powders adopted for SLM process.

1.4.3 Power requirements for SLM

For SLM applicable powders, size and shape must be tightly controlled because of their impact on powder flowability and deposition which altogether affect laser consolidation. There are several basic requirements for powder feedstock suitable for SLM process:

- (1) Powder flowability is an essential factor in SLM process, responsible for spreading powder smoothly across the build area and creating a uniform powder layer before irradiation [60].
- (2) Homogeneous and dry powders of spherical morphology provide even distribution and improved powder flow. Particle shape irregularities increase surface area and may cause agglomeration. Rough surface and high humidity may result in deterioration of powder flow [61].
- (3) Particle size distribution (PSD) is an important parameter, which influences number of operations of the SLM process, including powder spreading, storage and recycling [62]. In reused powders, particles becoming bigger as compared to the fresh powder is a common issue caused by pre-sintering of particles near the laser scanned areas. Also, spattered metal particles adhere onto neighboring particles and form larger and irregular powder structures [63].
- (4) Low oxidation level is important because oxidation usually hinders the consolidation, causes instability, breaks up the melt pool into droplets during the laser treatment process [64].
- (5) Thermal properties (thermal absorptivity and conductivity) of powders are detrimental due to the influence of laser absorptivity, melt zone formation and heat transfer mechanisms in the SLM process [53].

In general, commercial metals (alloys) powders for SLM are prepared by atomization method. During atomization liquid metal is broken into many droplets, then solidifies at flight cooling process in a chamber. The three main powder atomization methods for 3D printing [65] are shown in Fig. 1.5. There are three steps for all the atomization processes: 1) melting, 2) atomization and 3) solidification.

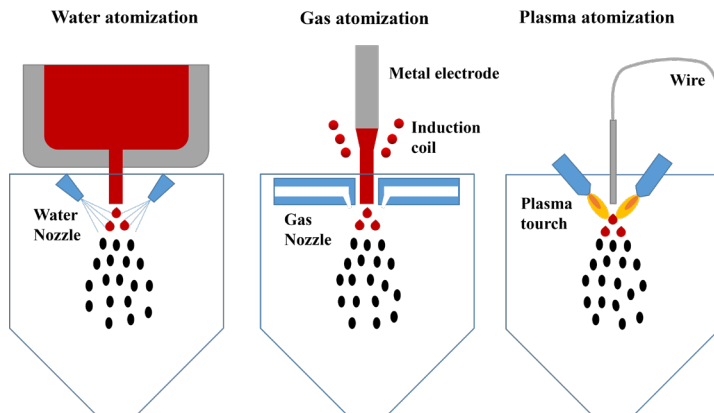


Figure 1.5 Scheme of powder atomization process.

Water atomization (WA) is primarily used for ferrous and related alloys. It is a low-price mode of atomization, but limits powder purity of reactive metals and alloys. The essence of gas atomization (GA) lies beneath using a high-pressure gas (N_2 or Ar) to break up liquid metal flow through a nozzle. Although it is a relatively developed

technology, there are some hindering problems. Fine particles may fly back and lead to a collision partially melted particles from the circulation of gas in the atomizing chamber, which causes formation of satellite particles. These satellite particles are not desired for some applications as they have negative influence on the flowability of powder. In the plasma atomization (PA) process, a pre-alloyed wire is inserted onto a hot zone created by plasma torches. The wire is melted and then broken into droplets that cooled promptly, thus it is suitable for producing powders with high purity. But the cost of plasma atomization is much higher compared to the other two atomization processes.

Self-propagating high-temperature synthesis has curious perspective to develop a powder suitable for SLM processes, as SHS allows to tailor structural features of produced powders by changing the initial composition of precursors' mixture, sample size, packing density, chamber pressure, etc. The development of ceramic composite powders of special microstructure by the advanced SHS technology will create a new industrial platform for producing powders for the consolidation processes (SLM) of complex components with tailored physical-mechanical properties.

1.5 Self-propagating high-temperature synthesis

Self-propagating high-temperature synthesis (SHS) is an exothermic chemical reaction proceeding in a self-supporting manner for the production of solid materials in either air or an inert atmosphere [10], [11]. The method is based on the concept that once initiated locally by means of a momentary thermal heating, a highly exothermic chemical reaction self-propagates through the precursors converting them into desired products (Fig. 1.6). The beneficial aspects of CS are the high temperatures (500-3000°C), high heating rates (10^2 to 10^6 °C·s⁻¹), and short reaction times. SHS received considerable attention as an innovative method to synthesize advanced materials including refractory ceramics, intermetallics, composites, as well as pure metals from cheap and available precursors [66]. SHS provides also a wide range of materials not only in the form of powders, porous materials, but also non-porous compacts, casts and coatings [67].

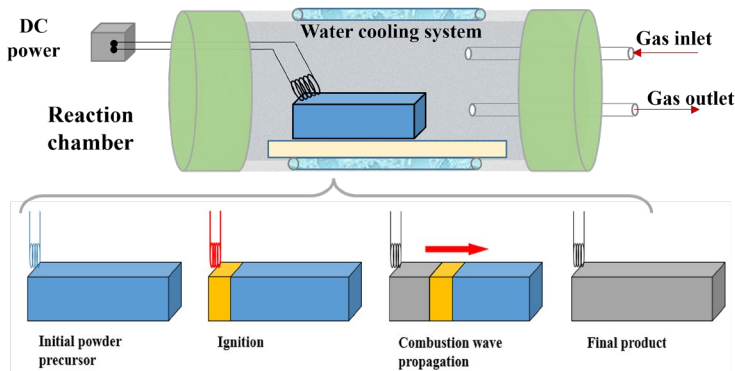


Figure 1.6 Scheme of Self-propagating high-temperature synthesis (SHS) process.

As a result, SHS exhibits great flexibility, allowing to manufacture a wide diversity of products on virtually the same equipment. Up to now, more than three thousand substances and materials have been synthesized by the SHS method, and a number of

productions based on it have been established [68]. In comparison with the conventional methods of synthesizing materials in high-temperature furnaces, SHS has a number of obvious advantages, namely: low energy consumption, simple and small-sized equipment, high performance (productivity, effectiveness, substantial price reduction), high purity of products due to self-purification phenomena at high temperatures, environmentally friendly, easy scaling-up ability, etc., considering that:

- (i) SHS is a flexible, simple, energy-saving way to produce refractory and hard materials with high purity, controllable phases and microstructure,
- (ii) the structures formed during SHS process may provide enhanced exclusive properties of ceramic based composites of SPS and SLM printed parts.

1.6 Objectives of the study

The production of ceramic-based composites remains the provoking puzzle as the manufacturing of the end-products with consistent and predictable properties requires input materials with exact specifications. The latter in turn requires reliable and effective methods for powder synthesis. One of the key issues hindering further applications of Ti-B ceramic based materials is the limited number of materials suitable for the processing by advanced consolidation techniques (AM through SLM, SPS, etc.).

Therefore, the **objective** of the PhD study is the design, synthesis and development of Ti-B based powder feedstocks suitable for SPS and SLM processing to produce bulk, porous and complex shaped reliable items using the developed powders.

To tackle the objective, the **specific aims** are formulated as follows:

1. Feedstock
 - TiB₂-Ti feedstock preparation from commercially available powders for SPS and SLM consolidation.
 - Development and SHS preparation of Ti-B based composite powders of special size and morphology suitable for SPS and SLM processing.
 - Characterization of the prepared feedstocks.
2. Spark plasma sintering
 - SPS consolidation of commercially available TiB₂-Ti powder mixture and SHS-derived Ti-B based composite powders. Study of mechanical properties and tribological behavior (sliding wear resistance, etc.) of fabricated compact parts.
3. Selective laser melting
 - SLM fabrication of (i) bulks and lattices from commercially available TiB₂-Ti powder mixture, (ii) SHS-prepared Ti-B based composite powders. SLM process optimization. Characterization and examination of phase transformation and microstructure features of SLM produced parts.

2 Materials and methods

2.1 Feedstock preparation and design of the systems

The raw materials used for the preparation of powder feedstock are listed in Table 2.1.

Table 2.1 Raw materials (powders).

Name	Composition	Particle size (μm)	Purity (%)	Impurity elements	Producer
Boron	B (amorphous)	<1	95	C, Fe	Sigma-Aldrich
Titanium	Ti	<44	99.5	O, N, H, C	Alfa Aesar
Silicon	Si	<20	99	O, C, B, H	Sigma-Aldrich
Titanium diboride	TiB ₂	<25	99.5	O, C	Alfa Aesar

Three pathways were utilized to prepare precursors for the consolidation processes:

(i) Feedstock 1: mechanical mixing of commercially available TiB₂ and Ti powders with the composition (50wt.%TiB₂-50wt.%Ti).

(ii) Feedstock 2: SHS of Ti-B elementary mixtures. The maximum amount of ceramic phase (TiB₂) according to the sinterability was experimentally deduced to be 50wt.% TiB₂ in the commercially available powder TiB₂-Ti mixture. To prepare the powder for consolidation with the same composition (50wt.%TiB₂-50wt.%Ti) by SHS method Ti-B precursor mixture (85wt.%Ti-15wt.%B) was utilized.

(iii) Feedstock 3: SHS Ti-B-Si elementary mixtures. Direct SLM of SHSed Ti-B based powder was impossible due to high ceramic phase content (>80wt.%), thus Si was chosen as a binder material. And the precursor for the SLM process was produced by SHS of Ti-B-Si elementary mixture with 38.6wt.%Ti-17.4wt.%B-44wt.%Si composition.

The schematic overview of synthesis and consolidation Ti-B based material by SPS and SLM from commercial powder mixture and SHS-ed powder respectively is depicted in Fig. 2.1 and the designed powder percentage for SHS is listed in Table 2.2.

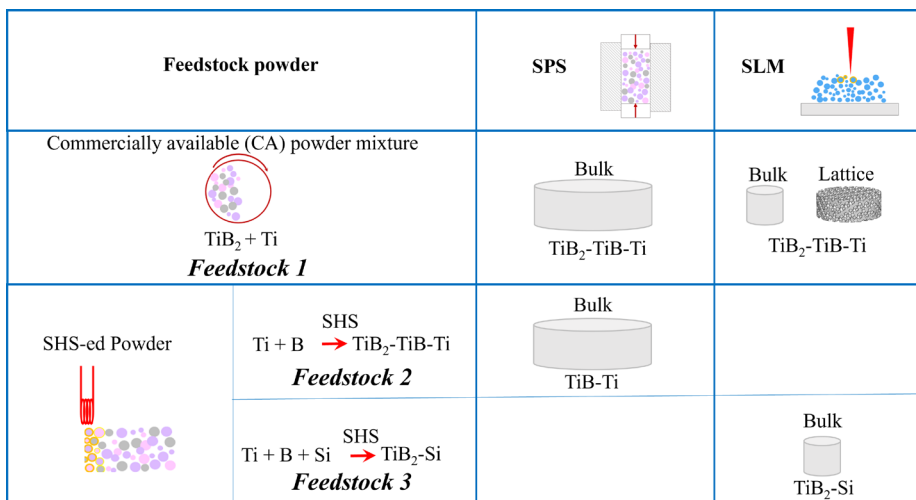


Figure 2.1 The preparation pathways for Ti-B based composites.

Table 2.2 The composition of SHS raw materials and products.

SHS System		SHS raw materials			SHS Products (calculated)			
		Ti	B	Si	Ti	TiB	TiB ₂	Si
Ti-B (Feedstock 2)	(moles)	1.28	1	-	0.28	1	0	-
	(wt.%)	85	15	-	18.6	81.4	0	-
Ti-B-Si (Feedstock 3)	(moles)	1	2	2	0	0	1	2
	(wt.%)	38.6	17.4	44	0	0	56	44

2.1.1 Mechanical mixing

Ti-TiB₂ mixture of composition 50:50 wt.% (Feedstock 1) was prepared from commercially available powders of pure Ti and TiB₂ by mechanical mixing.

TiB₂ and elemental Ti powders were dry mixed in a motor driving rotating plastic bottle (100 mm diameter and 150 mm height) for 2 h at 20 rpm speed and further were dried in oven at 60°C for 20 min before the consolidation procedure for moisture removal.

2.1.2 SHS of Ti-B, Ti-B-Si composite powders

For SHS process, a mixture of reactants (calculated according to Table 2.2) was homogenized in a ceramic mortar for 15 min. The green body was prepared in two ways: 1) stuffing into rectangular stainless-steel boat of 10 cm length, 20 mm width, 12 mm height; 2) uniaxial pressing of cylindrical or hexagonal shape formed by die-mold. The samples were inserted into a CPR-3.5I reaction chamber filled with argon gas of 99.99% purity at pressure of 0.3 MPa. The mixture of KNO₃ and Si powders (3 g) of the weight ratio 1:4 was used as igniting mixture positioned on the terminal or surface of the green body. To initiate the combustion reaction, a tungsten coil buried in the igniting mixture was charged with electricity under 12 V for 5 sec. Two C-type tungsten-rhenium (W/Re-5 and W/Re-20, 0.1mm in diameter) thermocouples were positioned at holes drilled in a green body to record temperature-time history of the combustion wave propagating process. After the SHS process, samples were cooled down in the chamber and the produced composites were further crushed or milled into fine powders. From the temperature-time curve the maximum combustion temperature (T_c) and the average combustion velocity (U_c) were deduced. T_c was averaged from two maxima temperatures of the recorded profiles. U_c was calculated by formula: $U_c = L/t$, where L is the distance between the two thermocouples, t is the time interval of combustion wave propagation between the two thermocouples.

2.2 Spark plasma sintering

The consolidation of commercial TiB₂-Ti powder mixture and SHSed Ti-B based composite was performed in SPS (FCT Systeme GmbH, Germany) in vacuum (<5 mbar) employing continuous DC power. A graphite mold and punch set up for sample in 1 inch (25.4 mm) diameter was used for the sintering. The 20 g powder mixture was loaded into a graphite mold (graphite papers were located between the punch/mold and powder) and a BN solution was sprayed on the inner surface of graphite paper to make for easy separation after sintering. A fixed heating rate of 100 °C·m⁻¹ was applied to fabricate the samples with 8 mm in height, then cooled down by up to ~200 °C·m⁻¹. Considering the high relative density and stable producing process, the optimized parameters are listed in Table 2.3.

Table 2.3 The process parameters of SPS.

Precursor	Pressure (MPa)	Temperature (°C)	Dwelling time (min)	Heating rate (°C·min ⁻¹)
Commercial TiB ₂ -Ti (Feedstock 1)	35	1500	3	100
SHSed Ti-B (Feedstock 2)	50	1200	3	100

2.3 Selective laser melting

Metal 3D printer (ReaLizer GmbH SLM-50, Germany) was used for the SLM consolidation process. The laser equipped is a Yb:YAG fiber laser of 1070 nm wave length and the maximum nominated output power is 120 W. The SLM process was performed in an argon protective atmosphere chamber with oxygen level below 0.5%.

The laser energy density (LED) was calculated based on the following equation: $E=P/vhd$, where P is laser power, v is scanning speed, h is hatching distance and d is layer thickness. The scanning speed is evaluated from the quotient of exposure time and point distance. Bar shaped bulk samples with 10 mm diameter and 5 mm height were produced from the commercial TiB₂-Ti powder mixture (Feedstock 1) at 1500-3500 mA laser current (Fig. 2.2).

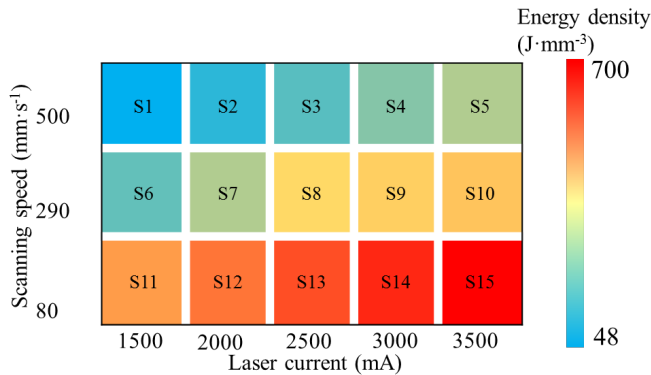


Figure 2.2 The SLM process parameters for consolidation of bulk solid samples from commercial TiB₂-Ti powder.

Lattice structures from the commercial TiB₂-Ti powder mixture (Feedstock 1) were 3D printed at a fixed scanning speed of 80 mm·s⁻¹, using the laser current of 2000 mA, layer thickness of 25 μm and hatching distance of 60 μm. The printed lattices were later heated in the furnace (WEBB, USA) up to 1100°C (dwell time 3 h). The heating rate was 10 °C ·min⁻¹ in the nitrogen gas flow of 200 ml·min⁻¹ (purity 99.999 vol.%) during the heating process. The purpose of the nitridation was to convert the SLM produced ceramic-metal lattices into fully ceramic structures.

For the SHS-ed TiB₂-Si powders (Feedstock 3), solid cylinders (∅10×5 mm) were built by SLM using laser current 1400-2200 mA at a scanning speed of 80 mm·s⁻¹ and layer thickness of 25 μm. The latter was chosen based on the average diameter (D50=21 μm) of the used TiB₂-Si powders.

2.4 Characterization

The particle size distribution of powders was assessed with the help of a laser diffraction using Malvern Mastersizer 3000 (Almelo, Netherlands). Hall Flowmeter was used to evaluate the flowability. According to the EVS-EN ISO 4490:2018 standard, test result was recorded as a time of 50 g of powder flowing passing through a $\varnothing 2.5$ mm hole in a standard funnel.

After the SPS process the surface graphite layers were removed by a grinding machine (80036, Cromag). After SPS and SLM processes, the samples were polished to 1 μm finish using a Phoenix 4000 (Buehler, USA) system at flowing water with the help of 8-inch diamond grinding discs (DGD Terra, Buehler, USA). The polishing was executed in a speed of 300 $\text{rev}\cdot\text{min}^{-1}$ and kept for 3 minutes for each disc. The discs were changed in a certain sequence (74, 40, 20, 10, 3 and 1 μm) and then cleaned with acetone and ethanol.

Archimedes' densities of bulks were measured using balance (Mettler Toledo ME204, 0.1 mg accuracy, Australia), and geometrical densities were calculated from samples' size (measured by digital caliper, 0.01 mm accuracy) and weight (measured by Eltra 84 analytical balance, 0.1 mg accuracy).

The morphology and chemical composition of the initial powders, SHS-ed powders, SPS-ed compacts and SLM produced specimens were analyzed by scanning electron microscopes (SEM, HR-SEM Zeiss Merlin, Germany) equipped with EDS (Energy Dispersive X-Ray Spectroscopy) detectors.

Phase composition of the samples was analyzed by X-ray diffractometers (XRD, D5005, Bruker, USA). Rietveld refinement method was used to evaluate the concentrations of compounds and elements.

The hardness was evaluated by a Indentec 5030 SKV tester (Brierley Hill, UK), a load of 1-30 kgf were chosen and the final hardness value were calculated from average of at least 5 measurements.

Compressive strength tests were performed by Zwick universal test machine (ZwickRoell Group, Germany). The strain rate of 0.1 min^{-1} was chosen based on ISO 13314:2011 standard [69].

A universal tribo-test device (CETR/Bruker - UMT-2, USA) was employed for materials testing under dry unidirectional sliding in ball-on-plate configuration. The ball counterbody of Al_2O_3 with $\varnothing 10$ mm (Redhill Precision, Czech Republic), hardness $\text{HV}_{10} \approx 1450$ and surface roughness $R_a = 0.02$ μm was exploited under the applied loads of 5 N (0.51 kgf) and 20 N (2.04 kgf), sliding speed of 0.1 ms^{-1} and distance of 1000 m with the radius of a wear track of 4.5 mm. Each test consists of 20 equal periods with duration of 500 s to assess friction evolution during each period (start, running and stop). Tests were performed both at room and elevated temperature (up to 900°C) and coefficient of friction (CoF) were evaluated. Besides CoF, the volume wear loss was recorded by 3D profilometer (Bruker Contour, USA).

3 Results and discussion

3.1 Feedstocks

3.1.1 Feedstock 1. Commercial Ti and TiB₂ powder mixtures

Powder feedstock 1 represents commercial mixture of 50 wt.% Ti and 50 wt.% TiB₂. The morphology examined by SEM in Fig. 3.1 shows the irregular shape (Fig. 3.1a) of the Ti and flaky shape (Fig. 3.1b) of the TiB₂ powder particles.

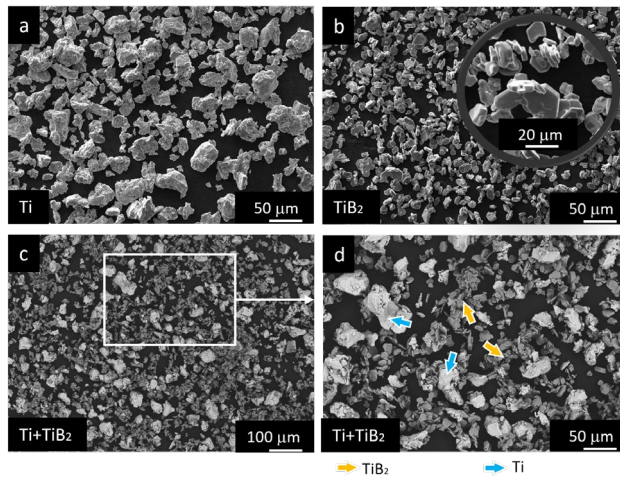


Figure 3.1 SEM images of the initial powders (a) Ti, (b) TiB₂ and their mixture at different magnifications (c) (x150), (d) (x300) (adapted from Publication III).

After mixing, the powder displays <20 micron-size TiB₂ particles with regional agglomerates (Fig. 3.1c and d). The flowability of the mixture was not possible to evaluate using the Hall Flowmeter method due to severe blocking of the hall hole during the testing.

3.1.2 Feedstock 2. SHS-ed powder from Ti-B for SPS

Powder feedstock 2 was prepared from combustion of element Ti and B powder mixtures with 1.2:1 molar ratio by SHS. The reaction between Ti and B in SHS process is a highly exothermic process ($T_{ad}=2660^{\circ}\text{C}$, calculated by ISMAN-Thermo software). Fig. 3.2b shows the combustion thermogram and pressure change curve during the SHS process. The maximum combustion temperature of 1700°C was reached at $2.12\text{ mm}\cdot\text{s}^{-1}$ combustion wave propagation velocity ($U_{heating}=2500\text{ }^{\circ}\text{C}\cdot\text{s}^{-1}$). The thermal mode of combustion process was beneficial for Ti melting ($T_m=1668^{\circ}\text{C}$) and dissolving/interacting with B to form TiB as per the principle of reaction diffusion. Additionally, an excess amount of Ti ($n_{excess}=0.2\text{ mol}$) in the system serves as an adhesion phase for the composite powder. The combustion product retains at high temperature for few seconds and temperature drop of below melting point of Ti is demonstrated at cooling rate of $U_{cooling}=10\text{ }^{\circ}\text{C}\cdot\text{s}^{-1}$ (Fig. 3.2b). The wide post-combustion and cooling zones favor the formation of spherically shaped Ti droplets/particles.

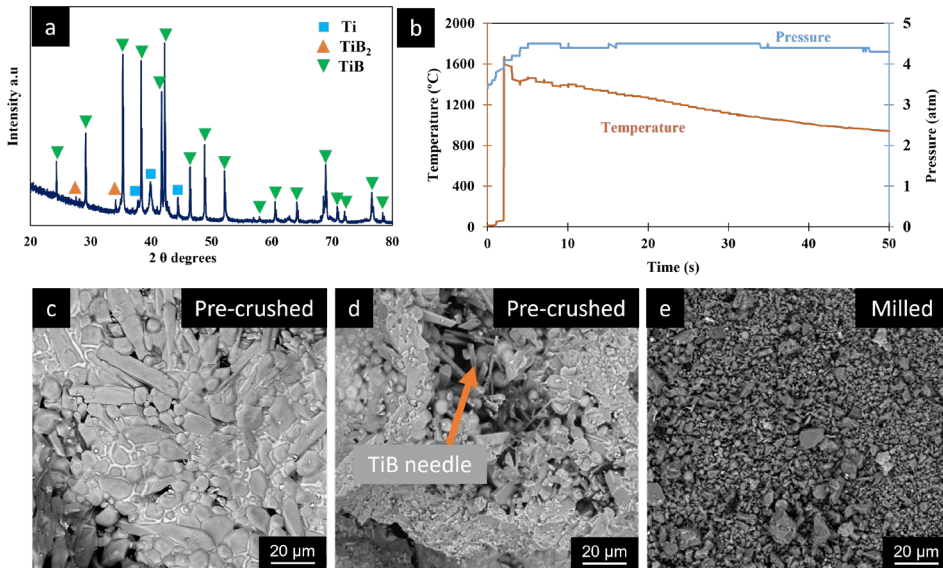


Figure 3.2 (a) SHSed bulk product; (b) Combustion temperature and pressure evolution; (c, d) Typical examples of pre-crashed piece; and (e) Composite powder after the milling by disintegrator (*adapted from Publication II*).

The SEM images of pre-crashed SHS product in Fig. 3.2 (c, d) demonstrate the co-existence of agglomerates of fine and coarse particles of either rounded or needle-like morphology. Spherical droplets of molten Ti were also present as Ti was added with an excess amount to the initial mixture. Since the elemental boron tends to center segregation on subsequent precipitation from molten solution of Ti and B, the TiB needles mostly grow towards the center during SHS processing.

Fig. 3.2e shows the SEM image of TiB-Ti composite powder after disintegrator milling. Particle size distribution (PSD) specified in Table 3.1 reveals the median diameter (D50) of TiB-Ti powder of around 9 μm , which is dramatically smaller compared to commercial TiB₂-Ti powder mixtures (Fig. 3.1). Such distribution may contribute to the homogeneity of precursor for the subsequent SPS consolidation process.

Table 3.1. Particle size distribution of the SHSed TiB-Ti powder after disintegrator milling (*adapted from Publication II*).

Particle Size of SHSed TiB-Ti powders		
D10 (μm)	D50 (μm)	D90 (μm)
2.12	8.98	27.2

The XRD patterns (Fig. 3.2a) of SHSed TiB-Ti powder confirm the presence of TiB, TiB₂ and free Ti. The presence of TiB₂ phase along with Ti and TiB is explained as follows: the reaction of fine Ti particles with boron proceeding in several stages includes the formation of diboride matrix, melting of Ti particles, capillary flow of Ti melt and its reaction with diboride with the subsequent formation of monoboride. In addition, the insufficient time for completion of the reaction between TiB₂ and Ti due to fast propagation of the combustion wave is responsible for the presence of TiB₂. According to Rietveld refinement method the approximate concentrations were estimated as of 17.4 wt.% free Ti, 66.4 wt.% TiB and 16.2 wt.% TiB₂.

3.1.3 Feedstock 3. SHS-ed powder from Ti-B-Si for SLM

For powder feedstock 3, Ti-2B-2Si mixture was prepared for the combustion synthesis. The combustion synthesis was accomplished according to thermodynamic calculations considering a temperature of TiB₂-Si formation ($T_{ad}=1700^{\circ}\text{C}$, calculated by ISMAN-Thermo software). During the reaction between Ti-2B-2Si mixture, the maximum combustion temperature of 1530°C (Fig. 3.3b) was recorded, which coincides to the thermodynamic calculations. The combustion front in the Ti-B-Si mixture progresses along the specimen heating reagents in the combustion wave at $250^{\circ}\text{C}\cdot\text{min}^{-1}$ rate as an undulating movement with a combustion velocity of $0.24\text{ cm}\cdot\text{s}^{-1}$, in contrast to Ti-B mixture with smooth planar wave. The undulating movement is influenced by a liquid silicon phase in the front of the wave and produces a layered structure in the combustion product.

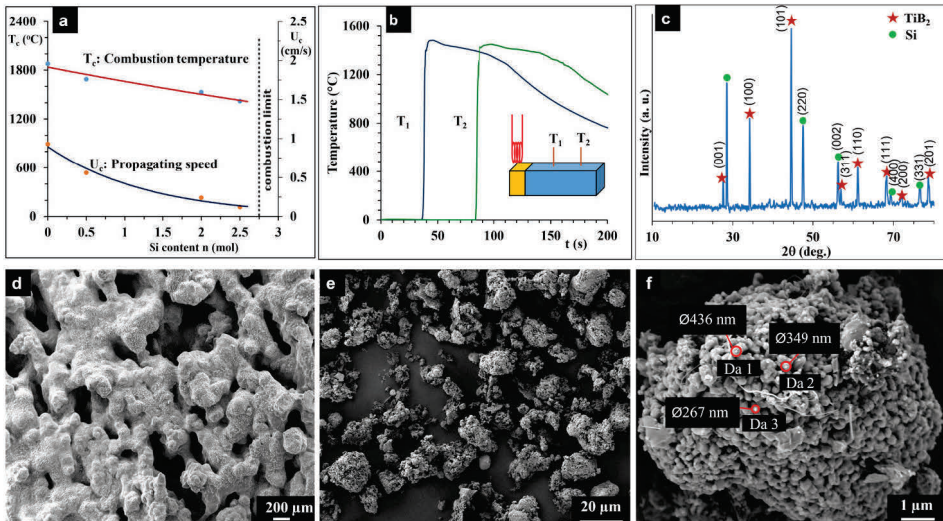


Figure 3.3 (a) Combustion peculiarities in the $\text{Ti} + 2\text{B} + n\text{Si}$ system; (b) Combustion temperature profiles; (c) XRD pattern of the produced powder; (d) SEM images of porous bulk SHS TiB₂-Si product; (e and f) milled TiB₂-Si powder (adapted from publication V).

XRD pattern of the combustion product of Ti-2B-2Si mixture certifies that product consist of only hexagonal titanium diboride and silicon (Fig. 3.3c). SEM analysis of the product immediately after the combustion synthesis depicts the bulk sample of porous morphology composed of many spherical protrusions (Fig. 3.3d). The porous bulk easily powdered by milling portrays an assembly of particles ($<50\ \mu\text{m}$) and their agglomerates (Fig. 3.3e). Higher resolution SEM image (Fig. 3.3f) shows that the spherical protrusion has a “pomegranate-like” structure. This “pomegranate-like” particle represent the gathering of nano-size and ultra-fine TiB₂ particulates “gluing” by silicon binder. The diameters of 436 nm, 349 nm, and 267 nm were measured for the selected particulates, named as Da1, Da2, Da3 in Fig. 3.3f. As shape of the precursor powders controls the spreading of particles and packing through the deposited layer during SLM process, the “pomegranate-like” structure will promote the melting/solidification process positively.

The SHS-derived TiB₂-Si feedstock comprises particles of pomegranate-shaped morphology and required particle size distribution. As well-documented, the PSD influence flowability, moreover round particles enhance the spreading of powders,

hence, vastly affect the final property of the produced part. In this work, the milled powder was sieved and ranged (less than 20 μm , 20-45 μm and 45-90 μm particle size). The PSD and flowability of powders tested by Hall flow meter are shown in Table 3.2. The flowing property of powders with particle size less than 20 μm was low, and supremely result was reported. The powders with particle size in the range of 20-45 μm show moderate flowability appropriate for the SLM process to provide a homogenous and smooth spreading of the powder.

Table 3.2 Particle size distribution and flowability of produced TiB_2 -Si powders.

Particle size range (μm)	Particle size distribution (μm)	Hall flow rate (s/50g)
$\mu < 20$	-	-
20 - 45	D10=5.48, D50=21.2, D90=41.4	29.75 ± 0.31 (acceptable for SLM)
45 - 90	D10=12.3, D50=57.56, D90=85.4	24.68 ± 0.34

3.2 Spark plasma sintering

3.2.1 SPS of commercial Ti and TiB_2 powder mixtures (Feedstock 1)

After SPS processing of commercial Ti and TiB_2 powder mixtures (sample image shown in Fig. 3.4a), the surface X-ray diffraction pattern (Fig. 3.4b) reveals the coexistence of Ti, TiB and TiB_2 phases, so the chemical reaction between Ti and TiB_2 was not accomplished at the given sintering temperature and duration (1500°C, 3 min).

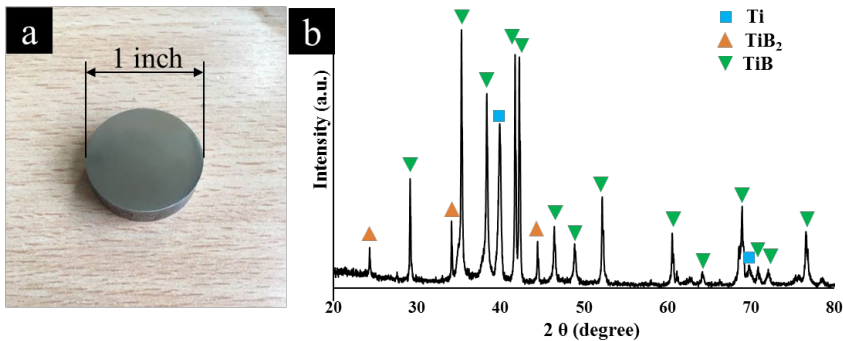


Figure 3.4 (a) Photo image and (b) Surface XRD pattern of the SPSed TiB_2 -Ti sample.

The specimens were polished for microstructure analysis by SEM. The fractured specimens were also examined and the morphology of fracture and polished surfaces are displayed beside each other (Fig. 3.5). The samples are not homogeneous, in-situ synthesised TiB comprise particulates of a length of less than 2 μm and a diameter of few hundred nm randomly distributed on the polished surfaces of composite specimens. The lack of porosity observed in SEM images of polished fracture were in compliance with the Archimedes density measurements (relative density 99.4%).

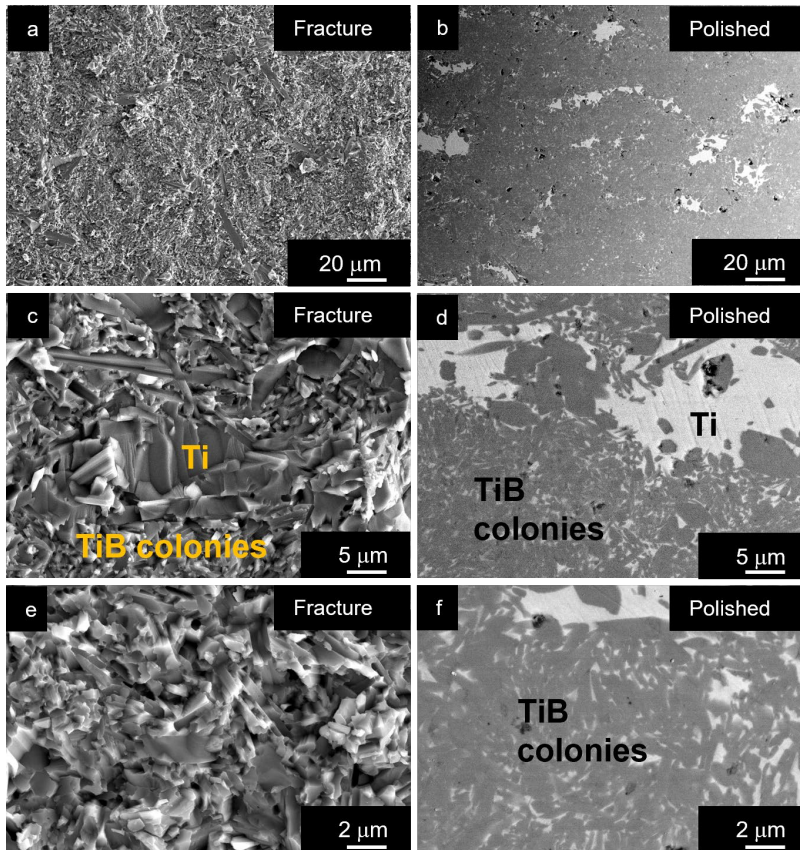
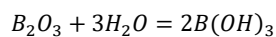
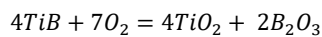


Figure 3.5 The SEM image of SPSed TiB_2 -TiB-Ti composite (a, c, e) fracture and (b, d, f) polished surfaces (adapted from Publication I).

Macrohardness measurements by Vickers indentation method showed that the HV30 of TiB_2 -TiB-Ti composite is 13.24 ± 0.18 GPa. The indentation fracture toughness of the composite was calculated as 10.5 ± 0.5 $MPa \cdot m^{1/2}$ using Palmqvist Crack method. The fracture toughness value of ceramic based TiB_2 -TiB-Ti composite is commensurate with titanium based composite TiB_w -60wt.% Ti (IFT = 9.35 $MPa \cdot m^{1/2}$, Table 1.3) [37].

Fig. 3.6d demonstrates the coefficient of friction and average volumetric wear of pure Ti and the produced TiB_2 -TiB-Ti composite by sliding test. It is clearly seen that Ti-B reinforcement contributes to the wear behavior of the composite and is preferable compared to pure Ti. A significant drop in CoF and wear at elevated temperature ($700^\circ C$ - $900^\circ C$) is noted. At 700 - $900^\circ C$ a lubricating boric acid $B(OH)_3$ characterized by a glass layer is formed on the composite surface (Fig. 3.6a-c). TiB oxidizes forming boron oxide (B_2O_3) starting from $700^\circ C$ in air and the spontaneous chemical reaction between water molecules and the B_2O_3 coating in a humid environment leads to the formation of $B(OH)_3$ film according to the chemical reaction:



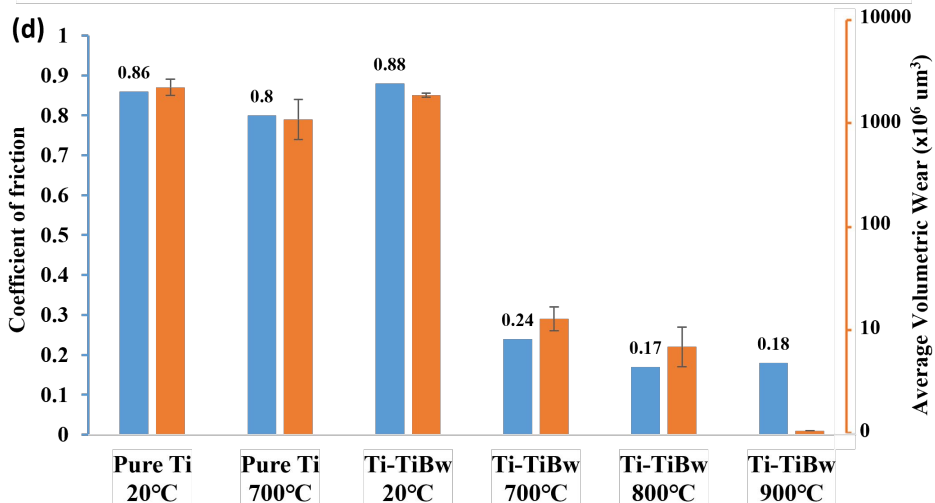
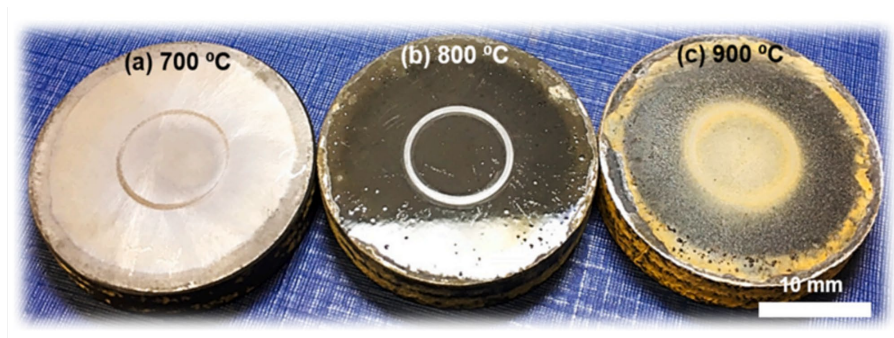


Figure 3.6 Ti-TiB_w Composite surfaces after sliding test (a) minimal glazed layer, 700°C; (b) maximum glazed layer, 800°C; (c) faded glazed layer after cooling, 900°C and (d) Coefficient of friction and average volumetric wear at several test temperatures (adapted from Publication 1).

3.2.2 SPS of SHS-ed Ti-B powder (Feedstock 2)

SHSed Ti-B powder comprising TiB, TiB₂ and free Ti phases was subjected to SPS to consolidate the same size specimens as from commercial Ti and TiB₂ mixture. Fig. 3.7a illustrates the SEM image of SHS-SPSed composite indicating the distribution of two phases - TiB phase (grey) together with free Ti (white). The both SHS and SPS processes promoted the $\text{Ti} + \text{TiB}_2 \rightarrow 2\text{TiB}$ interaction and complete formation of TiB phase in Ti matrix. XRD pattern (Fig. 3.7b) of SPSed bulk composite derived from the polished surface confirms the presence of only TiB and Ti with concentrations of 87.8% and 12.2%, respectively, calculated by the Rietveld refinement method. In addition, according to the XRD patterns the peaks' width was narrowed after SPS revealing the enhancement of crystallinity of the phases. Compared to the TiB-Ti composite produced by SPS from the conventionally mixed commercially available powders of Ti and TiB₂ (Fig. 3.5), the product is more homogeneous, although they own similar densities, which results in improved mechanical and tribological features. The relative Archimedes density is calculated to be 99.7%, and hardness is 1550 ± 26 HV30 for the TiB-Ti composite obtained by the conjugation of SHS and SPS processes. The Vickers hardness of pure TiB is about 1800, therefore, the hardness value for the current TiB rich composite is relatively higher in comparison to several published data (Table 1.3).

Apart from the high hardness, an enhanced IFT value in the current composite ($8.16 \pm 0.5 \text{ MPa} \cdot \text{m}^{1/2}$) is observed due to the presence of 0.2 mole extra Ti in the composite as per design. In general, it is extremely difficult to produce a composite material with a high content of ceramic phase (here TiB) showing a commendable IFT value. This is also obvious from Table 1.3 demonstrating decrease in the IFT, as well as density values of the composite with the increase in ceramic content. A higher relative density and IFT values of the composite under study with high ceramic content is attributed to reactive SPS and in-situ formation of TiB phase.

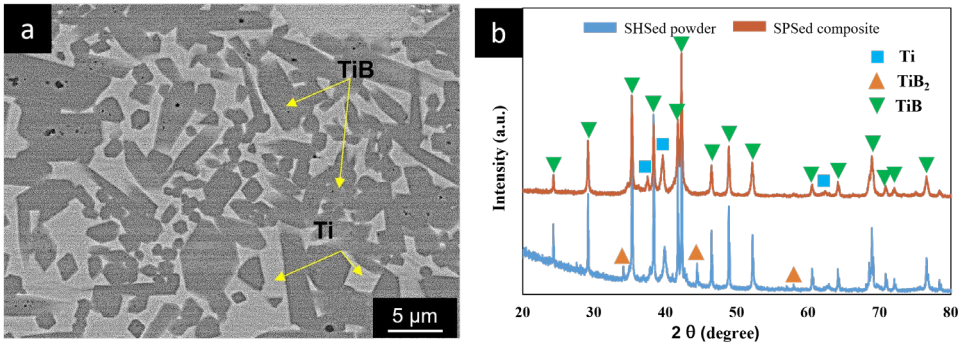


Figure 3.7 (a) SEM image of SPSed composite; and (b) XRD patterns of SHSed powder and SPSed composite (**adapted from Publication II**).

The volumetric wear and coefficient of friction tested at different temperatures (RT, 800°C) and loads (5 N, 20 N) are shown in Fig. 3.8. As expected, at room temperature, higher CoF and higher wear rate of TiB-Ti specimen was recorded; while at a temperature of 800°C, a lower CoF and a decrease in the wear rate of the material was demonstrated. This can be explained by the change in the wear mechanism and the formation of a new phase (B_2O_3) at the test temperature (the same mechanism occurs as for specimens from SPS of commercial Ti and TiB_2 mixture). Compared with the test stabilization time at room temperature (3000 s), the time required for the stabilization of CoF at high temperature is substantially reduced (100 s, Fig. 3.8b). The range of CoF fluctuation and the stabilization time are affected by the mechanical properties of the material, the formation mechanism of the friction layer and the surface treatment (defects, roughness, presence of a small contaminants, etc.). Grinding and the forming of a characteristic friction layer is an indispensable process that affects the following steady-state wear mechanism and final wear rate.

It is worth noting that at 800°C, the running-in period is very short regardless of low or high sliding loads. It is worth mention that at 800°C, especially at the maximum test load (20 N), the CoF is the lowest (Fig. 3.8b), and there is no substantial increase in each sliding cycle. This phenomenon leads to the conclusion that the interval between sliding oxidation is favored to friction coupling.

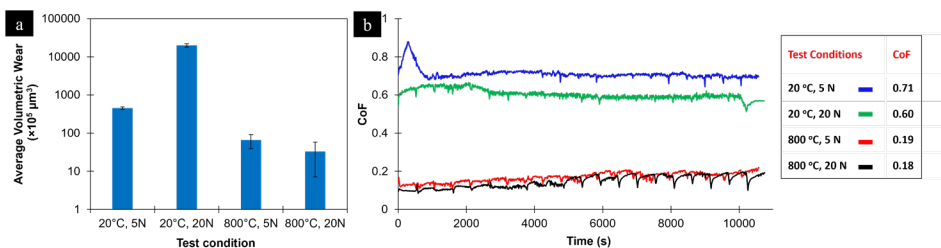


Figure 3.8 Effect of temperature and load on evolution of (a) volumetric wear and (b) coefficient of friction (adapted from Publication II).

3.3 Selective laser melting

3.3.1 SLM of commercial Ti and TiB₂ Powder mixtures (Feedstock 1)

Although Ti-B based samples sintered by SPS show encouraging properties, but lack of geometric flexibility prevents their further extensive applications. Hence, 3D printing via SLM was chosen to directly manufacture near net shape products. As the first step, cylindrical bulks and lattices were printed from 50wt.%Ti-50wt.%TiB₂ commercial powder mixtures. The laser current and scanning speed were adjusted to get an optimized quality of the printed parts.

Bulks

SEM images of the polished samples obtained from commercial Ti and TiB₂ powder mixtures (S1-S15) are depicted in Fig. 3.9. Laser current of 1500-3500 mA and scanning speeds of 500 mm·s⁻¹, 290 mm·s⁻¹ and 80 mm·s⁻¹ were applied for the consolidation.

The samples printed by highest applied scanning speed (500 mm·s⁻¹) possess open pores pointed with green arrows. Their formation is justified by the lack of fusion of the powder (samples S1, Fig. 3.9a) and high viscosity of the melt pool handicapping the adequate flow to the desired regions. Besides the porosity formation, it is important to consider the new phases formation and their distribution. During the laser treatment TiB new phase formation was observed (pointed with yellow arrows). It is visible that tiny needle type TiB and the unreacted TiB₂ (marked with pink arrows) co-exist in most of the samples (S3, S4 and S5). At higher laser scanning speed the irradiation is very quick (less than 40 μs in each exposure point), which results to a short lifetime of the blended melt pool, thus hindering the reactions between molten Ti and TiB₂ interface. The latter results in pores, that are located between TiB₂ particles and titanium melt and are irregular in form (pointed with orange arrows).

Samples sintered at moderate-scanning speed (290 mm·s⁻¹), have smoother surface with less pores compared to the first set. However, when the applied laser current is relatively lower, TiB is present in the form of colonies inhomogeneously distributed among Ti and alongside TiB₂ (samples S6-S8). At higher laser current (>3000 mA), the needle shaped TiB particles are firmly apportioned in the material (samples S9 and S10). The TiB needles are with width of 2-5 μm and length up to 50 μm. The neighboring needles have parallel direction, but overall distribution is random.

At slow scanning process (80 mm·s⁻¹), the phase transformation induced pores increased. Applying excess energy caused the formation of the dominating TiB phase

and the morphology of needles became coarser and uneven (samples S14 and S15). The absence of metallic titanium result in the brittleness of the sample, pores became inevitable in the ceramic rich areas.

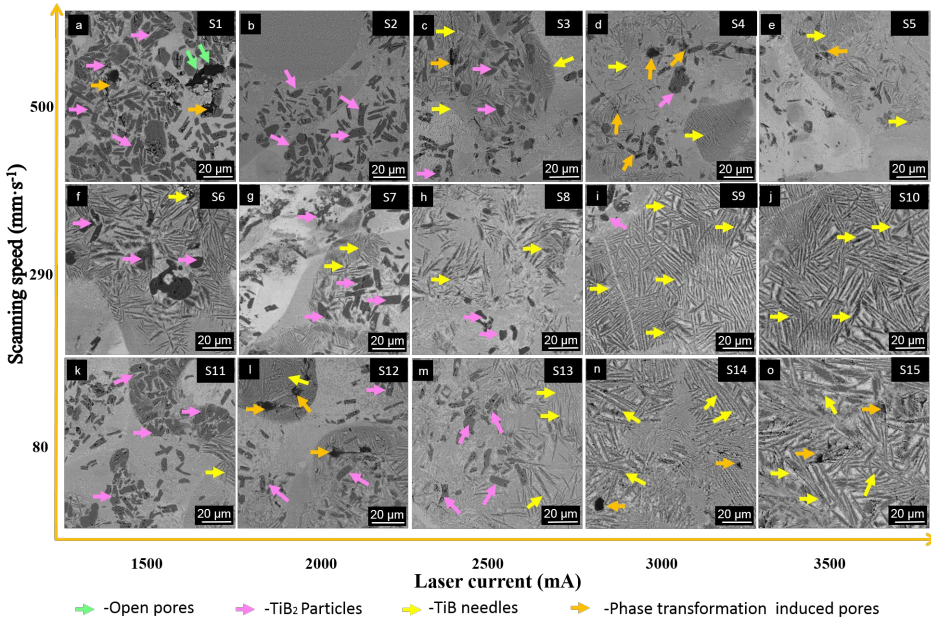


Figure 3.9 Top surface microstructure of polished TiB₂-Ti samples prepared at different scanning speed and laser current (**adapted from Publication III**).

To demonstrate the change in phase composition according to scanning speed and laser current, XRD patterns were quantified by Rietveld refinement method. According to Fig. 3.10b, the tendency of increase in TiB amount in samples S1-S5 and S11-S15 was observed demonstrating the crucial role of the laser current on the TiB formation. The samples scanned at the same laser current, but different scanning speed (500 mm·s⁻¹ and 80 mm·s⁻¹), e.g. S1 with S11 or S5 with S15, demonstrate moderate difference in TiB content. From thermodynamic-kinetic point of view, it manifests that the main phase transformation from TiB₂ to TiB is regulated by the achieved temperature rather than the keeping time, and needle colonies are influenced by the cooling process. In SLM process, laser power is determining factor for the temperature, and the scanning speed mainly controls the lifetime of the melting pool. For instance, at shorter laser exposure time (fast scanning speed) the holding time is short and the cooling rate is fast, TiB needles are thin and tiny; while at slow scanning speed, the melting pool holding duration is longer and the cooling rate is slower, thus TiB needles have more time to grow in preferred direction.

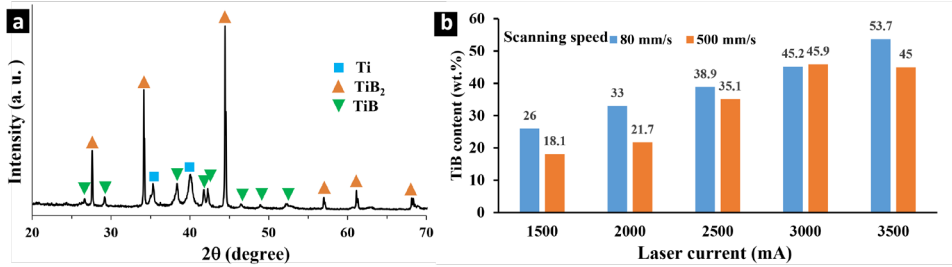


Figure 3.10 (a) Typical XRD pattern and (b) the TiB content (wt.%) in the samples sintered at scanning speed of 80 mm·s⁻¹ (S1-S5) and 500 mm·s⁻¹ (S11-S15) according to Rietveld refinement method from XRD patterns (**adapted from Publication III**).

The density and hardness of the produced TiB₂-TiB-Ti composites are listed in Table 3.3. For sample S1, due to high porosity (Fig. 3.9a), the hardness measurement is unreliable. Overall, the hardness value shows an increasing tendency with the increasing of LED. The highest hardness of around 20.4 GPa achieved for S15 is comparable with hardness of fully dense TiB₂ - based composites. The density of SLM samples increase with the decrease of the scanning speed. For example, the density of samples S11-S15 sintered at 80 mm·s⁻¹ scanning speed is obviously higher in comparison with the samples S1-S5 sintered at 500 mm·s⁻¹. In general, increasing of LED can generate a larger area of melting pool during laser scanning, which results in a denser and harder specimen.

Table 3.3 Density and hardness of the TiB₂-TiB-Ti composites (**adapted from Publication III**).

Sample	S1	S2	S3	S4	S5	S6	S7	S8	S9	S10	S11	S12	S13	S14	S15
LED (J·mm ⁻³)	48	64	80	96	112	84	112	140	168	196	300	400	500	600	700
Relative Density (%)	~77	~83	~86	~85	~86	~82	~84	~86	~87	~87	~89	~88	~90	~91	~92
HV5 (GPa)	-	5.5 ±0.7	9.5 ±2.3	9.4 ±2.7	9.6 ±1.7	5.7 ±1.0	7.1 ±0.8	9.6 ±1.2	12.1 ±1.1	13.1 ±1.8	9.4 ±2.5	10.7 ±1.5	11.8 ±2.0	17.2 ±3.2	20.4 ±2.5

Lattices

Lattice structures produced from TiB₂-Ti powder mixtures are depicted in Fig. 3.11. The SEM images of the as-built structures show that the pore sizes are varied in a range of 550 to 630 μm, and the strut diameters are between 510 and 560 μm (Fig. 3.11b and e). The phase composition of the lattices after sintering is similar to the bulk samples. The formation of TiB phase coexisting with TiB₂ and Ti after the SLM processing is demonstrated in Fig. 3.11c. After sintering the TiB₂-TiB-Ti lattices were nitridized in the high-temperature furnace in nitrogen atmosphere to obtain fully ceramic composite. Nitridation of TiB₂-TiB-Ti lattices leads to yellow-brownish appearance pointing out the generation of TiN phase at the expense of free titanium (Fig. 3.11f). According to phase

composition analysis of the lattices (Table 3.5) an increase of TiB and decrease of TiB₂ content is attributed to Ti participation in formation of both TiN and TiB phases according to TiB₂ + Ti → 2TiB reaction started during room temperature ball milling; and 2Ti + N₂ → 2TiN reaction at T > 800°C. The in-situ chemical reactions immediately during the laser sintering have tendency to build up and maintain the designed structures.

The change in dimensions of lattices after the nitridation process was not noticeable (Fig. 3.11a and d) as the densities and coefficient of thermal expansion (CTE) of materials before and after nitridation are similar (Table 3.4).

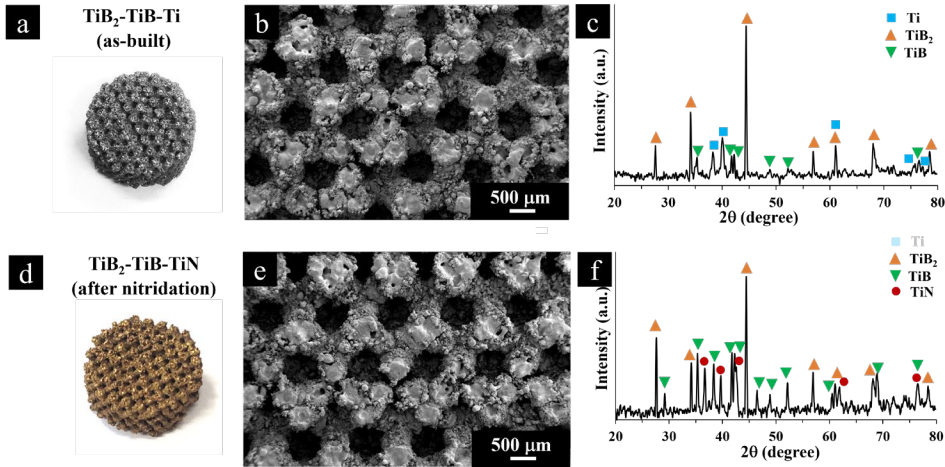


Figure 3.11 (a,b,c) General view, SEM images and XRD pattern of the as-built TiB₂-TiB-Ti lattice and (d,e,f) TiB₂-TiB-TiN lattice after nitridation (adapted from Publication IV).

Table 3.4 Density and thermal expansion of TiN, TiB₂, TiB and Ti (adapted from Publication IV).

Compound	Density (g·cm ⁻³)	Thermal expansion (°C ⁻¹)
TiN	5.22	~9.35×10 ⁻⁶
TiB ₂	4.52	~7.2 × 10 ⁻⁶
TiB	4.56	~7.15 × 10 ⁻⁶
Ti	4.506	8.4-10.8×10 ⁻⁶

Table 3.5 Phase composition of lattices after SLM and nitridation (adapted from Publication IV).

Phase Composition	Content (wt.%)	
	After SLM	After nitridation
Ti	21.1	0
TiB ₂	46.3	23.5
TiB	32.6	37.3
TiN	0	39.2

To evaluate the structural integrity of the samples, as well as their applicability in spongy bone regeneration, the compressive stress - strain measurements of the produced structures were conducted (Fig. 3.12). As shown in the curve, the first peak (Fig.3.12a)

is normally related to some struts crack, so the overall load-bearing capacity is comparatively low, but thanks to the lattice structure, the crack didn't propagate directly through adjacent struts avoiding the entire failure of the ceramic specimen immediately during the compression process. The compressive strengths were recorded as 7 MPa and 3.5 MPa (Fig. 3.12), while compressive strain results were 24.4% and 20.5%, respectively for TiB₂-TiB-Ti lattices before and after the nitridation. TiB₂-TiB-Ti lattices shows a higher strength value because the metallic titanium can absorb the stress better compared to ceramic TiN.

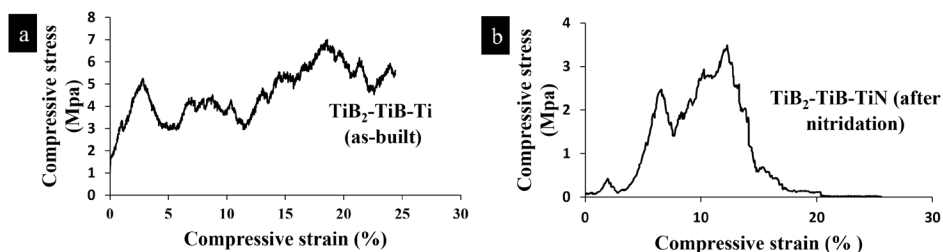


Figure 3.12 Compressive stress - strain curves of (a) as build TiB₂-TiB-Ti lattice and (b) nitridized TiB₂-TiB-TiN lattice (adapted from Publication IV).

The natural trabecular bone of 64% porosity and 750±250 μm pores possesses a compressive strength of 4.1±1.9 MPa [70]. In comparison, the produced TiB₂-TiB-TiN lattice maintain similar properties, so as a potential application, it may be considered as a substitute for filling and rebuilding the bone cavity or bone loss area caused by trauma or other bone disease.

3.3.2 SLM of SHS-ed Ti-B-Si powder (Feedstock 3)

Although the 3D printing from Ti and TiB₂ commercial powder is promising, TiB₂ is consumed during the in-situ reaction process with Ti. In order to produce composites with high content of TiB₂ by SLM, another SHS system was considered. Si was chosen as the binder material due to good laser absorption properties at the applied wave length (41% for 1070 nm Yb:YAG fiber laser) and TiB₂-Si composite powders (Feedstock 3) were produced from SHS of Ti, B and Si mixture.

Bulk cylindrical samples with 10 mm diameter and 5 mm height were built by SLM for the process parameter optimization. The microstructure of the TiB₂-Si bulks printed using different laser currents are shown in Fig. 3.13.

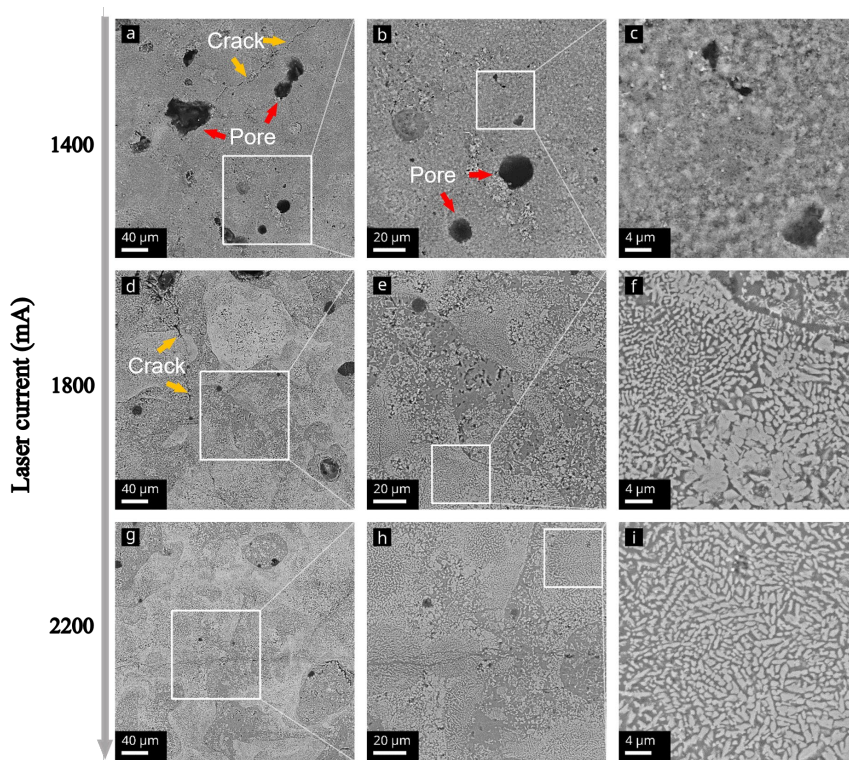


Figure 3.13 Polished top surface SEM images of TiB_2 -Si bulks produced at (a-c) 1400 mA , (d-f) 1800 mA and (g-i) 2200 mA laser current (**adapted from publication V**).

Table 3.6 specifies the geometric density of 56wt.% TiB_2 -44wt.%Si system produced at a laser current of 1400 to 2200 mA. It is obvious that the densification level is improving with increase in the laser current. The highest geometric density of the bulk was achieved to be $3.05 \text{ g}\cdot\text{cm}^{-3}$. Considering the theoretical density of 56wt.% TiB_2 -44wt.%Si material ($3.19 \text{ g}\cdot\text{cm}^{-3}$), the calculated relative density reaches 97%.

Table 3.6 Geometric density and hardness values of produced TiB_2 -Si bulk (**adapted from publication V**).

Sample	Laser current (mA)	Geometric density ($\text{g}\cdot\text{cm}^{-3}$)	Relative density (%)	HV1 (GPa)
C1	1400	2.77	87	-
C2	1800	2.86	90	4.4 ± 1.0
C3	2200	3.05	97	7.6 ± 1.0

At laser current of 1400 mA (Sample C1, Fig. 3.13a-c), the non-spherical (irregular shape) pore formation is confirmed by the applied inadequate energy input to completely melt the raw material and promote consolidation. When the supplied power is insufficient, not fully fused zone caused by un-melted powder particles near the holes can be found. In the PBF process, in order to ideally perform sintering, the powder on the top of the sintered layer should absorb enough laser energy to melt a certain thickness of the spreading layer. However, insufficient energy input can result in a reduction in the size of the molten pool, and therefore inadequate melting of the

powder particles and/or spalling of the previously solidified layer. Under medium laser current (Sample C2, 1800 mA Fig. 3.13d-f), samples with smoother surface and higher density can be produced. In the morphology, fusion defects were observed in samples generated under a laser current of 1400-1800 mA. Spherical pores caused by the release of absorbed gas or the evaporation of the melt silicon were identifiable in both specimens. The overall microstructure of the sample prepared under a laser current of 2200 mA (Sample C3) is almost crack-free, and it is mainly composed of columnar grains with an average spacing in the sub-micron range (Fig. 3.13i). These grains follow the deposition direction due to the high thermal cooling gradient (up to 10^3 - 10^8 K·s⁻¹).

It is well-known that the residual porosity has dramatic influence on the hardness. For samples produced with lower laser current (1400 mA), it was impossible to measure a reliable hardness value due to high porosity. As expected, the hardness of the sample C3 is higher than that of the sample C2. The production of high-density and high-hardness materials requires high-intensity laser current ($I=2200$ mA). Due to larger/deeper melt pools, the sample C3 printed with high energy input shows improved particle connections. The immediate penetration of liquid silicon into the pores during laser treatment means that when the contact angle is small, the silicon is ready to wet TiB₂, which limits the removal of TiB₂ solid inclusions from the silicon. The increase in laser current results in acceleration of the movement and flowability of the melt, hence improved the infiltration of silicon through the “pomegranate-like” structural entities in the raw material. On the other hand, thanks to the “pomegranate-like” morphology of the precursor, the ultrafine-grained TiB₂ particles act as nucleation centers during the cooling process, contributing to uniform solidification of molten silicon.

The SEM image and EDS mapping of the produced TiB₂-Si solid parts are shown in Fig. 3.14 a-e. The microstructure of the composites consists of TiB₂ with relatively large columnar grains with 2-10 microns length and numerous sub-micron equiaxed grains distributed along the silicon matrix. Hence, during the laser scanning, the TiB₂ particles demonstrate high affinity for viscous silicon, thereby promoting the sintering and consolidation processes. Furthermore, the XRD pattern of the produced sample shows that no other phases are formed in the 3D printing process regardless of the laser treatment (Fig. 3.14f).

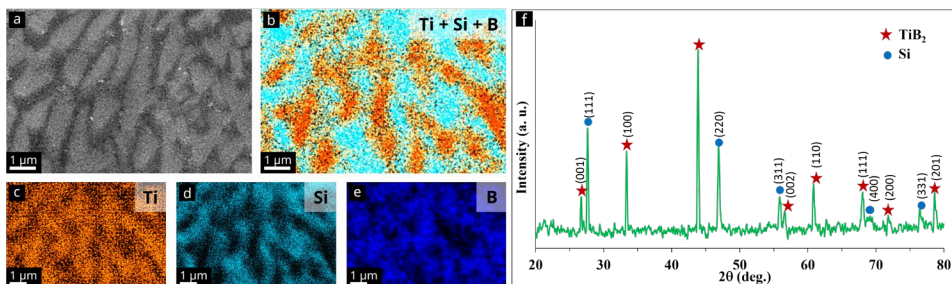


Figure 3.14 (a) SEM image, (b-e) EDS mapping and (f) XRD pattern of selective laser melted TiB₂-Si composite (**adapted from publication V**).

During SPS and SLM of SHSed powders the relatively fine TiB or TiB₂ particles incorporated in the titanium or silicon matrix structure, increased the extent of nucleation sites providing new interfaces between Ti and TiB, Si and TiB₂ for grain growth inhibition and enhancement of microstructural homogeneity and mechanical properties.

4 Conclusions

As a consistent result of the main objectives, i.e. design and producing of newly developed Ti-B based feedstocks suitable for advanced consolidation by spark plasma sintering and selective laser melting to produce qualified composites, the following conclusions were drawn:

1. Findings/results in feedstock production (SHS process):

A powder of TiB-Ti (Feedstock 2) was developed for SPS process from SHS of pure boron and titanium at the combustion temperature of 1700°C. It demonstrates the co-existence of agglomerates of fine and coarse particles of either rounded or needle-like morphology. Boron tends to center segregation with subsequent precipitation from molten solution of Ti and B, the TiB needles mostly grow towards the center. The powder is relatively fine ($D_{50}=8.98\ \mu\text{m}$) and suitable for producing homogenous composite bulks.

A TiB₂-Si powder (Feedstock 3) in “pomegranate-like” structured was prepared for the first time by SHS at a combustion temperature of 1530°C. The powder particulates consist of a great number of TiB₂ particles in nanoscale and “glued” together by silicon binder. The “pomegranate-like” powders consisting particles in the range of 20-45 μm demonstrated fair flowability and high efficiency for manufacturing solid bulks via SLM without any post-treatment/atomization.

2. Results about composites produced by SPS:

A fully dense TiB_w-Ti composite was in-situ produced from commercial powders (TiB₂-Ti, feedstock 1) by spark plasma sintering at 1500°C, pressure of 35 MPa for a dwell time of 3 min. Samples demonstrated 1324 ± 18 (HV30) hardness and IFT of $10.52\ \text{MPa}\cdot\text{m}^{1/2}$.

A fully dense and thermodynamically stable 88 wt.%TiB-Ti composites were fabricated by spark plasma sintering from SHS prepared TiB-Ti powders (Feedstock 2). The samples were successfully densified by spark plasma sintering at a relatively low temperature of 1200°C with the application of 50 MPa pressure during 3 min in vacuum. They exhibited the hardness of ~ 1550 HV30 integrated with a good IFT of $8.16\ \text{MPa}\cdot\text{m}^{1/2}$.

Both TiB_w-Ti and TiB-Ti composites exhibit a considerably low coefficient of friction (~ 0.2) at elevated temperature (700-900°C) due to development of protective lubricious boric acid tribo-layers of a high load bearing capacity from 700°C.

The spark plasma sintered samples from SHS prepared TiB-Ti powders showed more homogeneous microstructure, therefore improved mechanical and tribological features as compared to the samples sintered from commercial TiB₂-Ti powders.

3. Results about SLM of bulks and lattice structures:

(i). TiB₂-TiB-Ti (with 18-54 wt.%TiB) composite bulks were SLM fabricated from commercially available 50 wt.%TiB₂-50 wt.%Ti powder mixture (Feedstock 1). The size and fraction of TiB needle-like colonies were governed by the laser energy density. The sintering at high laser current (3500 mA) and relatively slow scanning speed ($80\ \text{mm}\cdot\text{s}^{-1}$) resulted in bulks of ~ 20.4 GPa hardness, being comparable with ceramic composites produced by SPS method. SLM fabrication of TiB₂-Ti powders led to the needle shaped TiB particles with width of 2-5 μm and length up to 50 μm firmly apportioning in parallel directions.

The TiB₂-TiB-Ti cellular structures were successfully SLM fabricated exploiting the laser current of 2000 mA corresponding to the laser energy density (LED) of $400\ \text{J}\cdot\text{mm}^{-3}$.

Nitridation of the structures resulted in the development of the TiB₂-TiB-TiN ceramic lattices without significant deterioration of the geometrical parameters of the designed product. The composites of TiB₂-TiB-TiN, comprising the similar properties of trabecular bone (porosity, strength, etc.), may be considered as the potential substitutes to fill and reconstruct bone cavities or areas of bone loss caused by traumas or bone disease.

(ii). The 56 wt.%TiB₂-44 wt.%Si composites with a relative density of ~97% and hardness of ~7.6 GPa (HV1) were fabricated from SHS-derived “pomegranate-like” powders (Feedstock 3) using a 2200 mA laser current at 80 mm·s⁻¹ scanning speed. After SLM process the overall microstructure of the sample was almost crack-free, consisting of relatively large (2-10 μm) columnar and numerous of sub-micron equiaxed TiB₂ grains distributed in a silicon matrix.

5 Future work

Continuing the research briefly introduced in the thesis, more profound study have to be considered in the future:

- combustion synthesis and microstructure evolution of Ti-B based composite materials with other elements, such as carbon, aluminum and nickel as binder phases; the influence of Ni-Ti, Ni-B, Ti-C, B-C in-situ generated phases formation on the microstructural homogeneity of the powders
- selective laser sintering and spark plasma sintering of SHS derived Ti-B-C, Ti-B-Al, Ti-B-Ni composite materials, optimization of sintering procedure, recommendation for prospective applications.

Reference

- [1] V. Mamedov, "Spark plasma sintering as advanced PM sintering method," *Powder Metallurgy*, vol. 45, p. 322-328, 2002.
- [2] S. & D. M. Ford, "Additive manufacturing and sustainability: an exploratory study of the advantages and challenges," *Journal of cleaner Production*, vol. 137, no. 1, pp. 573-1587, 2016.
- [3] Wohlers Report, "3D printing and additive manufacturing, State of the industry," Wohlers Associates, 2019.
- [4] B. R. Bhat, J. Subramanyam and V. B. Prasad, "Preparation of Ti-TiB-TiC & Ti-TiB composites by in-situ reaction hot pressing," *Materials Science and Engineering: A*, vol. 325, p. 126-130, 2002.
- [5] S. A. Delbari, A. S. Namini and M. S. Asl, "Hybrid Ti matrix composites with TiB₂ and TiC compounds," *Materials Today Communications*, vol. 20, p. 100576, 2019.
- [6] L. G. Zhen and L. R. Ze, "Non-aerospace application of Ti materials with a great many social and economic benefits in China," *Materials Science and Engineering: A*, vol. 280, p. 25-29, 2000.
- [7] A. S. Konstantinov, P. M. Bazhin, A. M. Stolin, E. V. Kostitsyna and A. S. Ignatov, "Ti-B-based composite materials: Properties, basic fabrication methods, and fields of application," *Composites Part A: Applied Science and Manufacturing*, vol. 108, p. 79-88, 2018.
- [8] M. Oghbaei and O. Mirzaee, "Microwave versus conventional sintering: A review of fundamentals, advantages and applications," *Journal of alloys and compounds*, vol. 494, p. 175-189, 2010.
- [9] D. Roberson, C. M. Shemelya, E. MacDonald and R. Wicker, "Expanding the applicability of FDM-type technologies through materials development," *Rapid Prototyping Journal*, 2015.
- [10] J. Subrahmanyam and M. Vijayakumar, "Self-propagating high-temperature synthesis," *Journal of Materials Science*, vol. 27, p. 6249-6273, 1992.
- [11] A. G. Merzhanov, "Self-propagating high-temperature synthesis: twenty years of search and findings," *Combustion and plasma synthesis of high-temperature materials*, p. 1-53, 1990.
- [12] C. T. S. R. Subramanian, T. C. Murthy and A. K. Suri, "Synthesis and consolidation of titanium diboride," *International Journal of Refractory Metals and Hard Materials*, vol. 25, p. 345-350, 2007.
- [13] B. Buyuk, Y. Goncu, A. B. Tugrul and N. Ay, "Swelling on neutron induced hexagonal boron nitride and hexagonal boron nitride-titanium diboride composites," *Vacuum*, vol. 177, p. 109350, 2020.
- [14] T. Jüngling, L. S. Sigl, R. Oberacker, F. Thümmel and K. A. Schwetz, "New hardmetals based on TiB₂," *International Journal of Refractory Metals and Hard Materials*, vol. 12, p. 71-88, 1993.
- [15] T. C. Murthy, J. K. Sonber, C. Subramanian, R. K. Fotedar, M. R. Gonal and A. K. Suri, "Effect of CrB₂ addition on densification, properties and oxidation resistance of TiB₂," *International Journal of Refractory Metals and Hard Materials*, vol. 27, p. 976-984, 2009.

- [16] J. Li, L. Liu, S. Xu, J. Zhang and W. She, "First-principles study of mechanical, electronic properties and anisotropic deformation mechanisms of TiB under uniaxial compressions," *Applied Physics A*, vol. 125, p. 1-10, 2019.
- [17] X. Ma, C. Li, Z. Du and W. Zhang, "Thermodynamic assessment of the Ti-B system," *Journal of alloys and compounds*, vol. 370, p. 149-158, 2004.
- [18] L. Sun, Y. Gao, B. Xiao, Y. Li and G. Wang, "Anisotropic elastic and thermal properties of titanium borides by first-principles calculations," *Journal of Alloys and Compounds*, vol. 579, p. 457-467, 2013.
- [19] B. Huang, Y.-H. Duan, W.-C. Hu, Y. Sun and S. Chen, "Structural, anisotropic elastic and thermal properties of MB (M= Ti, Zr and Hf) monoborides," *Ceramics International*, vol. 41, p. 6831-6843, 2015.
- [20] K. E. Spear, P. Mcdowell and F. McMahan, "Experimental evidence for the existence of the Ti₃B₄ phase," *Journal of the American Ceramic Society*, vol. 69, p. C-4, 1986.
- [21] D. Zhou, Y. Liu, B. Shen, X. Zhao, Y. Xu and J. Tian, "Structural prediction of ultrahard semi-titanium boride (Ti₂B) using the frozen-phonon method," *Physical Chemistry Chemical Physics*, vol. 18, p. 7927-7931, 2016.
- [22] B. Basu, G. B. Raju and A. K. Suri, "Processing and properties of monolithic TiB₂ based materials," *International materials reviews*, vol. 51, p. 352-374, 2006.
- [23] Z. Fu, Synthesis, processing, and characterization of titanium carbide and titanium diboride based materials for structural and electronic application, Southern Illinois University at Carbondale, 2016.
- [24] Y. S. Kang, S. H. Kang and D. J. Kim, "Effect of addition of Cr on the sintering of TiB₂ ceramics," *Journal of materials science*, vol. 40, p. 4153-4155, 2005.
- [25] J. Jaroszewicz and A. Michalski, "Preparation of a TiB₂ composite with a nickel matrix by pulse plasma sintering with combustion synthesis," *Journal of the European Ceramic Society*, vol. 26, p. 2427-2430, 2006.
- [26] M. Ziemnicka-Sylwester, "Vaporization and Poor Wettability as the Main Challenges in Fabrication of TiB₂-Cu Cermets Studied by SPS," *Metals*, vol. 4, p. 623-638, 2014.
- [27] M. S. Asl, Z. Ahmadi, S. Parvizi, Z. Balak and I. Farahbakhsh, "Contribution of SiC particle size and spark plasma sintering conditions on grain growth and hardness of TiB₂ composites," *Ceramics International*, vol. 43, p. 13924-13931, 2017.
- [28] A. Li, Y. Zhen, Q. Yin, L. Ma and Y. Yin, "Microstructure and properties of (SiC, TiB₂)/B₄C composites by reaction hot pressing," *Ceramics international*, vol. 32, p. 849-856, 2006.
- [29] S. K. Bhaumik, C. Divakar, A. K. Singh and G. S. Upadhyaya, "Synthesis and sintering of TiB₂ and TiB₂-TiC composite under high pressure," *Materials Science and Engineering: A*, vol. 279, p. 275-281, 2000.
- [30] G. J. Zhang, Z. Z. Jin and X. M. Yue, "Effects of Ni addition on mechanical properties of TiB₂/SiC composites prepared by reactive hot pressing (RHP)," *Journal of materials science*, vol. 32, p. 2093-2097, 1997.
- [31] A. S. Namini, M. Azadbeh and M. S. Asl, "Effect of TiB₂ content on the characteristics of spark plasma sintered Ti-TiB_w composites," *Advanced Powder Technology*, vol. 28, p. 1564-1572, 2017.

- [32] J. Schmidt, M. Boehling, U. Burkhardt and Y. Grin, "Preparation of titanium diboride TiB₂ by spark plasma sintering at slow heating rate," *Science and Technology of Advanced Materials*, vol. 8, p. 376, 2007.
- [33] A. Turan, F. C. Sahin, G. Goller and O. Yucel, "Consolidation of TiB₂ Ceramics by using Spark Plasma Sintering," in *TMS 2014: 143rd Annual Meeting & Exhibition*, 2014.
- [34] L. Zheng, F. Li and Y. Zhou, "Preparation, microstructure, and mechanical properties of TiB₂ using Ti₃AlC₂ as a sintering aid," *Journal of the American Ceramic Society*, vol. 95, p. 2028-2034, 2012.
- [35] S. R. Bakshi and others, "Reactive spark plasma sintering and mechanical properties of zirconium Diboride-titanium Diboride ultrahigh temperature ceramic solid solutions," *Technologies*, vol. 4, p. 30, 2016.
- [36] H. Attar, M. Bönisch, M. Calin, L.-C. Zhang, S. Scudino and J. Eckert, "Selective laser melting of in situ titanium-titanium boride composites: processing, microstructure and mechanical properties," *Acta Materialia*, vol. 76, p. 13-22, 2014.
- [37] Z.-h. Zhang, X.-B. Shen, S. Wen, J. Luo, S.-k. Lee and F.-c. Wang, "In situ reaction synthesis of Ti-TiB composites containing high volume fraction of TiB by spark plasma sintering process," *Journal of Alloys and Compounds*, vol. 503, p. 145-150, 2010.
- [38] Z. Xinghong, X. Qiang, H. Jiecai and V. L. Kvanin, "Self-propagating high temperature combustion synthesis of TiB/Ti composites," *Materials Science and Engineering: A*, vol. 348, p. 41-46, 2003.
- [39] C. Hu, F. Li, D. Qu, Q. Wang, R. Xie, H. Zhang, S. Peng, Y. Bao and Y. Zhou, "Developments in hot pressing (HP) and hot isostatic pressing (HIP) of ceramic matrix composites," in *Advances in Ceramic Matrix Composites*, Elsevier, 2014, p. 177-202.
- [40] F. B. Swinkels, D. S. Wilkinson, E. Arzt and M. F. Ashby, "Mechanisms of hot-isostatic pressing," *Acta Metallurgica*, vol. 31, p. 1829-1840, 1983.
- [41] O. Guillon, J. Gonzalez-Julian, B. Dargatz, T. Kessel, G. Schierning, J. Räthel and M. Herrmann, "Field-assisted sintering technology/spark plasma sintering: mechanisms, materials, and technology developments," *Advanced Engineering Materials*, vol. 16, p. 830-849, 2014.
- [42] Z. A. Munir, U. Anselmi-Tamburini and M. Ohyanagi, "The effect of electric field and pressure on the synthesis and consolidation of materials: A review of the spark plasma sintering method," *Journal of materials science*, vol. 41, p. 763-777, 2006.
- [43] I. Gibson, D. Rosen, B. Stucker and M. Khorasani, *Additive manufacturing technologies*, vol. 17, Springer, 2014.
- [44] W. E. Frazier, "Metal additive manufacturing: a review," *Journal of Materials Engineering and performance*, vol. 23, p. 1917-1928, 2014.
- [45] K. V. Wong and A. Hernandez, "A review of additive manufacturing," *International scholarly research notices*, vol. 2012, 2012.
- [46] F. Doreau, C. Chaput and T. Chartier, "Stereolithography for manufacturing ceramic parts," *Advanced Engineering Materials*, vol. 2, p. 493-496, 2000.

- [47] A. S. T. M. Standard and others, "Standard terminology for additive manufacturing technologies," *ASTM International F2792-12a*, 2012.
- [48] B. Khoshnevis, D. Hwang, K.-T. Yao and Z. Yeh, "Mega-scale fabrication by contour crafting," *International Journal of Industrial and Systems Engineering*, vol. 1, p. 301-320, 2006.
- [49] J. Park, M. J. Tari and H. T. Hahn, "Characterization of the laminated object manufacturing (LOM) process," *Rapid Prototyping Journal*, 2000.
- [50] M. Ziaee and N. B. Crane, "Binder jetting: A review of process, materials, and methods," *Additive Manufacturing*, vol. 28, p. 781-801, 2019.
- [51] I. Gibson, D. Rosen and B. Stucker, "Directed energy deposition processes," in *Additive manufacturing technologies*, Springer, 2015, p. 245-268.
- [52] Y. He, R. D. Wildman, C. J. Tuck, S. D. R. Christie and S. Edmondson, "An investigation of the behavior of solvent based polycaprolactone ink for material jetting," *Scientific reports*, vol. 6, p. 1-10, 2016.
- [53] S. Sun, M. Brandt and M. Easton, "Powder bed fusion processes: An overview," *Laser additive manufacturing*, p. 55-77, 2017.
- [54] F. Fina, S. Gaisford and A. W. Basit, "Powder bed fusion: The working process, current applications and opportunities," in *3D printing of pharmaceuticals*, Springer, 2018, p. 81-105.
- [55] J.-P. Kruth, P. Mercelis, J. Van Vaerenbergh, L. Froyen and M. Rombouts, "Binding mechanisms in selective laser sintering and selective laser melting," *Rapid prototyping journal*, 2005.
- [56] W. Y. Yeong, C. Y. Yap, M. Mapar and C. K. Chua, "State-of-the-art review on selective laser melting of ceramics," *High value manufacturing: advanced research in virtual and rapid prototyping*, vol. 1, p. 65-70, 2013.
- [57] M. Baumers, C. Tuck and R. Hague, "Selective heat sintering versus laser sintering: comparison of deposition rate, process energy consumption and cost performance," in *SFF proceedings*, 2015.
- [58] H. C. M. Z. L. C. Attar, "Manufacture by selective laser melting and mechanical behavior of commercially pure titanium," *Materials Science and Engineering: A*, vol. 593, pp. 170-177, 2014.
- [59] S. Bremen, W. Meiners and A. Diatlov, "Selective laser melting: A manufacturing technology for the future?," *Laser Technik Journal*, vol. 9, p. 33-38, 2012.
- [60] Attar, H., "Effect of powder particle shape on the properties of in situ Ti-TiB composite materials produced by selective laser melting," *Journal of Materials Science & Technology*, vol. 31, no. 10, pp. 1001-1005, 2015.
- [61] J. H. Tan, W. L. E. Wong and K. W. Dalgarno, "An overview of powder granulometry on feedstock and part performance in the selective laser melting process," *Additive Manufacturing*, vol. 18, p. 228-255, 2017.
- [62] D. S. B. S. A. B. H. N. & L. G. Bourell, "Influence of the particle size distribution on surface quality and mechanical properties in AM steel parts," *Rapid Prototyping Journal*, vol. 17, pp. 195-202, 2011.

- [63] A. B. Spierings, N. Herres and G. Levy, "Influence of the particle size distribution on surface quality and mechanical properties in AM steel parts," *Rapid Prototyping Journal*, 2011.
- [64] J. H. W. W. L. E. & D. K. W. Tan, "An overview of powder granulometry on feedstock and part performance in the selective laser melting process," *Additive Manufacturing*, vol. 17, pp. 228-255, 2017.
- [65] K. Kassym and A. Perveen, "Atomization processes of metal powders for 3D printing," *Materials Today: Proceedings*, vol. 26, p. 1727-1733, 2020.
- [66] M. Lackner, *Combustion synthesis: novel routes to novel materials*, Bentham Science Publishers, 2010.
- [67] P. La, M. Bai, Q. Xue and W. Liu, "A study of Ni3Al coating on carbon steel surface via the SHS casting route," *Surface and Coatings Technology*, vol. 113, p. 44-51, 1999.
- [68] A. G. Merzhanov, "The chemistry of self-propagating high-temperature synthesis," *Journal of Materials Chemistry*, vol. 14, p. 1779-1786, 2004.
- [69] ISO 13314:2011, "Mechanical testing of metals — Ductility testing — Compression test for porous and cellular metals".
- [70] K. Bodišová, M. Kašiarová, M. Domanická, M. Hnatko, Z. Lenčéš, Z. V. Nováková, J. Vojtaššák, S. Gromošová and P. Šajgalík, "Porous silicon nitride ceramics designed for bone substitute applications," *Ceramics International*, vol. 39, p. 8355-8362, 2013.

Acknowledgements

I would like to express my huge gratitude to my supervisor Professor Irina Hussainova for her great support, guidance and encouragement, and to my co-supervisor Dr Sofiya Aydinyan for her leadership, scientific and research help.

I would like to express my gratitude for Professor Jakob Kübarsepp for the thorough review and valuable suggestions on my thesis.

I would like to thank my first teachers in powder metallurgy field Dr Lauri Kollo, Dr Märt Kolnes, Dr Mart Kolnes, Dr Marek Tarraste and Dr Yaroslav Holovenko.

I would like to acknowledge the significant help from my dear friends and colleagues Dr. Roman Ivanov and Dr. Tatevik Minasyan for all useful scientific discussions, help and freindship.

I would like to thank my friends Der-Liang Yung, Marina Aghayan, Maria Drozdova, Janis Baronins, Ramin Rahmani Ahranjani, Nikhil Kumar Kamboj, Rocio Estefania Rojas Hernan, Ali Saffarshamshirgar, Rahul Kumar, Mansureh Rezapourian, and whole my group for their friendship and scientific help.

Continuing the list, I want to thank Dr Maksim Antonov, Dr Dmitri Goljandin, Dr Olga Volobujeva, Mr Rainer Traksmaa, Dr Mart Viljus, Laivi Väljaots and Hans Vallner for all the support they showed me during these 4 years of studies.

This study was supported by Tallinn University of Technology scholarship, the Estonian Research Council under grants IUT19-29 (J. Kübarsepp), PUT1063 (I. Hussainova), PRG643 (I. Hussainova), PSG220 (S. Aydinyan), M.ERA-Net. Project MOBERA18 N.20097582-CA "HOTSelfLub" and Comet-Program InTribology No.872176.

Abstract

Ti-B based composites by selective laser melting and spark plasma sintering

Titanium-boron based materials are promising because of the outstanding characteristics of high specific modulus, excellent hardness, high electrical conductivity, good wear resistance and chemical stability. Recently, titanium-boron based materials have attracted attention in high-temperature structures and wear applications, but their feedstocks preparation and consolidation are less reported.

The synthesis and consolidation methods of titanium-boron based materials were certified to be critically decisive for their properties and application. The present PhD work surveys the possibility of feedstock development and producing bulk and complex geometry Ti-B ceramic based composite materials. The particular emphasis is on the morphologies, mechanical properties, tribological properties and microstructural features affected by the technological procedure of material synthesis and consolidation of Ti-B ceramic based composites.

The powder feedstocks suitable for spark plasma sintering (SPS) and selective laser melting (SLM) were prepared via a mechanical mixing and a self-propagating high-temperature synthesis (SHS). A novel “pomegranate-like” $\text{TiB}_2\text{-Si}$ ceramic-metalloid powder feedstock with a fair flowability was successfully manufactured by SHS and subjected to SPS and SLM processes resulting in the production of the materials with 97% relative density and 7.6 GPa hardness. The TiB-Ti composites produced by SLM of the mixture of the commercially available TiB_2 and Ti powders possess a high hardness of 20.4 GPa and an indentation fracture toughness of $8.2 \text{ MPa}\cdot\text{m}^{1/2}$. The composites of $\text{TiB}_2\text{-TiB-TiN}$ have been regarded as the potential substitutes to fill and reconstruct bone cavities or areas of bone loss caused by traumas or bone disease. In-situ spark plasma sintering of Ti-TiB_w composite has enabled preparation of the material exhibiting substantially improved sliding wear performance at temperatures up to 900°C due to development of a protective lubricious boric acid tribo-layer of a high load bearing capacity. Therefore, the Ti-TiB_w compacts obtained are suitable for the self-lubrication at elevated temperatures. Furthermore, the TiB-Ti composite from SHS produced powder and consolidated via SPS demonstrated an enhanced hot sliding wear behavior.

Lühikokkuvõte

Sädepaagutus- ja selektiivse lasersulatus-tehnoloogia abil valmistatud Ti-B baasil komposiitmaterjalid

Titaani ja boori baasil materjale on palju uuritud kuna titaan-boor keraamikal on väljapaistvad omadused: kõrge erielastsusmoodul, suurepäane kõvadus, hea elektrijuhtivus ning kulumiskindlus ja keemiline stabiilsus. Viimasel ajal on palju uuritud Ti-B keraamika kasutamist rakendustes, kus materjalil peab olema kõrge temperatuuri taluvus ja kulumiskindlus. Sealjuures on vähe teadmisi, kuidas sünteesida vajalike omadustega lähtepulbreid.

Ti-B materjalide omadused ja rakendus sõltuvad otsustest, mis tehakse erinevate tootmisprotsesside juures. Käesolev doktoritöö keskendub lähtepulbrite ja konsolideerimisprotsesside arendusele, mis võimaldaks Ti-B keraamikast keerulise geomeetriaga tooteid valmistada. Fookus on sellel, kuidas materjali valmistusmeetodid mõjutavad Ti-B keraamika baasil komposiitide morfoloogiat ning mehaanilisi, triboloogilisi ja mikrostruktuuri omadusi.

Doktoritöös kasutati konsolideerimismeetoditena plasmaaktiveeritud paagutust (SPS) ja kihtlisandustehnoloogiat selektiivne lasersulatus (SLM). Lähtepulbrid valmistati mehaanilise segamise ja iselevikõrgtemperatuursünteesi (SHS) teel. Uudne "granaatõuna sarnane" TiB₂-Si keraamika-poolmetall pulber sobiva voolavusega valmistati SHS meetodil. See pulber sobis kasutamiseks toorainena nii SPS, kui ka SLM protsessides ja tulemuseks oli kõrge tihedusega (suhteline tihedus 97%) ja kõvadusega (7.6 GPa) materjal. TiB-Ti komposiit valmistati SLM meetodil kasutades pulbri tootjatelt saadud TiB₂ ja Ti pulbreid ja saadud materjali iseloomustab suur kõvadus (20.4 GPa) ja sitkus (8.2 MPa·m^{1/2}). TiB₂-TiB-TiN keraamilist komposiiti peetakse üheks võimalikuks materjaliks, mida kasutada traumade või haiguste järgselt luude vigastuste ravimisel ja luude taastamisel. Reaktiivne plasmaaktiveeritud paagutus võimaldas valmistada Ti-TiB_w komposiiti, mis toimib hästi hõõrdkulumisel temperatuuridel kuni 900°C. Selle omaduse tagab materjali pinnal moodustuv määriv boorhappe kaitsekiht, mis kaitseb materjali ennast. Ti-TiB_w komposiitidel on seega tagatud isemääriv omadus kõrgetel temperatuuridel. Lisaks on SHS meetodil valmistatud pulbri ja SPS meetodil konsolideeritud TiB-Ti komposiitidel kõrgendatud kulumiskindlus kõrgetel temperatuuridel.

List of publications not included in this thesis

- I. **Liu, L.**, Minasyan, T., Aydinyan, S., Hussainova, I. (2018). Selective laser melting of combustion synthesized titanium diboride based composites. In: EuroPM 2018 Congress and Exhibition, 14-18 October, Bilbao, Spain. European Powder Metallurgy Association, 3987459.
- II. **Liu, L.**, Minasyan, T., Aydinyan, S., Hussainova, I. (2018). Novel approach for the preparation of shapes from TiB₂-Si₃N₄ composite by selective laser melting. In: Euro PM 2018 Congress and Exhibition, 14-18 October, Bilbao, Spain. European Powder Metallurgy Association, 3987173.
- III. **Liu, L.**, Aydinyan, S., Minasyan, T., Baronins, J., Antonov, M., Kharatyan, S., Hussainova, I. (2019). Spark plasma sintering of combustion synthesized TiB₂-Si composite. *Ceramics in Modern Technologies*, 1 (Issue No 1, April).
- IV. **Liu, L.**, Minasyan, T., Aydinyan, S., Hussainova, I. (2019). The Preparation of TiC/TiN Composites by Selective Laser Melting. *Modern Materials and Manufacturing 2019. Key Engineering Materials*, vol. 799, pp. 165-170. Trans Tech Publications Ltd.
- V. **Liu, L.**, Minasyan, T., Ivanov, R., Kollo, L., Aydinyan, S., Hussainova, I. (2019). Fabrication of Copper by Selective Diode Laser Melting. In: Euro PM2019 Congress & Exhibition, 13 - 16 October 2019. Maastricht. European Powder Metallurgy Association, 4347526.
- VI. **Liu, L.**, Ivanov, R., Kumar, R., Minasyan, T., Antonov, M., Hussainova, I. (2021). Functionally Gradient Ti6Al4V-TiB Composite Produced by Spark Plasma Sintering. *Modern Materials and Manufacturing 2021. IOP Conference Series: Materials Science and Engineering*, 1140(1), 012004.
- VII. Minasyan, T., **Liu, L.**, Aydinyan, S., Kollo, L., Aghayan, M., Hussainova, I. (2018). Lattice of MoSi₂/Si₃N₄ by selective laser melting. In: EuroPM 2018 Congress and Exhibition, 14-18 October, Bilbao, Spain. European Powder Metallurgy Association, 3993050.
- VIII. Minasyan, T., **Liu, L.**, Aghayan, M., Kollo, L., Kamboj, N., Aydinyan, S., & Hussainova, I. (2018). A novel approach to fabricate Si₃N₄ by selective laser melting. *Ceramics International*, 44(12), 13689-13694.
- IX. Minasyan, T., Aghayan, M., **Liu, L.**, Aydinyan, S., Kollo, L., Hussainova, I., & Rodríguez, M. A. (2018). Combustion synthesis of MoSi₂ based composite and selective laser sintering thereof. *Journal of the European Ceramic Society*, 38(11), 3814-3821.
- X. Minasyan, T., Kirakosyan, H., Aydinyan, S., **Liu, L.**, Kharatyan, S., & Hussainova, I. (2018). Mo-Cu pseudoalloys by combustion synthesis and spark plasma sintering. *Journal of Materials Science*, 53(24), 16598-16608.
- XI. Minasyan, T., **Liu, L.**, Aghayan, M., Rodríguez, M. A., Aydinyan, S., & Hussainova, I. (2019). Mesoporous fibrous silicon nitride by catalytic nitridation of silicon. *Progress in Natural Science: Materials International*, 29(2), 190-197.
- XII. Minasyan, T., **Liu, L.**, Aydinyan, S., Antonov, M., & Hussainova, I. (2019). Selective Laser Melting of Ti/cBN Composite. *Modern Materials and Manufacturing 2019. Key Engineering Materials*, 799, 257-262. Trans Tech Publications Ltd.

- XIII. Aydinyan, S., Minasyan, T., **Liu, L.**, Cygan, S., & Hussainova, I. (2019). ZrC Based Ceramics by High Pressure High Temperature SPS Technique. *Modern Materials and Manufacturing 2019. Key Engineering Materials*, 799, 125-130. Trans Tech Publications Ltd.
- XIV. Minasyan, T., **Liu, L.**, Holovenko, Y., Aydinyan, S., & Hussainova, I. (2019). Additively manufactured mesostructured MoSi₂-Si₃N₄ ceramic lattice. *Ceramics International*, 45(8), 9926-9933.
- XV. Davtyan, D., Mnatsakanyan R., **Liu, L.**, Aydinyan, S., Hussainova, I. (2019). Microwave synthesis of B₄C nanopowder for subsequent spark plasma sintering. *Journal of Materials Research and Technology*, 8(6), 5823-5832.
- XVI. Hussainova, I., Minasyan, T., **Liu, L.**, & Aydinyan, S. (2020, April). ZrC-TiC-MoSi₂ ceramic composite by spark plasma sintering. *Journal of Physics: Conference Series*, 1527(1), 012028. IOP Publishing.
- XVII. Minasyan, T., **Liu, L.**, Aydinyan, S., Volubujeva, O., Toyserkani, E., Hussainova, I. (2020). Mo(Si_{1-x}Al_x)₂-based composite by reactive selective laser melting, *Materials Letters*, 281, 128776.
- XVIII. Auriemma, F., **Liu, L.** (2021) Acoustic performance of an additive manufactured open-cell metal foam. *IOP Conference Series: Materials Science and Engineering*, 1140(1), 012002
- XIX. Minasyan, T., **Liu, L.**; Toyserkani, E.; Hussainova, I. (2021) Isothermal oxidation of SLM fabricated Mo(Si_{1-x}Al_x)₂ based composite. *IOP Conference Series: Materials Science and Engineering*, 1140(1), 012003
- XX. Michalczewski, R., Kalbarczyk, M., Słomka, Z., Hussainova, I., **Liu, L.**, Antonov, M. (2021). Adhesion of AlCrN coating deposited on TiB₂/Ti composites sintered by SPS dedicated for high temperature tribological applications. *IOP Conference Series: Materials Science and Engineering*, 1140(1), 012010

Patents

- I. Invention: Self-functionalizing fibrous networks of Si_3N_4 with complex geometry and manufacturing thereof. Institution: Tallinn University of Technology. Authors: **Le Liu**, Tatevik Minasyan, Sofiya Aydinyan, Marina Aghayan, Irina Hussainova. Priority number: EP17174463.4. Priority date: 05.06.2017.
- II. Invention: TiB_2 based complex structures by selective laser sintering. Institution: Tallinn University of Technology. Authors: Sofiya Aydinyan, **Le Liu**, Tatevik Minasyan, Irina Hussainova. Priority number: US62/677975. Priority date: 30.05.2018.
- III. Invention: A method of direct laser shaping ceramic-intermetallic composites of MoSi_2 and/or $\text{Mo}(\text{Si},\text{Al})_2$ and Al and/or Al alloy. Institution: Tallinn University of Technology. Authors: Sofiya Aydinyan, **Le Liu**, Tatevik Minasyan, Irina Hussainova. Priority number: GB1908943.2. Priority date: 21.06.2019.

Appendix

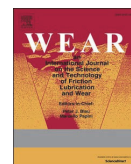
Publication I

Kumar, R., Antonov, M., **Liu, L.**, Hussainova, I. (2021). Sliding Wear Performance of in-situ Spark Plasma Sintered Ti-TiBw Composite at Temperatures up to 900°C. *Wear*, 203663.



Contents lists available at ScienceDirect

Wear

journal homepage: <http://www.elsevier.com/locate/wear>

Sliding wear performance of in-situ spark plasma sintered Ti-TiB_w composite at temperatures up to 900 °C

Rahul Kumar^a, Maksim Antonov^a, Le Liu^a, Irina Hussainova^{a,b,*}

^a Department of Mechanical & Industrial Engineering, Tallinn University of Technology, Tallinn, 19086, Estonia

^b ITMO University, Kronverkskiy 49, St, Petersburg, 197101, Russian Federation

ARTICLE INFO

Keywords:

Sliding wear
High-temperature
Ti-TiB_w composite
SPS

ABSTRACT

Although Ti-based composites find wide industrial applications, their tribological behaviour, especially at elevated and high temperatures, is not conclusively evaluated. In this work, a sliding wear performance of metal – ceramic composite of 50 wt%Ti–50 wt%TiB_w, which were in-situ produced by spark plasma sintering, was studied. Microstructural examination and X-ray diffraction analysis identified presence of two phases, Ti and TiB, and confirmed the formation of stable TiB whiskers-like grains (TiB_w) during reaction synthesis of Ti and TiB₂. Ball-on-plate dry sliding wear tests were performed against a 10 mm alumina ball under 5 N normal load with the sliding speed and distance of 0.1 ms⁻¹ and 1000 m, respectively. The tests were performed at RT and elevated temperatures of 300 °C, 500 °C, 700 °C, 800 °C and 900 °C. The worn surfaces were studied using scanning electron microscopy and 3D profilometry to understand the responsible wear mechanisms. Results have demonstrated significantly reduced wear rates of Ti-TiB_w composite as compared to reference pure Ti across all temperatures. The formation and the protective role of tribo-oxide layers on the surface of Ti-TiB_w composite during elevated temperature sliding is reported.

1. Introduction

Over the past few decades, titanium (Ti) based materials have matured at a large pace in various sectors including aviation, biomedical, chemical and structural industries due to their excellent combination of high strength, modulus and fracture toughness, biocompatibility and corrosion resistance [1]. Nevertheless, their poor wear resistance and relatively low hardness due to a low *c/a* ratio in a HCP unit cell limits their applicability in tribology related applications [2,3], especially at elevated and high temperatures (HT). Change in wear mechanism from mild to severe one, which is conditioned by the development of tribo-films, is a process of high probability during operation at the HT [4,5]. For many materials, including steels, the oxide-layers serve as protective layers against wear [6,7]. The tribo-layers developed on the surface of titanium alloys are reported to be thin, brittle, loosened and weakly adhered to a parent surface resulting in spallation during sliding [5,8,9]. Large difference in hardness between pure Ti substrate and developed surface oxides is reported to be a reason for non-adherent nature of tribo-layer [1]. Another possible reason owing to oxide delamination during room temperature (RT) sliding is a low value of Pilling-Bedworth ratio (PBR) [10], and therefore, a large lattice

mismatch between the layers. At temperatures beyond ~700 °C, a higher PBR value in Ti alloys results in scaling and oxides delamination [10,11]. However, the protective behavior of tribo-layer developed under sliding of Ti–6Al–4V and Ti–6.5Al–3.5Mo–1.5Zr–0.3Si alloys was reported in Refs. [5,8,12,13]; whereas, the formation of brittle titanium and vanadium oxides (such as TiO, TiO₂ and V₃O₄) over Ti–6Al–4V was demonstrated in Refs. [2,14]. Moreover, properties and performance of the tribo-layer are found to be highly dependent on temperature, sliding velocity and load applied [8,9,12]. Therefore, the role of surface tribo-layer during HT applications remains unclear and inconclusive for Ti-based composites.

The large number of works has been carried out to improve the wear performance of Ti-based composites exploiting a laser surface processing, coatings deposition, and reinforcements incorporation [15–20]. Most of these approaches does not result in a substantial enhancement of overall strength and hardness of materials [2,15,19]. Reinforcement with ceramic particles, such as TiN, TiC, TiB₂, TiB, B₄C, SiC and Al₂O₃, has demonstrated a great benefit in regards of improvement in mechanical as well as physical properties [1,2,17,18,21]. Titanium monoboride (TiB) is of the most widely used additive due to its excellent thermodynamic and chemical stability with Ti matrix, comparable

* Corresponding author. Department of Mechanical & Industrial Engineering, Tallinn University of Technology, Tallinn, 19086, Estonia.
E-mail address: irina.hussainova@taltech.ee (I. Hussainova).

<https://doi.org/10.1016/j.wear.2021.203663>

Received 3 September 2020; Received in revised form 3 January 2021; Accepted 6 January 2021

Available online 14 February 2021

0043-1648/© 2021 Elsevier B.V. All rights reserved.

densities of Ti and TiB, as well as a good interfacial bonding. Composites of Ti-TiB_w usually exhibit a high strength [1,3,21], low PBR and an overall biocompatibility.

Commonly, the reinforcements in metal matrix composites (MMCs) are prepared ex-situ and then added to the matrix. The other way is in-situ processing using exothermic reactions in solid-state processes or crystallization during solidification. More chemically and thermodynamically stable and homogeneous MMCs with a fine microstructure are demonstrated by the in-situ processed composites. The Gibbs free energy for the reaction between Ti and TiB₂ (i.e. Ti + TiB₂ → TiB) is of a negative value ($\Delta G \sim -154$ kJ/mol) [21,22], indicating thermodynamically instability of TiB₂ and Ti and, consequently, tendency to form TiB. Growth of needle-shaped TiB particles (whiskers-like) with a high aspect ratio (due to one dimensional growth along [010]) and well-developed interfacial bonds (due to no byproduct/intermediate phase) enhances stiffness, strength, and creep resistance of the composite [22]. In-situ formation of titanium boride whiskers (TiB_w) in titanium matrix demonstrates some benefits, such as constrained grain growth, increase in ultimate tensile strength and hardness as compared to the monolithic titanium [1,23,24]. In contrast, TiB₂ particles do not generate such a needle-like structure due to their two dimensional growth along $[1\bar{1}00]$ directions [22,23].

Several methods to fabricate titanium based bulk composites (TMCs) have come into picture in recent years including selective laser sintering [15,22], hot isostatic pressing [17,23], vacuum sintering [25], spark plasma sintering (SPS) or field-assisted sintering technique (FAST) [1, 24], etc. Very limited information is available on the microstructures and mechanical properties of the Ti-TiB_w composites fabricated by the SPS method. Unlike the conventional powder metallurgy (PM) techniques, no external heat supply is required for SPS; instead, a pulsed direct current is passed through the starting powders confined in an electrically conducting pressurized graphite die. The applied uniaxial pressure on the sample contributes to a high densification level of the products. SPS enables mixtures to be sintered at a lower temperature, as compared to the conventional PM sintering, within a relatively shorter time, which positively contribute to the dense fine-grained materials [26].

The 50 wt%Ti-50 wt%TiB_w ceramic-metal composite is an attractive candidate for a wide variety of applications not only at room temperature but also at elevated and high temperatures especially under conditions, where a good wear resistance is required. Although RT tribological performance of Ti-TiB composites have recently been extensively studied, very limited information is available on tribo-behavior of the composites at elevated temperatures. Consequently, the present paper aims at filling the existing gap and reporting on the tribological performance of the spark plasma sintered Ti-TiB_w composites identifying the role of the tribo-layer and wear associated mechanisms of materials damage. The transition from mild to severe wear is examined and variations in wear behavior at different temperatures are evaluated.

2. Experimental

2.1. Material processing

The powder mixture of Ti and TiB₂ was prepared by 2 h of mechanical rotation mixing of Ti (*Alfa Aesar*, Germany, particle size 0–50 μm) and TiB₂ (>99.5% *Alfa Aesar*, Germany, 0–44 μm) powders. The 50 wt%Ti-50 wt%TiB_w composites were fabricated by SPS (*FCT Systeme GmbH*, Germany) at temperature of 1500 °C in vacuum. The pressure of 35 MPa was applied under continuous application of electric current for a dwell time of 3 min.

The powder mixtures were loaded into a graphite mold of 25.4 mm in diameter and heated up to sintering temperature with a heating rate of 100 °C/min. The Ti-TiB_w composites are densified by means of solid

state sintering, which is a common pathway for production of high temperature ceramics and composites.

2.2. Microstructural characterization

After SPS, the sintered cylinders of 5 mm thickness and 25 mm diameter were polished to 1 μm finish using a Phoenix 4000 (*Buehler*) system and cleaned with acetone and ethylene alcohol.

Microstructural examination of the specimens was performed on mechanically polished and fractured surfaces using a scanning electron microscope (SEM, *Hitachi TM1000*) and a high-resolution scanning electron microscope (HR-SEM Zeiss Merlin) equipped with an energy dispersive spectrometer (EDS).

Phase identification was conducted by X-ray diffractometer (XRD, *Siemens Bruker D5005* X-ray analyzer with a Philips X'Pert PRO diffractometer, PANalytical, Netherlands) using Cu K α radiation (30 mA, 40 kV, $\lambda = 0.1542$ nm) in a $\theta - 2\theta^\circ$ scan with a step size of 0.02° and a count time of 0.4 s). Relative content of phases was estimated by Rietveld refinement method, which was performed by quantitative analysis of the crystalline phases detected by the corresponding XRD patterns.

2.3. Mechanical properties

The bulk density of composites was measured using Archimedes principle with a distilled water as the immersing medium using *Mettler Toledo ME204* balance with 0.1 mg accuracy. The density reported is the mean of 3 measurements.

The bulk Vickers hardness (HV30) was measured using *Indentec 5030* SKV unit with an indentation load of 30 kg for 10 s. The reported values are the mean of at least 5 indentations.

The indentation fracture toughness (IFT) was calculated from the length of radial cracks emanating from the corners of the indents following Palmqvist approach [27]. The load of 50 kgf for 10 s on the indenter resulted in quite well developed crack systems, which mitigate any surface effects of the indentation. Five equally spaced indents were recorded for each sample and values were averaged. The surface cracks initiated by the indenter were measured using optical microscopy (*Zeiss Discovery V20*) equipped with *AxioVision* software.

The surface roughness (R_a) was measured with the help of the *Mahr* perthometer, PGK 120, in contact mode.

2.4. Wear tests

A universal materials test device (UMT-2) supplied by CETR (*Bruker*) was employed for materials testing under dry circular sliding ball-on-plate configuration. Al₂O₃ Ø10 mm ball (*Redhill Precision, Czech Republic*) of HV10 \approx 1450 and $R_a = 0.02$ μm was used as a counterbody with an applied load of 5 N (0.51 kgf), sliding speed of 0.1 ms^{-1} and distance of 1000 m (duration of sliding - 10000 s) with a radius of wear track of 4.5 mm. Tests were conducted at room and elevated temperatures of 300 °C, 500 °C, 700 °C and 800 °C. As the materials may be of interest for applications at a higher than titanium phase transformation temperatures of about 883 °C, the tests were also conducted at 900 °C. The heating rate was settled to 6 °C/min. Coefficient of friction (CoF) was recorded during sliding. CpTi was used as a reference material. After the tests, the surface of the wear tracks was examined under SEM and evaluated by means of the 3D profilometer. The profiles of worn surfaces were assessed with the help of *Bruker Contour GT-K0* + 3D profilometer to determine the depth, shape and volume of material removed (net missing volume).

The performed tests take into consideration the phenomena of running-in as well as the start-stop durations during the test imitating the situation in real field bending or forming operations due to required part loading-offloading or any other process interruption and possible time delay, for example, due to human factors, etc. The running-in is

described as an initial surface and subsurface conditioning process occurring at the interface of sliding bodies during sliding test [28]. The current work is represented by a non-conformal tribo-test; the test duration is long enough to reach a steady state wear regime [28,29]. Besides, the additional step of recalibrating of device during interruptions was made to increase the test precision during testing. Therefore, the tests consist of 20 periodic restarting during a single test to assess friction evolution during each period (start, running and stop). The other parameters, such as load and frequency, were unchanged during all periods.

The fractured cross-sections were studied to evaluate the nature of the developed tribo-oxide layers. An essential step to understand the strength of the tribo-oxide layer formed at elevated temperatures, the effect of varying load at temperatures of 700, 800 and 900 °C was explored. These tests were carried out for a short time (1 min) for each load until the sufficient (more than 20%) increase in CoF or unacceptable vibration was observed. The results are reported in terms of 'load bearing capability' of the material, which includes its ability to bear a high load in addition to impart a stable and low CoF. The complex of studied properties is an important criterion for design of a tool material for forming and forging applications.

3. Results and discussion

3.1. Microstructural analysis

Fig. 1a demonstrates a uniform distribution of whiskers-like TiB particles throughout the titanium matrix and absence of spurious phases or reaction products. The XRD patterns of the composite (Fig. 1b) identifies just a few peaks of TiB₂ confirming the presence of in-situ formed TiB phase together with semi-reacted TiB₂ particles in titanium matrix containing both α (alpha) and β (beta) phases of titanium. The parent HCP alpha microstructure dissolves into the BCC structured beta phase as temperature increases beyond ≈ 883 °C (allotropic transformation in Ti), leading to a decrease in alpha phase content with an increase temperature [30]. However, due to presence of some impurities of alpha

stabilizers (such as, Al, O, C) in the starting powder of CpTi, the α phase transformation is incomplete.

3.2. Mechanical properties

The density, hardness and indentation fracture toughness values of the spark plasma sintered Ti-TiB_w composites are reported in Table 1.

SEM inspections of the fractured specimen (Fig. 1c) reveal the relatively fine TiB particles, incorporation of which increases the extent of nucleation sites providing new interfaces between Ti and TiB for grain growth inhibition during the sintering process [24].

3.3. Tribological performance

3.3.1. Wear and CoF analysis

The effect of temperature on wear rates and CoF is summarized in Figs. 2 and 3, respectively. Figs. 4 and 5 show the SEM and 3D profilometry images of the worn surface. The XRD patterns of the composites tested at 700, 800 and 900 °C are given in Fig. 6.

It was found that the wear performance of the materials tested is significantly improved with the increase in temperatures; being particularly pronounced at temperatures of 700 °C and higher. To be accurate, the wear measurements at high temperatures is greatly influenced by the oxide layer formation. At 900 °C, due to considerable oxidation of the surface, differentiation between the wear track and the pristine surface was rather difficult due to a comparable roughness.

A significant drop in CoF is indicated for composites tested at

Table 1
Density, hardness and fracture toughness of SPSeD samples.

Material	Density, g·cm ⁻³	Relative Density	Hardness, HV30	Indentation Fracture Toughness, MPa·m ^{1/2}
Ti	4.443	98.6%	287 ± 33	–
Ti-TiB _w	4.487	99.4%	1324 ± 18	10.52

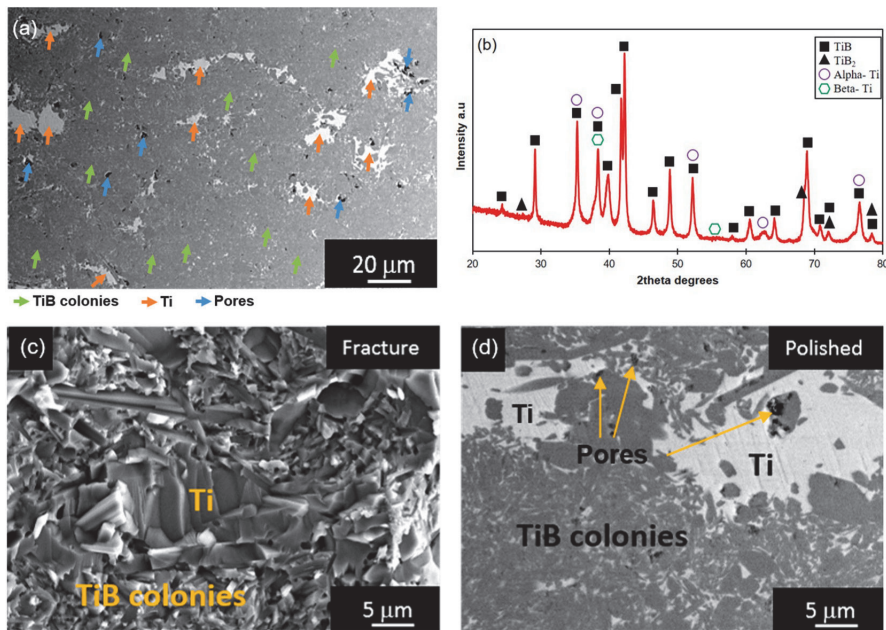


Fig. 1. Composite surface (a) SEM image; (b) XRD pattern; (c) SEM image of fractured surface; and (d) SEM image of polished surface.

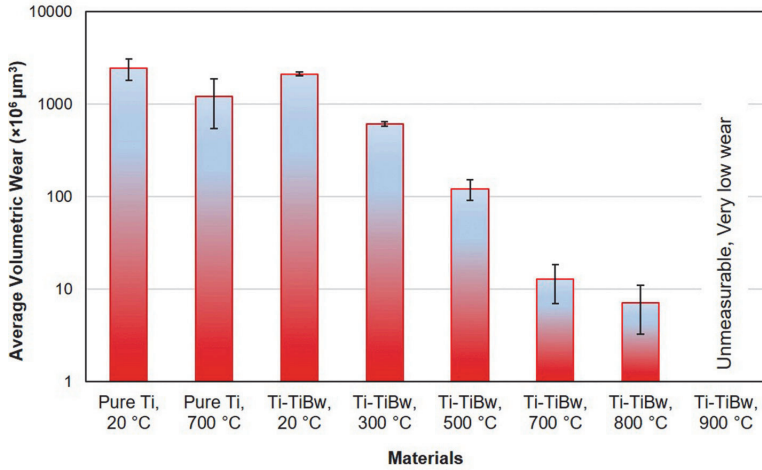


Fig. 2. The effect of temperature on wear rate of materials (logarithmic scale).

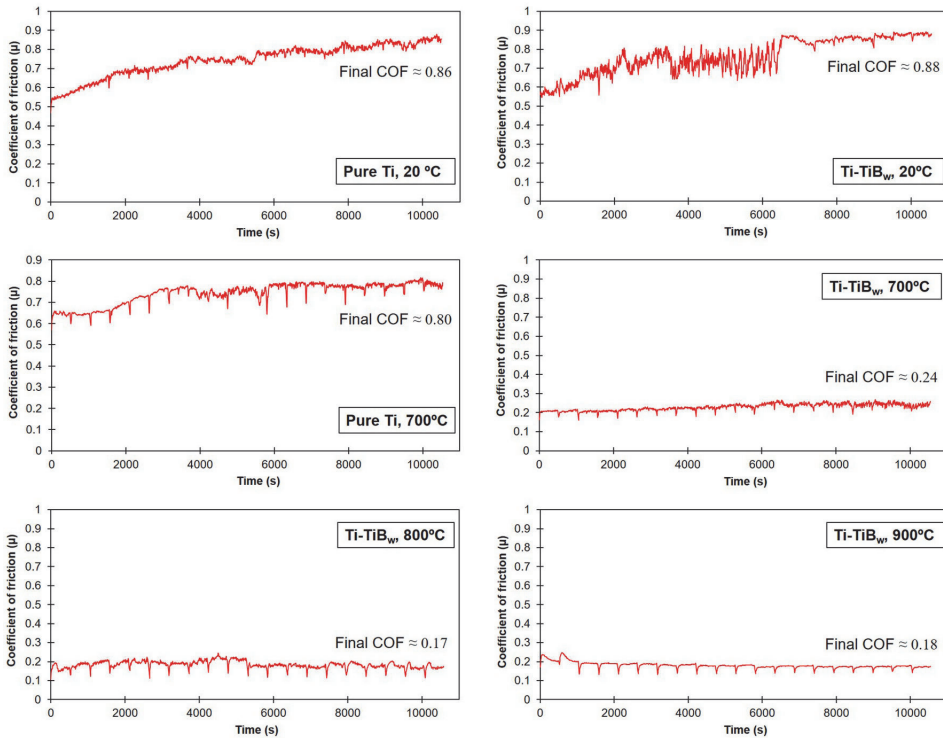


Fig. 3. Coefficient of friction of pure Ti and Ti-TiB_w composite at several test temperatures.

elevated temperatures. For the most of the cases, CoF stabilization was recorded during approximately 10 m of test run. However, at temperatures of 800 and 900 °C, the stabilization took a longer time of up to ≈50 m. High CoF in the case of pure Ti is conditioned by its lower hardness and instability of the tribo-layer [10,11,31]. Moreover, the wear debris or third bodies [32,33] accumulated during the tests might promote wear and fluctuation in CoF. Generated third bodies result in the high

localized stresses (stress concentration) and facilitate the removal of soft binder phase. However, at elevated temperatures, retained debris might be compacted and contribute to tribo-layer formation which is believed to reduce CoF. CoF fluctuation was also seen under RT composite sliding. At 300 and 500 °C, the SEM images (Fig. 4c) demonstrate a corrugation-like surface, which may be regarded as responsible for unstable CoF. The lowest friction was detected for composite tested at 800

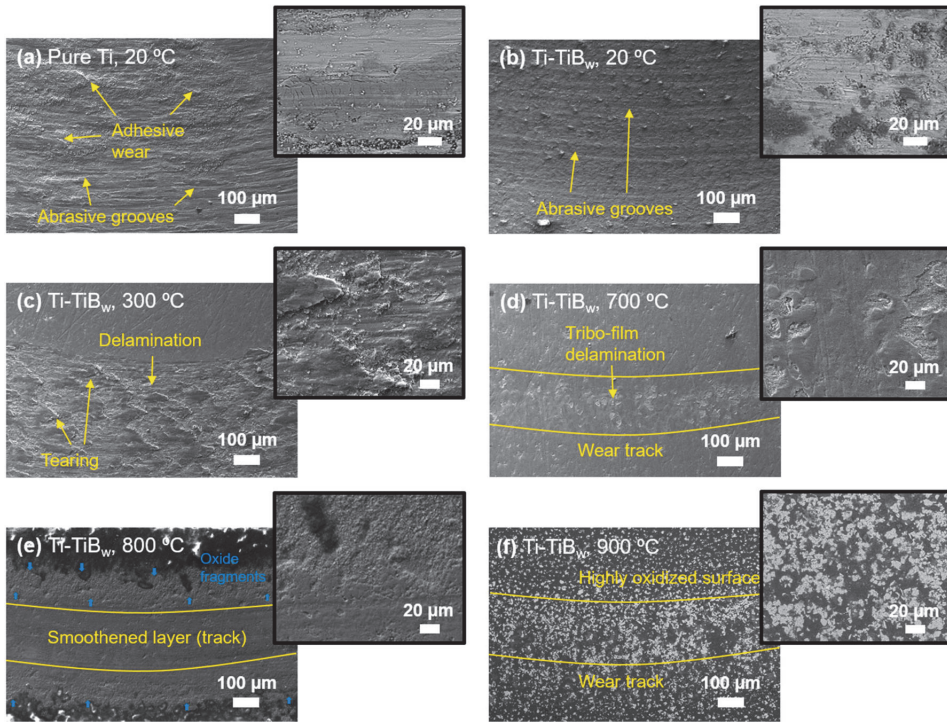


Fig. 4. SEM images of materials surface after sliding at various temperatures; (a) Pure Ti, 20 °C; (b) Ti-TiB_w, 20 °C; (c) Ti-TiB_w, 300 °C; (d) Ti-TiB_w, 700 °C; (e) Ti-TiB_w, 800 °C; and (f) Ti-TiB_w, 900 °C.

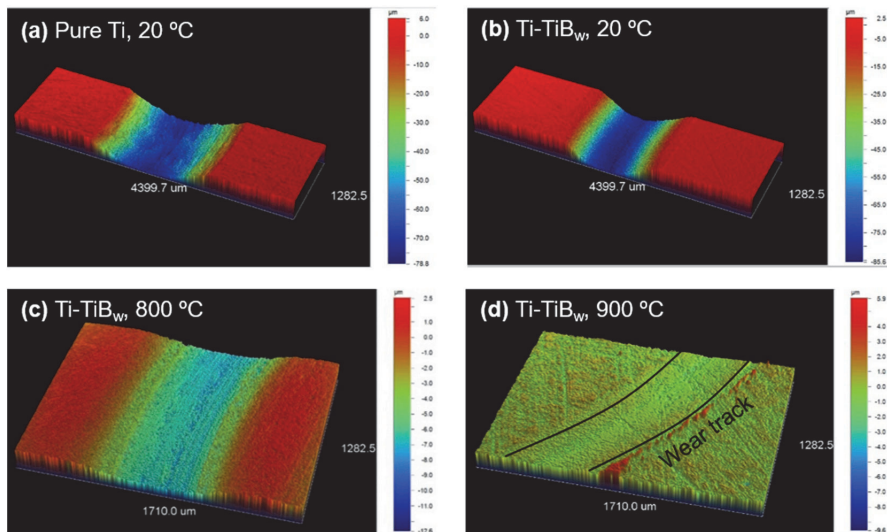


Fig. 5. 3D wear profiles of; (a) Pure Ti, 20 °C; (b) Ti-TiB_w, 20 °C; (c) Ti-TiB_w, 800 °C; and (d) Ti-TiB_w, 900 °C.

and 900 °C (i.e. CoF \approx 0.18).

Fig. 4 demonstrates the different wear mechanisms of sliding wear of pure Ti and the composites. Wear of pure Ti is associated with severe ploughing, plastic deformation and cutting resulting in significant

material removal. This increase in wear of pure Ti is amplified due to the characteristic of thermal softening (accompanied by conversion of frictional work into heat) during sliding. Abrasive wear and patches of adhesive wear mark were found on the surface of Ti specimens due to

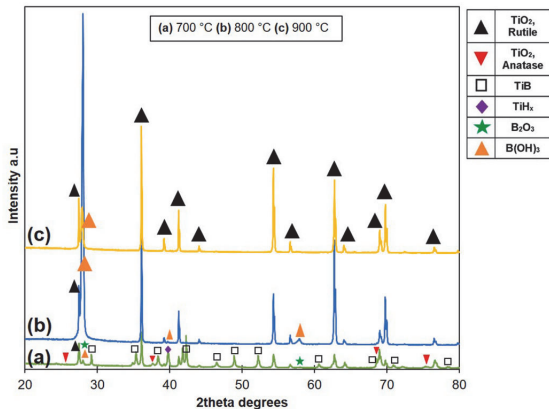


Fig. 6. XRD patterns of composite surface after test at (a) 700 °C; (b) 800 °C; and (c) 900 °C.

sliding against a much harder Al_2O_3 counterbody [31]. In addition, the wear of Ti as well as of RT tested composite is intensified by the phenomena of third body. Extreme vibration of test setup during testing of pure Ti was observed at 700 °C due to 'stick-slip' adhesive behaviour of Ti.

Normally, it is reported that a longer duration of wear test results in a high strain level at the surface, which is in contact with the counter disc, leading to the formation of surface and sub-surface cracks or fatigue-driven delamination [34]. SEM images demonstrate limited amount of delamination or local material removal along the ploughing grooves in Ti as well as the composite. The main wear mechanisms related to

Ti- TiB_w composite sliding at RT is similar to that of pure Ti except the fact that the intensity of occurring is significantly lower and is further suppressing with an increase in testing temperature. Adhesion and abrasion were dominant wear at RT composite sliding.

The XRD pattern, Fig. 6, displays the peaks of titania (TiO_2) on the surface of composite. Composite tested at 700 °C generated some peaks of TiB , which was suppressed when materials were tested at 800 and 900 °C due to intensive oxide layer development. Tribo-oxide layer delamination was evident at the lower temperatures of 300 and 500 °C tests. However, a significant diminution in tribo-layer delamination was detected at 700 °C and was almost not evident during sliding at 800 and 900 °C. The main wear mechanism at temperatures between 300-700 °C was oxidative in nature. A decrease in tribo-layer delamination from the surface during test at 700 °C and above is conditioned by the low CoF between tribo-pairs sliding and, therefore, relatively low shear stresses on the surface area. The stability and thickness of tribo-oxide layer increased with the increase in temperature of the test, which was also confirmed with cross sectional SEM imaging, Fig. 7. The principal mechanism involved into process of composite wear at 800 and 900 °C was a micro-polishing by the counterbody alumina.

The XRD patterns of the specimens tested at 700 and 800 °C, Fig. 6, reveal peaks of the compounds containing hydrogen (titanium hydride, boron oxide) owing to the precipitation of water vapour near ≈ 600 –800 °C. Water vapour release at this temperature range is reasoned by the presence of chlorine impurities, TiH_x or formation of hydrated oxides [35–37].

Anatase is often the first titanium dioxide phase to form in many processes (mainly at low temperatures) due to its lower surface energy; however, anatase tends to convert into rutile phase at elevated temperatures. The XRD patterns in Fig. 6 demonstrate a significant decrease in the peaks intensity of anatase at 800 °C and disappearance of these peaks at 900 °C. The precipitated water vapour preferably reacts with the existing metastable, less dense anatase to form the most stable,

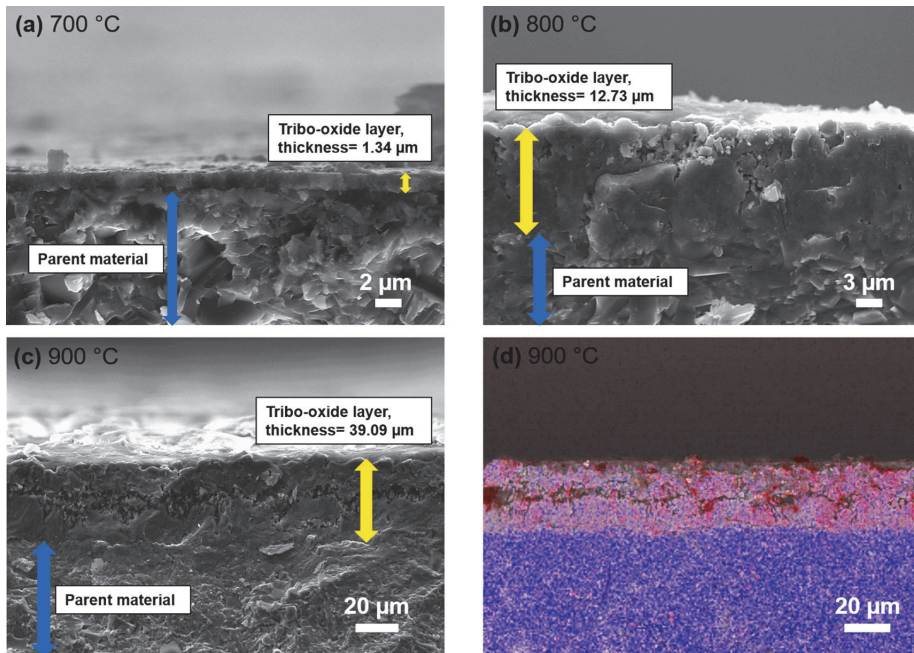


Fig. 7. SEM images of wear track cross-section of the composites tested at (a) 700 °C; (b) 800 °C; and (c) 900 °C with indication of the thickness of oxide layer formed; (d) EDS mapping of cross-section of the composite tested at 900 °C (red – oxygen; blue – titanium). (For interpretation of the references to colour in this figure legend, the reader is referred to the Web version of this article.)

dense, hard, and well-adherent rutile at elevated temperatures [38]. In addition, a decrease in the peak of hydrogen related compounds together with the increase in peaks of rutile TiO_2 was seen in XRD.

Fig. 7 demonstrates the cross-sectional examination of the composites tested at 700, 800 and 900 °C. During examination of the surface inside and outside of the wear track, it was found that the thickness of tribo-oxide layer was kept almost unchanging with no detectable alterations on the original surface. Therefore, the formation of protective tribo-layer on the surface of the composites at 700 °C and above can be stated. The thickness of oxide layer and its adherence with the parent material readily increased with the increase in test temperature from 700 to 900 °C. This situation states the role of temperature on oxidation rate by activating diffusing species. It should be noted that the accelerated oxidation rate due to increasing temperature can put the oxide layer in a more stressed condition as a result of thermal effects [39], which results in their gradual detaching from the surface as fragments. This could be the reason behind a fairly porous (or not as homogeneous as surfaces of materials tested at 700 and 800 °C) oxide layer over the composites tested at 900 °C, Fig. 7c.

The XRD patterns at Fig. 6 demonstrate the presence of lubricious boric acid, B(OH)_3 , on the composite surfaces characterized by a glazed/glassy layer (Fig. 8) at 700–900 °C. Moreover, the presence of boron oxide (B_2O_3) at 700 °C confirmed the formation of B(OH)_3 films from a spontaneous chemical reaction between water molecules and B_2O_3 coatings in a humid environment (Eqs. (1) and (2)). At 800 °C, TiB peaks get suppressed by extensive formation of TiO_2 phase, mainly rutile. The instant B_2O_3 phase was barely detected. Since TiO_2 formation is faster than B_2O_3 formation, it is possible that B_2O_3 are scarcely detected by XRD. A new peak for B(OH)_3 is detectable at 800 °C, Fig. 6b, confirming the reaction described by Eq. (2). At 900 °C, apart from strong rutile TiO_2 phase, the formed B(OH)_3 peak is still recognizable, Fig. 6c. The lubricious property of formed boric acid films is believed to contribute in lowering of CoF during tribo-pair sliding [40,41]. The formation of such self-lubricating and lubricious layer of boric acid on TiB_2 containing composites closer to ~1000 °C was also reported in Refs. [40–42]. However, a decline in its concentration at temperatures beyond 1000 °C, due to evaporation as gaseous phase is reported in Refs. [41,42]. According to the results of the current research it is possible to expect that initiation of the evaporation of in-situ formed B(OH)_3 took place already at 900 °C that resulted in its deficiency and intensification of titanium oxidation. This is confirmed by a decrease in the B(OH)_3 peak intensity at 900 °C, Fig. 6c. The highest peak intensity of boric acid and resulting glaziness was observed at 800 °C (Fig. 8b). As the temperature decreased after the test, the glazed film gradually faded away as shown in Fig. 8c. Fig. 8d shows the accumulation of liquid droplets (supposedly, boric acid) around the counterbody ball after composite sliding at 800 °C. The formation of glassy glazed layer in various metals and alloys at HT sliding and termed it to be wear protective is reported in Ref. [43]. Moreover, since the average surface roughness measured for pure Ti as well as composite specimens tested from RT to 800 °C was in the same range i.e. $R_a \sim 0.15 \pm 0.05 \mu\text{m}$, it is believed that there is no significant surface smoothing due to glazed layer formation.



3.3.2. Effect of load on coefficient of friction

The effect of applied load on coefficient of friction is illustrated in Fig. 9, wherein the CoF is plotted as a function of varying loads at test temperatures of 700, 800 and 900 °C. Dense, thick and stable (adherent) tribo-layer during the test at 800 °C resulted in the lowest and stable (at wider range of loads) CoF as compared to CoF detected at temperatures of 700 or 900 °C. Comparatively thin tribo-oxide layer developed at 700 °C resulted in unstable CoF (and increased vibration during sliding) as the load approached 14 N. The protective layer in Ti based materials usually benefit the best until 800 °C and under approaching 900–1000 °C, it tends to spall off and gradually lose its protective nature. Composite sliding under 900 °C exhibits a very fluctuating and unstable CoF with increasing loads. This was also confirmed by a high surface roughness value obtained for composite after the test at 900 °C, i.e. $R_a \sim 1.80 \pm 0.2$. An important point to note is that there was no oxide-layer breaking (or increase in CoF) during 800 °C test even at 26 N. However, during the test at 900 °C, a sudden jump in CoF at 17 N was found, which could be due to the oxide-layer breaking. Nevertheless, there could be other reasons for CoF jump, such as third body or debris particles present on the sliding track. Hereby, it can be established that the protective nature of tribo-oxide layer formed at 700 and 800 °C is the most stable and reliable, whereas the one formed at 800 °C has the highest load bearing capacity.

3.3.3. Counterbody ball wear

The ball wear (Fig. 10a) was measured using 3D profilometer and studied under SEM and analysed by EDS. No ball wear was seen for pure Ti at RT as well as 700 °C. High to average wear of alumina balls sliding against composite counterpart at RT, 300 and 500 °C was detected. Formation of patches of material removal clearly indicated the adhesion between the composite and alumina balls. At temperatures below 500 °C, the EDS mapping (RT sliding, Fig. 10c) demonstrated a significant amount of Ti transfer from the composite specimen to the alumina counterbody signifying that a severe adhesion took place between them [44,45]. However, wear is reduced with the increase in test temperature. The main mechanism responsible for wear of the ball at RT–500 °C was mainly adhesive wear (Fig. 10b).

The EDS analysis (Fig. 10c for 900 °C) shows that a worn area on the ball surface after the tests at 700, 800 and 900 °C consists of nearly zero Ti transfer from the composite surface. This is due to the well adhered tribo-layer on the tribo-surfaces mating, which is difficult to wear out. Moreover, Ti transfer was also prevented by the formation of lubricious boric acid covering the composite surface, and acting as the main sliding surface. Besides, boron transfer was evident on the balls surface (Fig. 10c). A visually smoothed/polished surface was evident on the balls at 800 and 900 °C. It is understood that transferred boron on the balls surface transformed to boric acid at 800 and 900 °C, thus

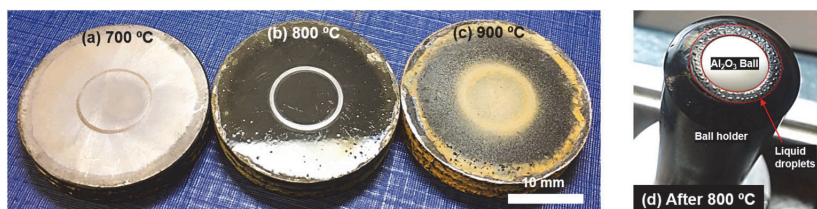


Fig. 8. Composite surfaces; (a) minimal glazed layer, 700 °C; (b) maximum glazed layer, 800 °C; (c) faded glazed layer after cooling, 900 °C; and (d) Liquid droplets staying around ball after test at 800 °C.

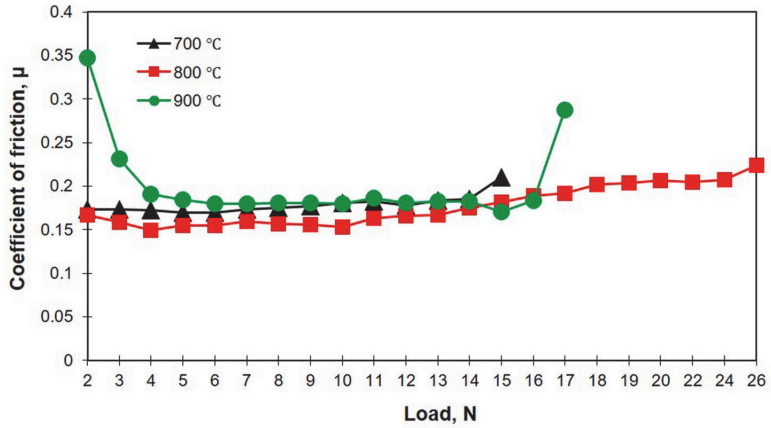
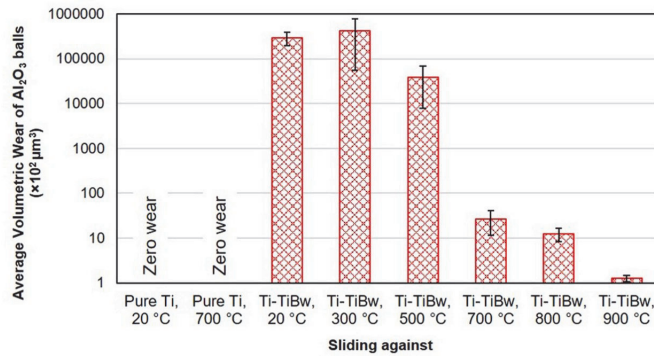
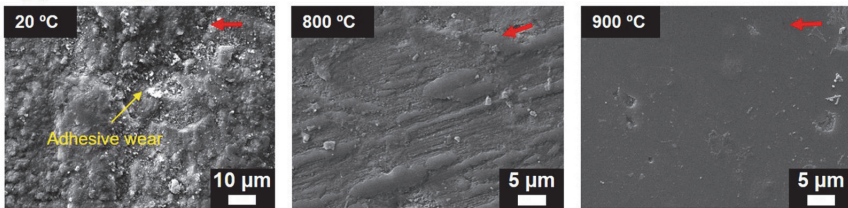


Fig. 9. Effect of increasing load and sliding temperature on CoF.

(a) Ball wear



(b) SEM images



(c) EDS analysis

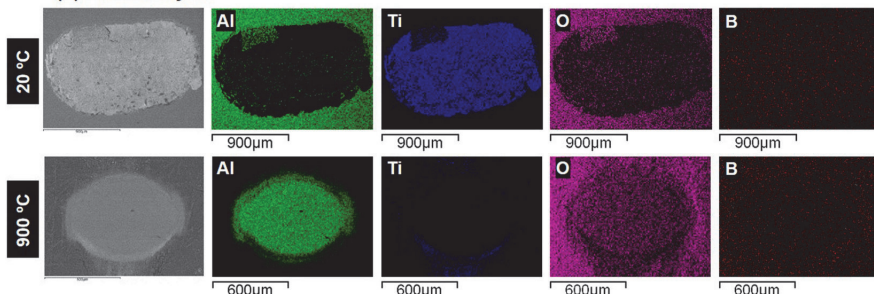


Fig. 10. (a) Ball wear; (b) SEM images of ball worn surface at 20 °C, 800 °C and 900 °C; and (c) EDS analysis of ball scars at 20 °C and 900 °C.

significantly reducing friction and wear. The main wear mechanism of alumina balls at 800 and 900 °C was mainly attributed to micro-polishing.

4. Conclusions

In the current work, a fully dense 50 wt%Ti-50 wt%TiB_w composite was in-situ produced with the help of SPS; and their tribological behavior under dry sliding conditions at temperatures up to 900 °C was evaluated. The effect of increasing temperature was demonstrated by a significant reduction in composite wear rate and lowering CoF due to development of protective tribo-layers. The formation of lubricious boric acid on the composite surface contributed into self-lubricating properties of the tribo-couple at temperatures of 700–900 °C. The highest load bearing capacity (up to 26 N) in combination with a lower CoF (<0.2) of the generated tribo-oxide layer was demonstrated at 800 °C. The wear mechanism of composite changed from adhesive and abrasive (at room temperature) to oxidative with an increase in test temperature. At temperatures of 800 and 900 °C, the micropolishing was considered as a prevailing wear mechanism.

Declaration of competing interest

The authors declare that they have no known competing financial interests or personal relationships that could have appeared to influence the work reported in this paper.

Acknowledgements

This work was supported by the Estonian Research Council grants PRG643 (I. Hussainova) and M-ERA.Net project “HOTselflub” MOBERA18.N.20097582-CA. The authors would like to thank Dr. Mart Viljus and Mr. Rainer Traksmaa for their help with SEM and XRD analysis.

References

- [1] A.S. Namini, S.A.A. Dilawary, A. Motallebzadeh, M.S. Asl, Effect of TiB₂ addition on the elevated temperature tribological behavior of spark plasma sintered Ti matrix composite, *Compos. B Eng.* 172 (2019) 271–280.
- [2] Y. Qin, L. Geng, D. Ni, Dry sliding wear behavior of extruded titanium matrix composite reinforced by in situ TiB whisker and TiC particle, *J. Mater. Sci.* 46 (14) (2011) 4980–4985.
- [3] A. Bloyce, P.H. Morton, T. Bell, Surface engineering of titanium and titanium alloys, *ASM Handbook* 5 (1994) 2232–2233.
- [4] M. Antonov, I. Hussainova, J. Kübarssepp, R. Traksmaa, Oxidation-abrasion of TiC-based cermets in SiC medium, *Wear* 273 (1) (2011) 23–31.
- [5] Y.S. Mao, L. Wang, K.M. Chen, S.Q. Wang, X.H. Cui, Tribo-layer and its role in dry sliding wear of Ti-6Al-4V alloy, *Wear* 297 (1–2) (2013) 1032–1039.
- [6] M. Antonov, R. Veinthal, E. Huttunen-Saarivirta, I. Hussainova, A. Vallikivi, M. Leljus, J. Priss, Effect of oxidation on erosive wear behaviour of boiler steels, *Tribol. Int.* 68 (2013) 35–44.
- [7] D.-L. Yung, A. Zikin, I. Hussainova, H. Danninger, E. Badish, A. Gavrilovic, Tribological performances of ZrC-Ni and TiC-Ni cermet reinforced PTA hardfacings at elevated temperatures, *Surf. Coating. Technol.* 309 (2017) 497–505.
- [8] X.X. Li, Y. Zhou, X.L. Ji, Y.X. Li, S.Q. Wang, Effects of sliding velocity on tribo-oxides and wear behavior of Ti-6Al-4V alloy, *Tribol. Int.* 91 (2015) 228–234.
- [9] Q.Y. Zhang, Y. Zhou, X.X. Li, L. Wang, X.H. Cui, S.Q. Wang, Accelerated formation of tribo-oxide layer and its effect on sliding wear of a titanium alloy, *Tribol. Lett.* 63 (1) (2016) 2.
- [10] G.K.J.M. Bertrand, K. Jarraya, J.M. Chaix, Morphology of oxide scales formed on titanium, *Oxid. Metals* 21 (1–2) (1984) 1–19.
- [11] M. Antonov, I. Hussainova, R. Veinthal, J. Pirso, Effect of temperature and loading rate on three-body abrasion of cermets and steel, *Tribol. Int.* 46 (2012) 261–268.
- [12] Q.Y. Zhang, Y. Zhou, L. Wang, X.H. Cui, S.Q. Wang, Investigation on tribo-layers and their function of a titanium alloy during dry sliding, *Tribol. Int.* 94 (2016) 541–549.
- [13] N. Dalili, A. Edrisky, K. Farokhzadeh, J. Li, J. Lo, A.R. Riahi, Improving the wear resistance of Ti-6Al-4V/TiC composites through thermal oxidation (TO), *Wear* 269 (7–8) (2010) 590–601.
- [14] Y. Qin, W. Lu, J. Qin, D. Zhang, Oxidation behavior of in situ synthesized TiB/Ti composite in air environment, *Mater. Trans.* 45 (12) (2004) 3241–3246.
- [15] M. Antonov, I. Hussainova, Experimental setup for testing and mapping of high temperature abrasion and oxidation synergy, *Wear* 267 (2009) 1798–1803.
- [16] E. Atar, E.S. Kayali, H. Cimenoglu, Characteristics and wear performance of borided Ti6Al4V alloy, *Surf. Coating. Technol.* 202 (19) (2008) 4583–4590.
- [17] Y. Pu, B. Guo, J. Zhou, S. Zhang, H. Zhou, J. Chen, Microstructure and tribological properties of in situ synthesized TiC, TiN, and SiC reinforced Ti3Al intermetallic matrix composite coatings on pure Ti by laser cladding, *Appl. Surf. Sci.* 255 (5) (2008) 2697–2703.
- [18] S. Zhang, W.T. Wu, M.C. Wang, H.C. Man, In-situ synthesis and wear performance of TiC particle reinforced composite coating on alloy Ti6Al4V, *Surf. Coating. Technol.* 138 (1) (2001) 95–100.
- [19] R. Kumar, M. Antonov, Self-lubricating materials for extreme temperature tribo-applications, *Mater. Today: Proc.* (2020), <https://doi.org/10.1016/j.matpr.2020.10.824>.
- [20] Y. Holovenko, M. Antonov, L. Kollo, I. Hussainova, Friction studies of metal surfaces with various 3D printed patterns tested in dry sliding conditions, Part J: *J. Eng. Tribol.* 232 (1) (2018) 43–53.
- [21] K. Morsi, V.V. Patel, S. Naraghi, J.E. Garay, Processing of titanium-titanium boride dual matrix composites, *J. Mater. Process. Technol.* 196 (1–3) (2008) 236–242.
- [22] L. Liu, T. Minasyan, R. Ivanov, S. Aydinian, I. Hussainova, Selective laser melting of TiB₂-Ti composite with high content of ceramic phase, *Ceram. Int.* 46 (13) (2020) 21128–21135.
- [23] H. Singh, M. Hayat, H. Zhang, R. Das, P. Cao, Effect of TiB₂ content on microstructure and properties of in situ Ti-TiB composites, *Int. J. Miner., Metall. Mater.* 26 (7) (2019) 915–924.
- [24] A.S. Namini, M. Azadbeh, M.S. Asl, Effect of TiB₂ content on the characteristics of spark plasma sintered Ti-TiBw composites, *Adv. Powder Technol.* 28 (6) (2017) 1564–1572.
- [25] M.S. Kumar, P. Chandrasekar, P. Chandramohan, M. Mohanraj, Characterisation of titanium-titanium boride composites processed by powder metallurgy techniques, *Mater. Char.* 73 (2012) 43–51.
- [26] I. Hussainova, M. Antonov, N. Voltshihin, J. Kübarssepp, Wear behavior of Co-free hardmetals doped with zirconia and produced by conventional PM and SPS routines, *Wear* 312 (1–2) (2014) 83–90.
- [27] F. Sergejev, M. Antonov, Comparative study on indentation fracture toughness measurements of cemented carbides, *Proc. Estonian Acad. Sci. Eng.* 12 (4) (2006) 388–398.
- [28] J. Baronins, M. Antonov, S. Bereznev, T. Raadik, I. Hussainova, Raman spectroscopy for reliability assessment of multilayered AlCrN coating in tribo-corrosive conditions, *Coatings* 8 (7) (2018) 229.
- [29] P.J. Blau, Running-in: art or engineering? *J. Mater. Eng.* 13 (1) (1991) 47–53.
- [30] M. Villa, J.W. Brooks, R.P. Turner, H. Wang, F. Boitout, R.M. Ward, Microstructural modeling of the α - β phase in Ti-6Al-4V: a diffusion-based approach, *Metall. Mater. Trans. B* 50 (6) (2019) 2898–2911.
- [31] D.S.R. Krishna, Y.L. Brama, Y. Sun, Thick rutile layer on titanium for tribological applications, *Tribol. Int.* 40 (2) (2007) 329–334.
- [32] Q. Yang, T. Senda, N. Kotani, A. Hirose, Sliding wear behavior and tribofilm formation of ceramics at high temperatures, *Surf. Coating. Technol.* 184 (2–3) (2004) 270–277.
- [33] R. Kumar, M. Antonov, U. Beste, D. Goljandin, Assessment of 3D printed steels and composites intended for wear applications in abrasive, dry or slurry erosive conditions, *Int. J. Refract. Metals Hard Mater.* 86 (2020) 105126.
- [34] N.P. Suh, The delamination theory of wear, *Wear* 25 (1) (1973) 111–124.
- [35] M. Yan, H.P. Tang, M. Qian, Scavenging of oxygen and chlorine from powder metallurgy (PM) titanium and titanium alloys, in: *Titanium Powder Metallurgy*, Butterworth-Heinemann, 2015, pp. 253–276.
- [36] S. Malinow, W. Sha, Z. Guo, C.C. Tang, A.E. Long, Synchrotron X-ray diffraction study of the phase transformations in titanium alloys, *Mater. Char.* 48 (4) (2002) 279–295.
- [37] W. Feng, Q. Wang, Q. Kong, X. Zhu, J. Wu, C. Sun, Influence of high-temperature water vapor on titanium film surface, *Oxid. Metals* 86 (3–4) (2016) 179–192.
- [38] D.A. Hanaor, C.C. Sorrell, Review of the anatase to rutile phase transformation, *J. Mater. Sci.* 46 (4) (2011) 855–874.
- [39] C. Coddet, A.M. Craze, G. Beranger, Measurements of the adhesion of thermal oxide films: application to the oxidation of titanium, *J. Mater. Sci.* 22 (8) (1987) 2969–2974.
- [40] Y.H. Koh, S.Y. Lee, H.E. Kim, Oxidation behavior of titanium boride at elevated temperatures, *J. Am. Ceram. Soc.* 84 (1) (2001) 239–241.
- [41] A. Erdemir, G.R. Fenske, R.A. Erck, A study of the formation and self-lubrication mechanisms of boric acid films on boric oxide coatings, *Surf. Coating. Technol.* 43 (1990) 588–596.
- [42] C. Higdon, B. Cook, J. Harringa, A. Russell, J. Goldsmith, J. Qu, P. Blau, Friction and wear mechanisms in AlMgB₁₄-TiB₂ nanocoatings, *Wear* 271 (9–10) (2011) 2111–2115.
- [43] A. Pauschitz, M. Roy, F. Franek, Mechanisms of sliding wear of metals and alloys at elevated temperatures, *Tribol. Int.* 41 (7) (2008) 584–602.
- [44] M. Antonov, H. Afshari, J. Baronins, A. Adoberg, T. Raadik, I. Hussainova, The effect of temperature and sliding speed on friction and wear of Si₃N₄, Al₂O₃, and ZrO₂ balls tested against AlCrN PVD coating, *Tribol. Int.* 118 (2018) 500–514.
- [45] Der-Liang Yung, Maksim Antonov, Renno Veinthal, Irina Hussainova, Wear behaviour of doped WC-Ni based hardmetals tested by four methods, *Wear* 352–353 (2016) 171–179.

Publication II

Kumar, R., **Liu, L.**, Antonov, M., Ivanov, R., Hussainova, I. (2021). Hot sliding wear of 88wt% TiB-Ti composite from SHS produced powders. *Materials*, 14(5), 1242.

Article

Hot Sliding Wear of 88wt% TiB–Ti Composite from SHS Produced Powders

Rahul Kumar ¹, Le Liu ¹, Maksim Antonov ¹, Roman Ivanov ¹ and Irina Hussainova ^{1,*}

¹ Department of Mechanical & Industrial Engineering, Tallinn University of Technology, 19086 Tallinn, Estonia; rahul.kumar@taltech.ee (R.K.); le.liu@taltech.ee (L.L.); maksim.antonov@taltech.ee (M.A.); roman.ivanov@taltech.ee (R.I.)

* Correspondence: irina.hussainova@taltech.ee

Abstract: Titanium alloys and composites are of great interest for a wide variety of industrial applications; however, most of them suffer from poor tribological performance, especially at elevated temperatures. In this study, spark plasma sintering was utilized to produce a fully dense and thermodynamically stable TiB–Ti composite with a high content of ceramic phase (88 wt.%) from self-propagating high temperature synthesized (SHS) powders of commercially available Ti and B. Microstructural examination, thermodynamic assessments, and XRD analysis revealed the in situ formation of titanium borides with a relatively broad grain size distribution and elongated shapes of different aspect ratio. The composite exhibits a considerable hardness of 1550 HV30 combined with a good indentation fracture toughness of 8.2 MPa·m^{1/2}. Dry sliding wear tests were performed at room and elevated temperature (800 °C) under 5 and 20 N sliding loads with the sliding speed of 0.1 m·s⁻¹ and the sliding distance of 1000 m. A considerable decline in the coefficient of friction and wear rate was demonstrated at elevated temperature sliding. Apart from the protective nature of generated tribo-oxide layer, the development of lubricious boric acid on the surface of the composite was wholly responsible for this phenomenon. A high load bearing capacity of tribo-layer was demonstrated at 800 °C test.

Citation: Kumar, R.; Liu, L.; Antonov, M.; Ivanov, R.; Hussainova, I. Hot Sliding Wear of 88wt% TiB–Ti Composite from SHS Produced Powders. *Materials* **2021**, *14*, 1242. <https://doi.org/10.3390/ma14051242>

Academic Editor: Tomasz Czujko

Received: 17 February 2021

Accepted: 1 March 2021

Published: 5 March 2021

Publisher's Note: MDPI stays neutral with regard to jurisdictional claims in published maps and institutional affiliations.



Copyright: © 2021 by the authors. Licensee MDPI, Basel, Switzerland. This article is an open access article distributed under the terms and conditions of the Creative Commons Attribution (CC BY) license (<http://creativecommons.org/licenses/by/4.0/>).

Keywords: sliding wear; TiB-based composite; high temperature; SHS; SPS

1. Introduction

Growing demand for titanium (Ti) and titanium alloys for a wide variety of industrial applications including, but not limited to, aerospace, marine, automotive, and biomedical industries have made Ti-based materials highly important. An extensive use of titanium alloys has been connected to their high strength-to-weight ratio, toughness, and extraordinary corrosion resistance. However, insufficient tribological performance of many alloys has hindered even wider applications of titanium, its alloys, and Ti-based composites [1,2], especially at elevated temperatures. To fill the gap and overcome the associated limitations, several methods including surface modifications [3], hard and soft coatings deposition [4], incorporating self-lubricating mediums [5], and reinforcements inclusion [6] are continuously reported. Titanium monoboride (TiB) is one of the most used additives for Ti matrix to yield improvement in mechanical as well as tribological properties due to Ti and TiB thermodynamic and chemical stability, similar density (4.5 g/cm³ for Ti and 4.56 g/cm³ for TiB), close values of coefficient of thermal expansion (8.2 × 10⁻⁶ °C⁻¹ for Ti and 6.2 × 10⁻⁶ °C⁻¹ for TiB), ability to retain protective tribo-oxide layer formed at elevated temperatures, and no spurious interfacial phase formation [1,7]. In situ formation of TiB during the reaction between Ti and TiB₂ has drawn considerable interest and is widely studied [3,8]. The Gibbs free energy for the reaction (i.e., Ti + TiB₂ → 2TiB) is a negative one (ΔG ~ -154 kJ/mol) demonstrating thermodynamical instability of TiB₂ and Ti and, therefore, a high potential to form a more stable TiB [8]. At elevated temperatures

and oxidative environment, Ti–TiB composites are suspected for the development of a dense rutile dominated oxides with a strong interfacial cohesion over the composites preventing the materials from severe oxidation and brittle fracture of sub-surface tribo-layers [9].

Changes in surface reactivity at elevated temperatures is a common attribute in metals. A large number of applications depends upon the ability of contacting surfaces to self-lubricate and/or to form protective oxide layers as a result of reactions with environments or during the tribo-contact [2]. Unlike steels and few others, oxides of Ti and its alloys are termed to be unprotective and undergo easy spallation during tribo-cycles [10,11]. Large lattice mismatch between the developed oxides and pristine Ti (or alloy) and ineffective Pilling–Bedworth ratio (P-B ratio) are the reason for such behavior [12]. Oxide scales developed over Ti and Ti–6Al–4V are reported to experience scaling, delamination, and constant fragmentation of brittle TiO, TiO₂, and V₂O₅ [12,13], especially at temperatures above ~700 °C. Sliding wear tests accomplished on Ti–6Al–4V alloy under 10–50 N load at a room temperature were carried out with the integration of TiO₂, Fe₂O₃, or mixtures of nano-scaled oxides onto sliding pathways, and the wear-increasing function was credited to TiO₂ with a low load-carrying capability [11]. On the other hand, in [14], a thermal oxidation treatment of Ti6Al4V-10 vol.%TiC composites at a temperature of 600–800 °C was performed, revealing the development of a uniform oxide layer of rutile. Besides, a higher load carrying capacity of thermally oxidized composites was reported after a sliding test with 10 N of a load. Similarly, in [15], the development of a dense rutile dominated layer with a strong interfacial cohesion over Ti-8 vol.% TiB composites at 650 °C was demonstrated. The performance of the tribo-oxide layer was found to be greatly influenced by temperature, sliding velocity, and the load applied. In general, the lack of clarity regarding the properties and the elevated temperature wear performance of Ti–TiB composites in conditions of dry sliding has motivated this study.

Energy and time efficient spark plasma sintering (SPS) is one of the successfully used processing techniques to produce dense Ti-matrix composites with minimal porosity and tremendous improvements in mechanical as well as tribological properties [1]. It is a well-established fact that the successful performance of composite materials at service requiring movement of one part over another is attainable with the help of careful selection of constituents, manufacturing technology, and post-treatment. The method of the precursor powders preparation and developed microstructure are shown to be the main features for the Ti–TiB cermet as the composite for tribological applications.

Most of the time, the composites are consolidated using commercially available and conventionally mixed/milled precursor powders of Ti and TiB₂, which often result in inhomogeneous structures with whisker-like TiB grains. To minimize these drawbacks, our approach proposes utilization of self-propagating high-temperature synthesis (SHS) or combustion synthesis for fabrication of the powder feedstock representing a collection of “pomegranate-like” particles consisting of TiB particulates bonded/clued by titanium. SHS has been widely accepted for production of various materials including ceramics, composites, and intermetallic and nano-phase materials [16,17] due to its high efficiency, negligible energy consumption, short processing time, and high productivity. It utilizes the advantages of extreme heat generated by the exothermic reaction in a reactive mixture during processing, resulting in the formation of a needed solid product [6]. Besides, SHS represents an in situ processing for the preparation of composite materials with interpenetrating phases of tailored composition.

As the formation of glazed layers of compacted oxides can provide wear protection to the composites at elevated temperatures [18,19], the current research work reports on the development of a tribo-layer during the sliding wear of spark plasma sintered Ti–TiB cermet of only 12 wt.% metal content, which were fabricated from the SHS produced “pomegranate-like” powders of Ti and TiB. Wear of the composite has been studied at the conditions of dry sliding at room (20 °C) and elevated (800 °C) temperatures. The

responsible wear mechanisms have been evaluated, and the role of surface layer formation during elevated temperature sliding has been discussed.

2. Materials and Methods

2.1. Self-Propagating High-Temperature Synthesis

The commercially available pure boron, B (purity >95%, Sigma-Aldrich, Taufkirchen, Germany, particle size <1 μm), and Ti (purity >99.5%, Alfa Aesar, Karlsruhe, Germany, particle size <44 μm) were prepared as 15 and 85 wt.% powder mixture, Figure 1a, for the combustion synthesis of the precursor suitable for SLM processing. The composition was designed to produce 85 wt.% of TiB with 15 wt.% of Ti upon a complete reaction $x\text{Ti}+y\text{B}\rightarrow y\text{TiB}+(x-y)\text{Ti}$. A mixture of reactants was homogenized in a ceramic mortar for 15 min and filled in a steel boat to prepare the rectangular green bodies of 10 mm length, 20 mm width, 15–20 mm height, and 50 grams' weight. The samples were placed into a reaction chamber CPR-3.5l filled with argon gas of 99.999% purity and subjected to the pressure of 0.3 MPa. To initiate the combustion reaction, a 7 sec annealing of a tungsten coil positioned on the bottom side of samples was employed under 12 V. The mixture of KNO_3 and Si powders with the weight ratio 1:4 was used as ignition agents. Two C-type tungsten-rhenium thermocouples (wire diameter 0.1 mm) preliminarily covered with a thin layer of boron nitride were positioned at holes drilled in the green body to record temperature-time profiles of the combustion process. Subsequently, the SHSed samples were crashed by a roller, then treated by disintegrator milling to make fine "pomegranate-like" powders, as detailed in [8]. The "pomegranate-like" powder represents the collection of composite particles with a relatively low size distribution and of the same flowability. Ceramic particles have been already embedded into the metallic titanium, which make the process of sintering much easier and more reliable.

The maximum combustion temperature (T_c) of 1700 $^\circ\text{C}$ was recorded. The computed average value of combustion velocity (U_c) is 2.12 mm/sec. The standard error of measurement for T_c and U_c were ± 20 $^\circ\text{C}$ and 5%, respectively. The evolution of temperature (T_c) and pressure during synthesis is demonstrated in Figure 1b.

2.2. Spark Plasma Sintering

Prior to SPS processing, the powder blends were milled in a semi-industrial milling system DSL-115 disintegrator (TalTech, Tallinn, Estonia). The SHS synthesized Ti-B powdered product was consolidated using SPS (FCT Systeme GmbH, Frankenblick, Germany) at a temperature of 1200 $^\circ\text{C}$ with application of 50 MPa pressure and continuous direct electric current during 3 min in a vacuum. The mixture was loaded into a graphite mold (diameter—25.4 mm) and heated up (heating rate—100 $^\circ\text{C}/\text{min}$) to the temperature of processing.

2.3. Materials Characterization

The produced cylinders with a thickness of 5 mm were refined to 1 μm finish with a Phoenix 4000 (Buehler) with the help of 8 inch diamond grinding discs (DGD Terra, Buehler, Esslingen, Germany). The polishing was executed with a speed of 300 rev/m during 3 min for each disc. The discs were changed in a sequence (74 μm , 40 μm , 20 μm , 10 μm , 3 μm , 1 μm) and water was used as a polishing medium. Then the polished specimens were cleaned by acetone and ethylene alcohol.

Microstructural inspection of the composites was made on polished and fractured surfaces using a high-resolution scanning electron microscope, SEM (HR-SEM Zeiss Merlin, Oberkochen, Germany) equipped with an energy dispersive spectrometer (EDS). The particle size distribution was assessed with the help of a laser diffraction using Malvern Mastersizer 3000, Almelo, Netherlands.

The chemical compositions of the powder mixture and the bulk samples were analyzed with the help of X-ray diffractometer (XRD, Siemens Bruker D5005 X-ray

analyzer with a Philips X'Pert PRO diffractometer, PANalytical, Almelo, Netherlands) using Cu K α radiation ($\lambda = 0.1542$ nm, 30 mA, 40 kV) with a scan step size of 0.02° and a count time of 0.4 s at each step. Relative fraction of the presented phases was estimated with the help of the Rietveld refinement method, which was performed by quantitative analysis of the crystalline phases detected by the corresponding XRD pattern.

The bulk density of composites was measured by means of the Archimedes' principle (Mettler Toledo ME204 balance, Greifensee, Switzerland) with 0.1 mg accuracy and distilled water as the immersing environment. The reported density is an average of at least 3 measurements. The relative density calculations are based on the assumption of presence of phases detected by XRD and their volume fraction.

The bulk Vickers hardness (HV30) was estimated using a tester (Indentec 5030 SKV, Stourbridge, West Midlands, UK) at the indentation load of 30 kg applied for 10 s. The reported values are the mean of at least 5 indentations.

The indentation fracture toughness (IFT) was calculated from the length of radial cracks emanating from the corners of the indents following the Palmqvist approach [20]. The load of 50 kg \cdot f on the indenter resulted in the quite well-developed crack systems, which mitigate any surface effects of the indentation. The length of the cracks initiated on the sample' surface by the indent were recorded by optical microscopy (Zeiss Discovery V20, Oberkochen, Germany) equipped with AxioVision 4.8.2 software. For each sample, values of 5 recorded indents were averaged.

2.4. Sliding Wear Test

A universal tribo-test device CETR/Bruker—UMT-2 was employed for materials testing under dry unidirectional sliding in ball-on-plate configuration. The ball counterbody of Al₂O₃ with $\varnothing 10$ mm (Redhill Precision, Prague, Czech Republic), hardness HV10 \approx 1450, and surface roughness R_a = 0.02 μ m was exploited under an applied load of 5 N (0.51 kgf) and 20 N (2.04 kgf), sliding speed of 0.1 m \cdot s⁻¹, and distance of 1000 m with the radius of a wear track of 4.5 mm. Each test consists of 20 equal periods with a duration of 500 s to assess friction progress during each test (start, running, and stop). An additional recalibration of device between periods was implemented to increase the test precision. This is especially important for the tests performed at elevated temperatures due to possible effect of a heat from a test chamber on the performance of force sensors positioned above it. The other parameters (load and frequency) were kept unchanged during the whole period. The duration of the test was selected to be sufficient to reach a steady state wear regime and to provide a measurable wear [21,22]. Surfaces of disk and ball were cleaned with ethanol, acetone, and then dried prior each test. Tests were conducted both at room and elevated temperature of 800 $^\circ$ C. The heating rate of 6 $^\circ$ C/min was settled to avoid unwanted thermal shock to test materials and equipment. The developed wear tracks were examined by SEM and evaluated by 3D profilometer Bruker Contour GT-K0+ to control the net missing volume.

The cross-section of the materials tested at 800 $^\circ$ C and both sliding loads of 5 and 20 N were examined with the help of SEM (HR-SEM Zeiss Merlin, Oberkochen, Germany) to explore the nature of the developed tribo-oxide layers.

In addition, oxidation tests were conducted in a laboratory furnace (Nabertherm muffle furnace, Lilienthal, Germany) at 300, 500, 700, and 800 $^\circ$ C to evaluate the oxide layer development. The oxidation duration was kept similar to the sliding test duration (10000 s). The oxidized samples were checked for weight gain to the nearest 0.1 mg using a Mettler Toledo ME204 and surface Vickers microhardness (HV0.5) using a tester unit (Indentec 5030 SKV, Stourbridge, West Midlands, UK) applying 500 g (0.5 kg) load for a dwell time of 10 s. The load of indentation was selected to provide precise imprint diagonal measurement and to reduce the influence of the underneath material. The values reported are averaged for at least 5 indentations/measurements made.

3. Results and Discussion

3.1. Microstructural Analysis

Figure 1a,b show SEM images of the initial powder mixtures and the combustion thermogram and pressure during SHS.

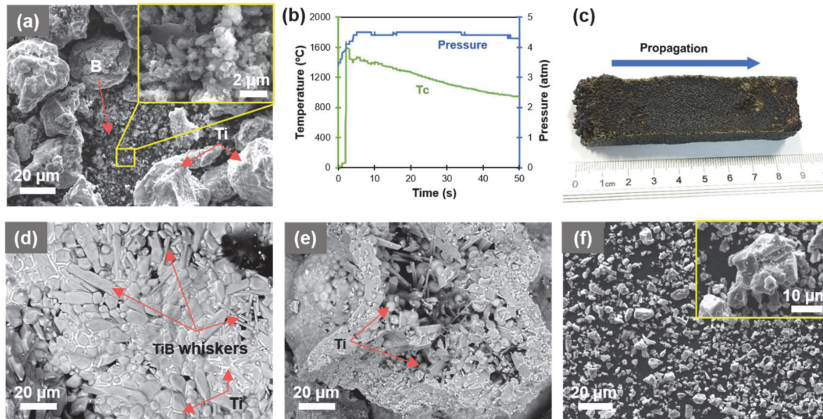


Figure 1. (a) SEM image of initial Ti and B powder mixture; (b) combustion temperature and pressure evolution; (c) high temperature synthesized (SHS) bulk product; (d,e) typical examples of SHSed fragments after manual crushing; and (f) composite powder after disintegrator milling.

According to the curve of temperature evolution during the combustion process, the temperature of 1700 °C is sufficient to melt Ti and dissolve or interact with B (according to phase diagram presented in [7]) to form TiB as per the principle of reaction diffusion. Additionally, an excess of Ti in the system serves as a matrix phase in a composite powder. It is to be noted that the high temperature during synthesis will not retain for a long time and a rapid drop in the temperature of the part below melting point of Ti (~1650 °C) is demonstrated (Figure 1b). A concurrent decrease in combustion temperature and an increase in pressure (due to sudden gas expanding from reaction frontier) creates the kinetic conditions which favored the formation of spherically shaped Ti droplets/particles.

The SEM images of a crashed SHS product in Figure 1d, e demonstrate the co-existing agglomerates of fine and coarse particles of either rounded or needle-like morphology together with spherical molten Ti droplets, as Ti was given with an excess amount to the initial mixture. The TiB whiskers mostly grow towards the center of the piece of material after SHS processing, which can be explained by the fact that elemental boron tends to be present in the center of segregation on subsequent precipitation from molten solution of Ti and B.

Figure 1f shows the SEM image of Ti–TiB composite powder after disintegrator milling. Particle size distribution (PSD) specified in Table 1 reveals the median diameter (D50) of Ti–TiB powder of around 10 µm.

Table 1. Size distributions of the SHSed Ti–TiB powders.

Particle Size (Ti–TiB SHSed Powder)		
D10 (µm)	D50 (µm)	D90 (µm)
2.12 µm	8.98 µm	27.2 µm

The XRD patterns of SHSed Ti–TiB powder confirm the presence of TiB, TiB₂, and free Ti as per Equation (1), which describes the first step of composite development, Figure 2. The presence of TiB₂ phase together with Ti and TiB was also reported in [23,24], mainly due to either the inhomogeneity of B in the mixture powder or the insufficient time for completion of the reaction between TiB₂ and Ti. The approximate concentration of 17.4% free Ti, 66.4% TiB, and 16.2% TiB₂ was evaluated through the analysis of the XRD pattern of the SHSed powder, Figure 1f.

However, upon SPS, no evident TiB₂ is identified by the XRD of the composite bulk as duration of the process allows complete chemical reaction between TiB₂ and Ti as per Equation (2), which describes the second step of composite fabrication (SPS) resulting in complete reaction between available TiB₂ and free Ti; therefore, the stable TiB phase and monoclinic α -Ti are the main constituents of the composite. The XRD pattern of SPSeD bulk recorded from the polished surface confirms the concentration of TiB phase of ~87.8% and Ti phase of ~12.2% with neither TiB₂ nor other phases.

Figure 2a demonstrates the SEM image of the composite revealing rather homogeneous distribution of TiB phase (grey) throughout the monoclinic Ti (white).

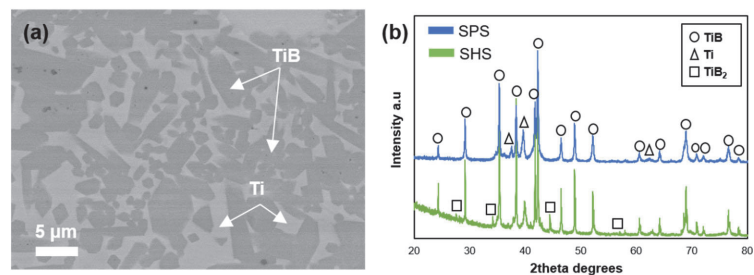
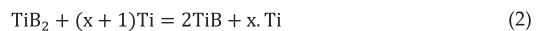


Figure 2. (a) SEM image of SPSeD (spark plasma sintering) composite; and (b) XRD patterns of SHSed powder and SPSeD composite.

The TiB–Ti composite produced by SPS from the conventionally milled/mixed commercially available powders of Ti and TiB₂ are detailed in [19]. Fabrication of the fully dense composites with a high hardness of ~1324 HV₃₀ and an indentation fracture toughness of 10.5 MPa·m^{1/2} has been reported. The homogeneous distribution of needle-like colonies of fine TiB was shown to be a key feature of the microstructure. The composites produced out from SHSed “pomegranate-like” powders display a relatively large distribution in the grain’ shape (from elongated with aspect ratio of 4 to equiaxed) as well as in the grain’ size (from as small as 0.5 μm up to as large as 10 μm), which, by very rough estimation, may be considered as bi-modal distribution. Tiny pores are only observed inside the large grains of TiB, indicating the high level of densification at the given conditions. A composite of only 12 wt% Ti has been consolidated to 99.7% of relative density, suggesting an improved densification of the material of high ceramic content.

3.2. Mechanical Properties

The density, hardness, and indentation fracture toughness (IFT) values for pure Ti and various Ti–TiB composites produced by different methods are listed in Table 2. Figure 3 demonstrates the images of fractured SPSeD bulks.

The Vickers’ hardness of TiB is about 1800 HV and, therefore, the high hardness of the TiB rich composite in the current research is ascertained (Table 2). Apart from a high

hardness, a good IFT value ($8.2 \text{ MPa}\cdot\text{m}^{1/2}$) is demonstrated due to the presence of metallic Ti in the composite. In general, it is challenging to produce a composite material with a high content of ceramic phase (here TiB) showing a commendable IFT value, Table 2, as decrease in the IFT and density with an increase in ceramic content is widely reported. However, in the current study, a high relative density and IFT are evidenced even with an extremely high ceramic content.

The SEM image of fractured composite surface, Figure 3, demonstrates significant amount of plastic deformation and few cleavage facets/steps, which are characteristic of a granular fracture. In addition, the river pattern features of the cleavages are also noticed pointing at a brittle mode of fracture. Intergranular as well as transgranular crack propagation is one of the features of composite fracture. It appears that the crack is initiated at a point on the interface of TiB grain and propagated alongside this interface, consuming a large amount of energy, and thus enhancing the fracture toughness. The propagating crack, upon confronting a TiB particle, tends to encircle it and is deflected from its original track. Therefore, the crack deflection mechanism of fracture can be held responsible for improved composite toughening. A similar phenomenon was also reported in [7,25,26].

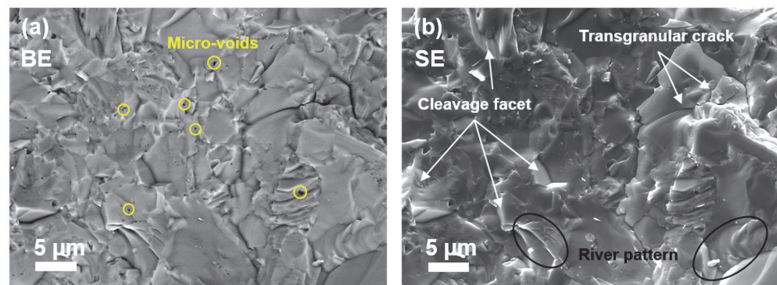


Figure 3. SEM images of fractured cross-sections: (a) Backscattered electron (BE); and (b) secondary electron (SE).

Table 2. Comparison of processing methods, relative density, hardness and indentation fracture toughness of Ti-TiB composites.

Material	Process	Relative Density (%)	Hardness	IFT ($\text{MPa}\cdot\text{m}^{1/2}$)
CpTi [1]	SPS	97.92 ± 0.03	291 ± 10 (HV30)	-
TiB _w -60 wt.% Ti [15]	Mixing + SPS	99.6%	-	9.35
TiB _w -50 wt.% Ti [19]	Mixing + SPS	99.4%	1324 ± 18 (HV30)	10.52
TiB-33 vol% Ti [24]	Ball Milling + Reaction hot pressing	-	1351 (HV50)	-
TiB-30 wt.%Ti [17]	SHS + PHIP (Pseudo Hot Isostatic Pressing)	98.45	87.8 HRA	6.15
TiB-20 wt.%Ti [17]	SHS + PHIP	97.57	86.7 HRA	5.23
TiB-12 wt.% Ti (current work)	SHS + SPS	99.7	1550 ± 26 (HV30)	8.16

3.3. Sliding Wear

Figure 4 demonstrates the effect of temperature and load on the wear rates of the composite along with the counterbody ball. Figure 5 shows the coefficient of friction (CoF) evaluation during sliding tests. Figure 6 displays the scanning electron microscope (SEM) images of the worn surfaces. The XRD pattern of the composite after 800 °C sliding test is given in Figure 7.

The wear rates and CoF values of composite tested at 800 °C are significantly reduced in comparison to RT test (Figures 4 and 5, Table 3). A distinct behavior of material at different load is clearly noticed. At a room temperature, an increase in load results in an expected rise in wear rate. However, at 800 °C, the wear rate is reduced with an increase in the test load.

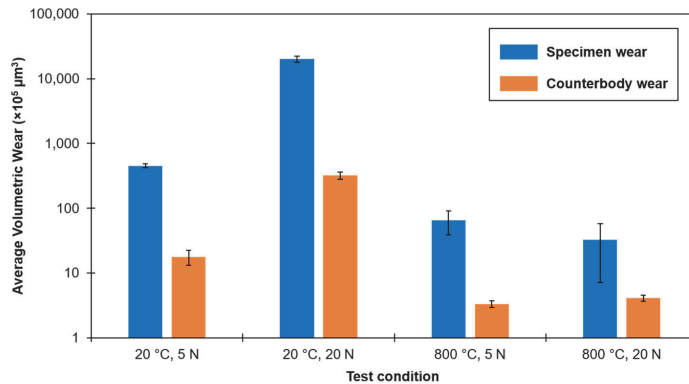


Figure 4. The effect of temperature and load on wear rate of Ti–TiB specimen and alumina counterbody (logarithmic scale).

The coefficient of friction is lower during tests performed at a higher load and/or temperature (Table 3, Figure 5). At a temperature of 800 °C, a lower CoF (during test with 20 N), as expected, resulted in a lower wear rate of material; while at room temperature, a lower CoF (during test with 20 N) resulted in a sufficiently higher wear rate of the Ti–TiB specimen. This can be explained by change in wear mechanism or the formation of new phases. The stabilization of CoF (reduction of fluctuations, running-in period) at a high temperature required significantly less time (100 s) as compared to the test at RT (3000 s), Figure 5. The range of CoF fluctuations and time to stabilization are influenced by properties of material, surface preparation (roughness, defects induced, presence of minor pollutants etc.), as well as mechanisms of tribo-layer formation. The running-in accompanied with formation of a characteristic tribo-layer is an essential process affecting the following steady state wear mechanism and the ultimate wear rate [27]. It is worth to note, that at 800 °C, a short running-in period was seen for both low and high sliding loads. It is important to mention that, at 800 °C, especially with maximum test load (20 N), the CoF is the lowest after restarting (Figure 5), and experiences insignificant growth during each sliding period. This leads to the conclusion that intervals between sliding-oxidation are favorable for tribo-couple. Table 3 specifies the CoFs measured at the end of the tests.

Table 3. Effect of temperature and load on CoF measured at the end of test.

Test Conditions	Final CoF
20 °C, 5 N	0.71 ± 0.02
20 °C, 20 N	0.60 ± 0.02
800 °C, 5 N	0.19 ± 0.02
800 °C, 20 N	0.18 ± 0.02

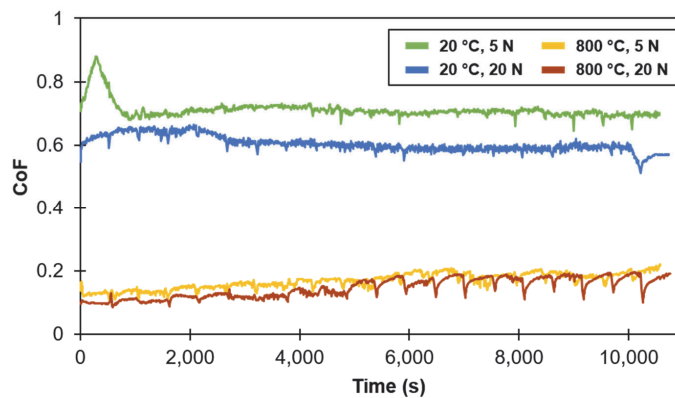


Figure 5. Effect of temperature and load on evolution of coefficient of friction.

Figure 6 illustrates the features of the main wear mechanisms associated with the composite subjected to sliding under given conditions. The composite surface after RT sliding is dominated by the features, which are characteristic of adhesive and delamination wear modes. It is a well-established fact that a long-time sliding results in a higher strain level at the composite surface causing the development of fatigue-driven surface or sub-surface cracks [26], which grow to a critical length during the sequence of sliding cycles, followed by material delamination from the surface. This time-progressive process of delamination can also be observed in Figure 6a, where surface cracks progressively propagate towards other cracks causing detachment of a material from the surface. The detached wear debris at RT may further act as a third body intensifying the wear [28]. Apart from delamination, adhesion and abrasion are the common mechanisms of wear during RT sliding. At a higher load, the adhesion and abrasion mechanisms escalated, resulting in high wear of composite, which is characterized by deep plough grooves and almost doubled width (≈ 1 mm) of a wear track as compared to the test under 5 N load. In all probability, a flash surface temperature is sufficient to cause the material transfer (adhesive wear) from the composite surface to the counterbody. It is confirmed by the fact that a substantial amount of material transfer for RT sliding was encountered on the worn counterbody surface at both tests performed at 5 and 20 N. The transferred material mostly consisted of elements from composite surface, i.e., titanium and boron.

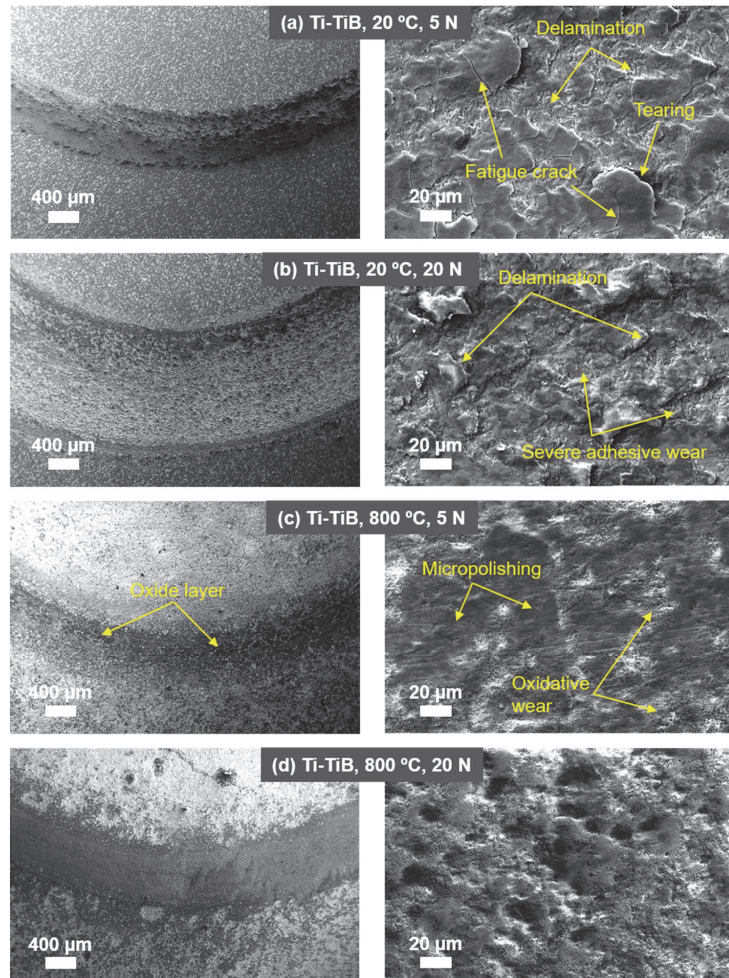


Figure 6. SEM images of composite surfaces with different magnification taken after sliding test. The test conditions are indicated in the figure.

At 800 °C, an oxidative wear has demonstrated a noticeable effect. The frictional surface was dominated by an even oxide layer. In general, the wear at this stage is mainly conditioned by the fragmentation of oxide scales; the direct contact between the alumina ball and the composite surface is limited. The XRD pattern in Figure 7 details the phases on the surface demonstrating the formation of rutile and the presence of boric acid.

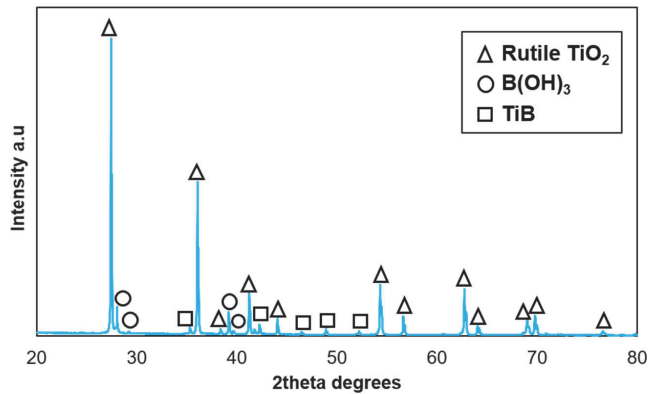


Figure 7. XRD pattern of composite surface after sliding at 800 °C, 20 N.

During cross-sectional examination of the wear tracks on the surface of the composites tested at 800 °C, the development of quite thick ($\approx 8 \mu\text{m}$), uniform, and well-adhered to the parent material tribo-oxide layer was confirmed, Figure 8. The tribo-layer is thick enough to prevent direct contact between the composite surface and alumina counterbody. The oxide layer is worn out during successive sliding cycles, following by rapid re-oxidation of the exposed or damaged surfaces, preventing further contact between the parent surfaces [28]. No considerable difference in thickness and roughness of the developed surface layers inside and outside of the wear track was revealed. Therefore, the counterbody ball was borne by the generated tribo-oxide layer, and there is a low chance of complete removal of tribo-layer and sliding over the unprotected surface. Moreover, at elevated temperatures, the generated third body or retained debris are reported to undergo compaction and contribute to the development of a mechanically mixed layer responsible for a stable CoF and reduced wear rate [9,28]. However, the compaction of debris is much less pronounced at RT. Moreover, the wear is intensified by brittleness of original material, which can be easily fractured by wear debris retained in the wear scar. Apart from oxidation, micropolishing, which is commonly reported phenomenon under elevated and high temperatures sliding [19], can also be considered as one of the wear mechanisms.

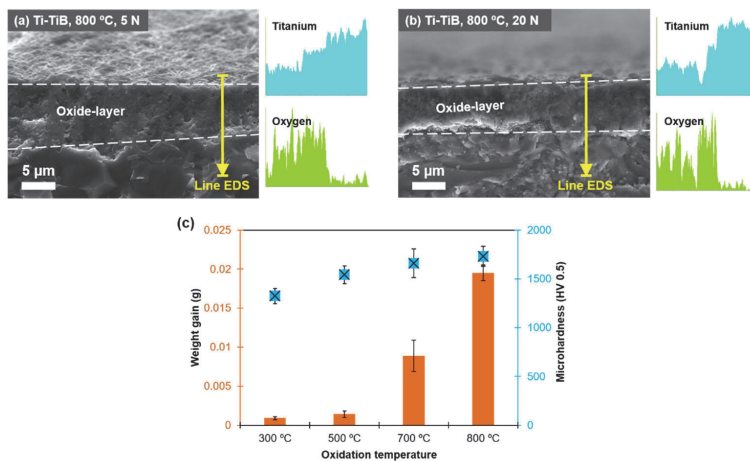


Figure 8. (a,b) SEM images of a central part of wear track cross-section of the composites tested at 800 °C with load of 5 or 20 N; (c) effect of oxidation temperature on weight gain and microhardness of composite.

Figure 8c demonstrates the effect of temperature on surface hardness and weight gain of Ti–TiB composite. All samples show negligible weight change at temperature below 500 °C, suggesting an insignificant oxidation evolution. The material exhibits a substantial weight gain and increased surface hardness at 700 and 800 °C due to the formation of rutile (Table 2). It is well documented that the first phase to form under oxidative media is anatase due to its lower surface energy and its further transformation into a harder and thermodynamically stable rutile at elevated temperature [29]. Therefore, it can be stated that the sliding behavior of composite at 800 °C is positively influenced by the rutile formation, which is a hard, thermodynamically stable, and thick layer of a P–B ratio in between 1–2 characterized by a higher load bearing capacity as compared to anatase.

Apart from rutile, the XRD pattern in Figure 7 reveals boric acid, $B(OH)_3$, presented on the surface of the composite after sliding at 800 °C. The slippery or lubricating behavior of boric acid is detailed elsewhere [30] in imparting a low CoF due to its layered crystal structure. The occurrence of boric acid is conditioned by the oxidation of boron above 600 °C with formation of boric oxide, B_2O_3 as per Equation (3); and further B_2O_3 readily reacts with moisture in humid environment as per Equation (4). A surface film of a lamellar structure (as $B(OH)_3$) consists of the atomic layers aligned parallel to the direction of sliding, causing them to easily slide over one another due to and interlayer slip [5].



Figure 4 demonstrates rather low wear of the counterbody alumina ball at the given sliding conditions. The hardness of alumina is comparable to that of the Ti–TiB composite (HV1450 vs. 1550, respectively); thus, the comparable wear rates of both bodies in contact are expected. Since, during an EDS study (Figure 9c,d), some amount of Ti–TiB specimen material transfer is evident on the Al_2O_3 ball surface. In all probability, the contact area of the ball should have higher temperature due to the fact that it is experiencing continuous friction, while the material of wear scar of the disk is experiencing wear only during passing of the ball and can slightly cool down between such passes.

More intensive transfer of titanium onto the counterbody in the case of RT sliding confirms the evidence of a severe adhesion between tribo-bodies. However, no detectable Ti transfer was recognized after the test conducted at 800 °C. It is understood that boron transfer from the composite to counterbody surface resulted in the formation of lubricious boric acid at elevated temperature sliding, thus minimizing counterbody as well as composite wear. At RT sliding, adhesion and abrasive marks were recognizable on the ball surface (Figure 9a), as the protection of oxide and lubricating boric acid layers is negligible. However, at 800 °C sliding under both loads, no marks of materials adhesion in the worn area were evidenced, Figure 9b. This was also confirmed by EDS analysis (Figure 9d). A smooth, polished surface of counterbody is clearly seen in Figure 9b.

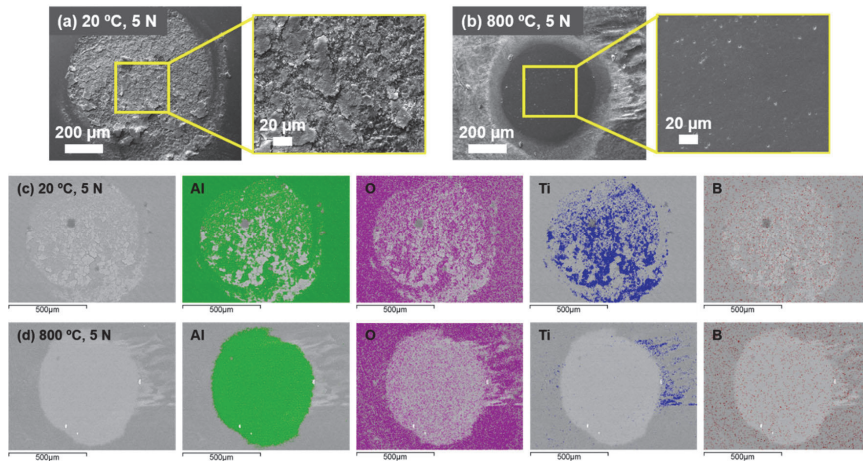


Figure 9. (a,b) SEM images of the counterbody ball worn surface; and (c,d) energy dispersive spectrometer (EDS) mapping of the worn area of the counterbody tested at 20 °C and 800 °C with load of 5 N.

4. Conclusions

In this study, a fully dense and thermodynamically stable TiB–Ti composite of TiB ceramic phase content of ~88 wt.% is densified by spark plasma sintering at a temperature of 1200 °C with the application of 50 MPa pressure during 3 min in vacuum. The “pomegranate-like” powder feedstock is produced with the help of self-propagating high-temperature synthesis of commercially pure boron and titanium at the combustion temperature of 1700 °C. During SPS, the TiB phase is mostly grown as equiaxed grains of a large size distribution. The bulks of TiB–Ti exhibit the hardness of ~1550 HV30 combined with a good indentation fracture toughness of 8.2 MPa·m^{1/2}.

The wear behavior at room and elevated temperature of 800 °C under dry sliding conditions under loads of 5 and 20 N is shown to be highly affected by the temperature of the test. A considerable decrease in wear rate and the coefficient of friction is demonstrated at 800 °C. The protective behavior and a high load bearing capacity of generated tribo-oxide layer at 800 °C is confirmed. The significant decrease in the coefficient of friction (i.e., ~0.18) at elevated temperature is attributed to the generation of lubricious boric acid on the composite surface. Abrasion and adhesion are the main mechanism of wear at room temperature sliding, whereas micropolishing of oxide surface dominates at 800 °C.

Author Contributions: Conceptualization – I.H.; Methodology – M.A. and R.K.; Software – L.L. and R.I.; Validation – I.H., M.A., and R.I.; Formal analysis – I.H., M.A.; Investigation – R.K., L.L. and R.I.; Resources – I.H.; Data curation – I.H.; Writing—original draft preparation, R.K., and L.L.;

Writing—review and editing - I.H.; Supervision - I.H. and M.A.; Project administration - I.H.; Funding acquisition - I.H. All authors have read and agreed to the published version of the manuscript.

Funding: This research was funded by the Estonian Research Council, grants PRG643. (I.H.), M-ERA.Net project “HOTselflub” MOBERA18 N.20097582-CA and M-ERA.Net DURACER18012.

Institutional Review Board Statement: Not applicable.

Informed Consent Statement: Not applicable.

Data Availability Statement: The data presented in this study are available on request from the corresponding author.

Acknowledgments: The authors acknowledge the Estonian Research Council under the grant PRG643 (I. Hussainova), M-ERA.Net project “HOTselflub” MOBERA18 N.20097582-CA and M-ERA.Net DURACER18012. The authors would like to thank PhD Medhat Hussainov and Rainer Traksmaa for powder characterization and XRD analysis, respectively.

Conflicts of Interest: The authors declare no conflict of interest.

References

- Namini, A.S.; Dilawary, S.A.A.; Motallebzadeh, A.; Asl, M.S. Effect of TiB₂ addition on the elevated temperature tribological behavior of spark plasma sintered Ti matrix composite. *Compos. Part B Eng.* **2019**, *172*, 271–280.
- Blau, P.J. Elevated-temperature tribology of metallic materials. *Tribol. Int.* **2010**, *43*, 1203–1208, doi:10.1016/j.triboint.2010.01.003.
- Atar, E.; Kayali, E.S.; Cimenoglu, H. Characteristics and wear performance of borided Ti6Al4V alloy. *Surf. Coat. Technol.* **2008**, *202*, 4583–4590.
- Pu, Y.; Guo, B.; Zhou, J.; Zhang, S.; Zhou, H.; Chen, J. Microstructure and tribological properties of in situ synthesized TiC, TiN, and SiC reinforced Ti3Al intermetallic matrix composite coatings on pure Ti by laser cladding. *Appl. Surf. Sci.* **2008**, *255*, 2697–2703, doi:10.1016/j.apsusc.2008.07.180.
- Kumar, R.; Antonov, M. Self-lubricating materials for extreme temperature tribo-applications. In *Proceedings of the Materials Today: Proceedings*; Elsevier BV: Amsterdam, The Netherlands, 2020, doi:10.1016/j.matpr.2020.10.824.
- Zhang, S.; Wu, W.; Wang, M.; Man, H. In-situ synthesis and wear performance of TiC particle reinforced composite coating on alloy Ti6Al4V. *Surf. Coat. Technol.* **2001**, *138*, 95–100, doi:10.1016/s0257-8972(00)01133-6.
- Morsi, K.; Patel, V.V. Processing and properties of titanium–titanium boride (TiB w) matrix compo-sites—A review. *J. Mater. Sci.* **2007**, *42*, 2037–2047.
- Liu, L.; Minasyan, T.; Ivanov, R.; Aydinian, S.; Hussainova, I. Selective laser melting of TiB₂-Ti compo-site with high content of ceramic phase. *Ceram. Int.* **2020**, *46*, 21128–21135.
- Antonov, M.; Hussainova, I.; Veinthal, R.; Pirso, J. Effect of temperature and load on three-body abra-sion of cermets and steel. *Tribol. Int.* **2012**, *46*, 261–268.
- Mao, Y.S.; Wang, L.; Chen, K.M.; Wang, S.Q.; Cui, X.H. Tribo-layer and its role in dry sliding wear of Ti–6Al–4V alloy. *Wear* **2013**, *297*, 1032–1039.
- Zhang, Q.Y.; Zhou, Y.; Li, X.X.; Wang, L.; Cui, X.H.; Wang, S.Q. Accelerated Formation of Tribo-oxide Layer and Its Effect on Sliding Wear of a Titanium Alloy. *Tribol. Lett.* **2016**, *63*, 1–13, doi:10.1007/s11249-016-0694-7.
- Bertrand, G.K.J.M.; Jarraya, K.; Chaix, J.M. Morphology of oxide scales formed on titanium. *Oxidation Met.* **1984**, *21*, 1–19.
- Qin, Y.; Geng, L.; Ni, D. Dry sliding wear behavior of extruded titanium matrix composite reinforced by in situ TiB whisker and TiC particle. *J. Mater. Sci.* **2011**, *46*, 4980–4985, doi:10.1007/s10853-011-5415-x.
- Dalili, N.; Edrisy, A.; Farokhzadeh, K.; Li, J.; Lo, J.; Riahi, A.R. Improving the wear resistance of Ti–6Al–4V/TiC composites through thermal oxidation (TO). *Wear* **2010**, *269*, 590–601.
- Qin, Y.; Lu, W.; Qin, J.; Zhang, D. Oxidation Behavior of In Situ Synthesized TiB/Ti Composite in Air Environment. *Mater. Trans.* **2004**, *45*, 3241–3246, doi:10.2320/matertrans.45.3241.
- Liu, L.; Aydinian, S.; Minasyan, T.; Hussainova, I. SHS Produced TiB₂-Si Powders for Selective Laser Melting of Ceramic-Based Composite. *Appl. Sci.* **2020**, *10*, 3283, doi:10.3390/app10093283.
- Xinghong, Z.; Qiang, X.; Jiecai, H.; Kvanin, V.L. Self-propagating high temperature combustion syn-thesis of TiB/Ti composites. *Mater. Sci. Eng. A* **2003**, *348*, 41–46.
- Antonov, M.; Hussainova, I. Experimental setup for testing and mapping of high temperature abra-sion and oxidation synergy. *Wear* **2009**, *267*, 1798–1803.
- Kumar, R.; Antonov, M.; Liu, L.; Hussainova, I. Sliding wear performance of in-situ spark plasma sintered Ti-TiBw composite at temperatures up to 900 °C. *Wear* **2021**, *203663*, 203663, doi:10.1016/j.wear.2021.203663.
- Fabijanić, T.A.; Čorić, D.; Musa, M. Šnajdar; Sakoman, M. Vickers Indentation Fracture Toughness of Near-Nano and Nanostructured WC-Co Cemented Carbides. *Metals* **2017**, *7*, 143, doi:10.3390/met7040143.

21. Blau, P.J. Running-in: Art or engineering? *J. Mater. Eng.* **1991**, *13*, 47–53, doi:10.1007/bf02834123.
22. Antonov, M.; Afshari, H.; Baronins, J.; Adoberg, E.; Raadik, T.; Hussainova, I. The effect of temperature and sliding speed on friction and wear of Si₃N₄, Al₂O₃, and ZrO₂ balls tested against AlCrN PVD coating. *Tribol. Int.* **2018**, *118*, 500–514.
23. Kumar, R.; Antonov, M.; Beste, U.; Goljandin, D. Assessment of 3D printed steels and composites intended for wear applications in abrasive, dry or slurry erosive conditions. *International Journal of Refractory Metals and Hard Materials* **2020**, *86*, 105126, doi:10.1016/j.ijrmhm.2019.105126.
24. Bhat, B.R.; Subramanyam, J.; Prasad, V.B. Preparation of Ti-TiB-TiC&Ti-TiB composites by in-situ reaction hot pressing. *Mater. Sci. Eng. A* **2002**, *325*, 126–130.
25. Antonov, M.; Hussainova, I. Cermets surface transformation under erosive and abrasive wear. *Tribol. Int.* **2010**, *43*, 1566–1575, doi:10.1016/j.triboint.2009.12.005.
26. Kumar, R.; Malaval, B.; Antonov, M.; Zhao, G. Performance of polyimide and PTFE based composites under sliding, erosive and high stress abrasive conditions. *Tribol. Int.* **2020**, *147*, 106282, doi:10.1016/j.triboint.2020.106282.
27. Holovenko, Y.; Antonov, M.; Kollo, L.; Hussainova, I. Friction studies of metal surfaces with various 3D printed patterns tested in dry sliding conditions. *Proc. Inst. Mech. Eng. Part J: J. Eng. Tribol.* **2017**, *232*, 43–53, doi:10.1177/1350650117738920.
28. Jiang, J.; Stott, F.; Stack, M. The role of triboparticulates in dry sliding wear. *Tribol. Int.* **1998**, *31*, 245–256, doi:10.1016/s0301-679x(98)00027-9.
29. Hanaor, D.A.H.; Sorrell, C.C. Review of the anatase to rutile phase transformation. *J. Mater. Sci.* **2011**, *46*, 855–874, doi:10.1007/s10853-010-5113-0.
30. Erdemir, A.; Bindal, C.; Zuiker, C.; Savrun, E. Tribology of naturally occurring boric acid films on boron carbide. *Surf. Coat. Technol.* **1996**, *86*, 507–510.

Publication III

Liu, L., Minasyan, T., Ivanov, R., Aydinyan, S., Hussainova, I. (2020). Selective laser melting of TiB₂-Ti composite with high content of ceramic phase. *Ceramics International*, 46(13), 21128-21135.



Contents lists available at ScienceDirect

Ceramics International

journal homepage: www.elsevier.com/locate/ceramint

Selective laser melting of TiB₂-Ti composite with high content of ceramic phase



Le Liu^a, Tatevik Minasyan^a, Roman Ivanov^a, Sofiya Aydynyan^a, Irina Hussainova^{a,b,*}

^a Tallinn University of Technology, Ehitajate 5, 19180, Tallinn, Estonia

^b ITMO University, Kronverksky 49, St. Petersburg, 197101, Russian Federation

ARTICLE INFO

Keywords:

Selective laser melting
Titanium diboride
Composites
Microstructure
Hardness

ABSTRACT

An increasing need in customized ceramics and ceramic-metal composites has driven the development of powders feedstock and procedures for utilization of additive manufacturing for production of mechanically reliable composites. However, processing of materials with a high fraction of ceramic particles is still in its infancy. Herein we report on 3D printing of TiB₂-TiB-Ti composites from TiB₂-Ti powder mixture of high ceramic content (50 wt%TiB₂) by an optimized process of selective laser melting. In-situ synthesized from the mixture of commercially pure Ti and TiB₂ powders, the composites possess up to 20.4 GPa hardness despite of a relatively high porosity of around 8%. Improvement in hardness is mainly due to hardening effect of both TiB and TiB₂ and correlated with an increase in fraction of needle-shaped TiB phase with an increase in laser energy density (LED). Depending on process parameters, an amount of the ceramic phases (needle-shaped TiB and coarse elongated TiB₂) can be customized. The laser energy density significantly affects the development of microstructure and size of the ceramic grains as well as the formation of solidification cracks. This study demonstrates the capacity of AM through SLM to produce the composites of high percentage of ceramic phase.

1. Introduction

The wide industrial use of advanced ceramic materials depends on the technological readiness to fabricate near-net-shaped three-dimensional ceramic-based parts with custom oriented geometry [1–3]. Additive manufacturing (AM), as an intensively developing smart technology, holds a unique position in modern-day product development [3–5]. The growing interest in manufacturing of high-performance complex-shaped components for applications in biomedical, aerospace and automotive industries exemplifies the need for development of materials through AM approaches. Selective laser melting (SLM), as one of the most commercialized and rapid growing AM technique, provides precise regulation of the shape, dimensional accuracy and internal inner architecture of designed objects [5].

Among refractory ceramics, TiB₂ has emerged as an outstanding reinforcing phase for metals and alloys due to the extremely high specific modulus of 125 GPa g cm⁻³, which is desirable in the components where the low weight and stiffness are important. TiB₂ exhibits high melting point (2790 °C), high hardness (27 GPa) and elastic modulus (565 GPa at 23 °C). Therefore, TiB₂ based materials are attractive for applications such as armors, cutting tool composites and crucibles [6]. Furthermore, TiB₂ has a high thermal conductivity (~110 W m⁻¹ K⁻¹

at 25 °C) and a lower coefficient of thermal expansion as compared to titanium, steel, iron based alloys and aluminum (8.4–10.8·10⁻⁶ K⁻¹ for Ti and ~7.2·10⁻⁶ K⁻¹ for TiB₂) [7,8]. Metal-matrix composites with TiB₂ reinforcing phase have increased stiffness, hardness, and wear resistance, along with reduced coefficient of thermal expansion and only a moderate decrease in thermal conductivity. The Al alloy reinforced with up to 15 vol% TiB₂ demonstrated an increase in strength and wear resistance [9]. Fe-TiB₂ (80/20 vol%) composite prepared by aluminothermic reduction of Fe₂O₃, TiO₂ and B₂O₃ powders possessed high hardness, high temperature stability and a better abrasive wear resistance as compared to high-chromium white cast iron [10]. In Ref. [11], Al-7Si with up to 6.8 vol% TiB₂ composites with significant improvement in hardness, yield strength, tensile strength, Young's modulus and wear resistance have been successfully synthesized by salt reaction route.

SLM of materials with a high fraction of ceramic phase, however, is a much more complicated process as compared to metals or metal-matrix composites [12–15]. A direct SLM of high ceramic content components usually results in cracking during the forming process owing to the high melting point of the ceramic powder and contraction during fast cooling after laser irradiation. A viable solution is to coat or mix other materials of a lower melting/softening point, which may

* Corresponding author. Tallinn University of Technology, Ehitajate 5, 19180, Tallinn, Estonia.

E-mail addresses: irina.hussainova@ttu.ee, irina.hussainova@taltech.ee (I. Hussainova).

<https://doi.org/10.1016/j.ceramint.2020.05.189>

Received 22 March 2020; Received in revised form 30 April 2020; Accepted 18 May 2020

Available online 27 May 2020

0272-8842/ © 2020 Elsevier Ltd and Techna Group S.r.l. All rights reserved.

serve as a binder for the ceramic powder. In Ref. [12], the SLM of Ti-B₄C powder mixture has been reported; however, the intended in-situ $3\text{Ti} + \text{B}_4\text{C} \rightarrow \text{TiC} + 2\text{TiB}_2$ reaction did not occur due to the strong dilution of the molten powder blend with the molten substrate material. The in-situ processed Ti-5wt.%TiB composites have been reported to possess full density (> 99%) and remarkably increased hardness [14]. It has been shown, that the relatively small amount of TiB reinforcement is sufficient to increase both stiffness and strength of the composites; moreover the composite with TiB have exhibited an improved thermodynamic and chemical stability at high temperatures.

The in situ TiB formation during reaction of Ti with TiB₂ results in a strong interfacial bonding between the materials of similar densities and thermal expansion coefficients. Therefore, the thermal stresses can be minimized allowing the fabrication of mechanically reliable construct. In this study, the printability of 50 wt%TiB₂-50 wt%Ti composite was examined for the first time. The evolution of the microstructure and mechanical properties during SLM at different process parameters were thoroughly analysed.

2. Experimental

TiB₂-Ti powder mixture was prepared by 2 h a mechanical rotation mixing of Ti (purity > 99.5%, Alfa Aesar, Germany, particle size 325 mesh, $\leq 44 \mu\text{m}$) and TiB₂ (> 99.5% Alfa Aesar, Germany, mean particle size 500 mesh, $\leq 25 \mu\text{m}$) powders during 2 h at a rotation speed of 20 rev min⁻¹, Fig. 1.

SLM process was performed by metal 3D printer (Realizer GmbH SLM-50, Germany) equipped with a Yb:YAG fiber laser with 1070 nm wave length and a maximum output power of 120 W. The laser energy density (LED) was calculated based on laser current, scanning speed, hatching distance and layer thickness. The manufacturing process was carried out in a chamber containing a tightly controlled atmosphere (high purity argon > 99.996 vol%) at oxygen level below 0.5%. The produced solid samples were of a cylindrical shape with 10 mm diameter and 5 mm height.

According to the literature review, the SLM of Ti and Ti-based metal-matrix composites was performed in a wide range of scanning speeds (100–400 mm s⁻¹) [14,16,17]. In this work, lower, higher and reported scanning speeds were applied. Three sets of bulks were produced at: 500 mm s⁻¹ (the first set S1-S5); 290 mm s⁻¹ (the second set S6-S10); and 80 mm s⁻¹ (the third set S11-S15), Table 1. Laser current was changed in a range of 1500–3500 mA with a step of 500 mA for all sets. A “zig-zag” scanning strategy and rotation of a laser scanning direction by 60° on each next layer was exploited. Hatching distance and layer thickness were kept at 60 μm and 25 μm , respectively, for all three sets. All samples were printed on a pure titanium substrate. The overall scheme of the preparation route of TiB₂-Ti bulks and picture of sample S8 are given in Fig. 2.

The SLM processed materials were cut off from the substrate using a wire-cutting machine; ultrasonically cleaned in an acetone solution; then sectioned, grounded and polished for further examinations.

The dimensions were measured using a digital Vernier calliper of

0.01 mm accuracy (Digital Caliper, KS Tools Werkzeuge - Maschinen GmbH, Germany). The density of sintered samples was calculated from geometric dimensions and weight. The Vickers hardness was estimated on the polished surface using a hardness tester (Indentec 5030 SKV) applying a load of 49 N for 10 s. Hardness and density were averaged for 5 measurements.

Morphology and microstructure were examined by a high-resolution scanning electron microscope (HR-SEM Zeiss Merlin) at an accelerating voltage of 15 kV. The SEM images were taken from the polished top surface and the side surface of the samples.

Phase compositions were analysed by X-ray diffraction (XRD; D5005, Bruker, USA) using CuK α 1 radiation ($\lambda = 1.5406 \text{ \AA}$). Relative contents of the phases were estimated by Rietveld refinement method, which was performed by quantitative analysis of the crystalline phases detected by the corresponding XRD patterns.

3. Results and discussion

3.1. Thermodynamics

Thermodynamic calculations reported elsewhere [18] for the Ti-B system revealed that the formation of TiB₂ is a spontaneous process due to negative Gibbs free energy (ΔG_T^0) values regardless the ambient gas pressure, but at high amount of boron phase. Increasing the amount of titanium in the initial mixture favors the formation of titanium monoboride. Accordingly, the formation of pure TiB₂ becomes possible only for the stoichiometric composition of initial mixture (Ti + 2B). In addition, the Gibbs free energies of TiB and TiB₂ formation (–160 kJ/mol and –275 kJ/mol, respectively) are negative, but the value of TiB₂ is lower than this of TiB, which indicates that TiB₂ is of priority to be generated in Ti-B reaction. Thus, the reaction of TiB₂ formation is thermodynamically easier than that of TiB. One important thing needs to be noted is that although the TiB₂ is easier to be generated than TiB in thermodynamic point of view, the diffusion coefficient of boron in TiB₂ to the titanium matrix and the growth rate of TiB is very high, which causes the real product to be TiB, rather than TiB₂. This might be also explained by the following thermodynamic data, i.e. the relationship between standard Gibbs free energy (ΔG) and temperature (T). The variation curve between Gibbs free energy ΔG and temperature T for the TiB₂ + Ti interaction demonstrates that the Gibbs free energy ΔG of the reaction is negative from 3000 °C to 0 °C, which indicates that the reaction between Ti and TiB₂ can be carried out spontaneously at temperatures ranging from 3000 °C to 0 °C. At 0 °C, ΔG value is about –43 kJ/mol, it decreases to –54 kJ/mol at 1500 °C and then increases up to –22 kJ/mol at 3000 °C, however maintaining its negative value in a wide temperature interval (Suppl.Fig.).

Supplementary Figure. The variation curve between Gibbs free energy ΔG (also ΔH , ΔS) and temperature T for the TiB₂ + Ti = 2TiB interaction.

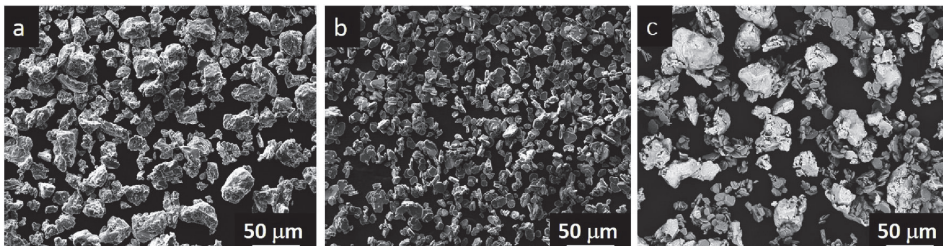


Fig. 1. SEM images of the initial powders Ti (a), TiB₂ (b) and their mixture(c).

Table 1
Parameters of SLM process.

Set	First set					Second set					Third set				
Sample	S1	S2	S3	S4	S5	S6	S7	S8	S9	S10	S11	S12	S13	S14	S15
Scanning speed [$\text{mm}\cdot\text{s}^{-1}$]	500	500	500	500	500	290	290	290	290	290	80	80	80	80	80
Laser current [mA]	1500	2000	2500	3000	3500	1500	2000	2500	3000	3500	1500	2000	2500	3000	3500
Laser power [W]	36	48	60	72	84	36	48	60	72	84	36	48	60	72	84
Laser energy density (LED) [$\text{J}\cdot\text{mm}^{-3}$]	48	64	80	96	112	84	112	140	168	196	300	400	500	600	700

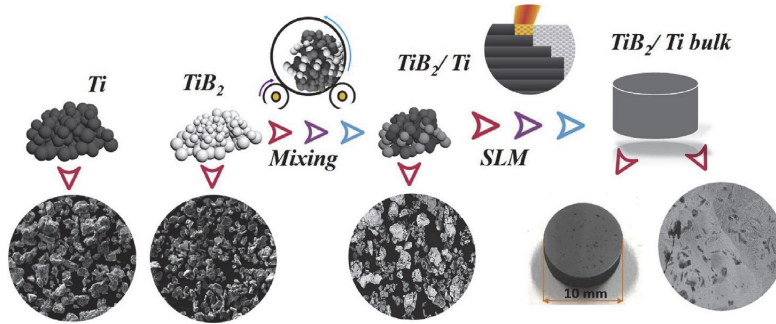


Fig. 2. Schematic of the preparation route of the TiB_2 -Ti bulks and photograph of S8.

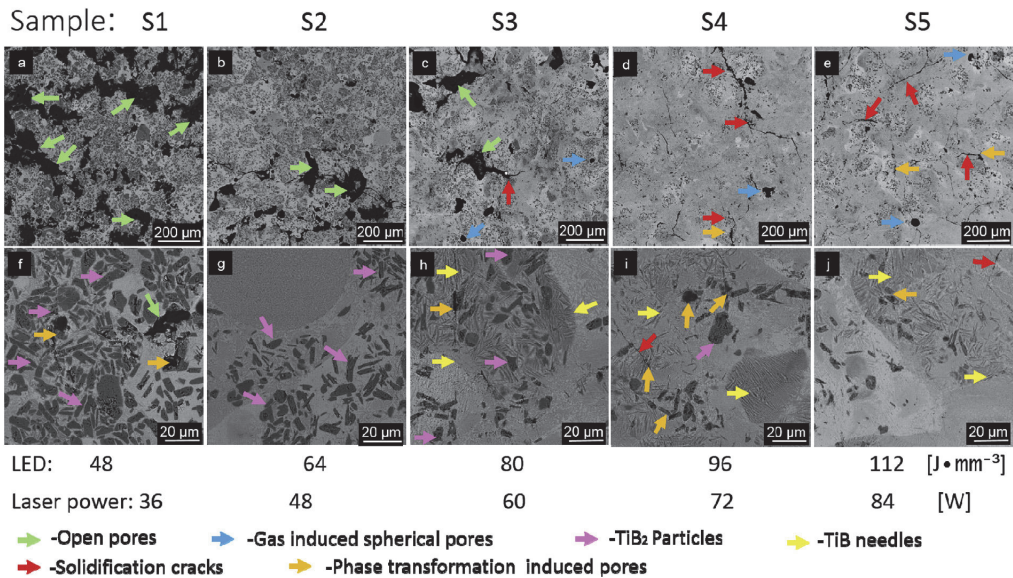


Fig. 3. Top surface SEM images of the first set of samples sintered at 500 mm s^{-1} scanning speed.

3.2. Microstructural analysis

The SEM images of the samples S1-S15 consolidated using laser current of 1500–3500 mA at a scanning speed of 500 mm s^{-1} , 290 mm s^{-1} and 80 mm s^{-1} are depicted in Fig. 3, Fig. 5 and Fig. 6, respectively.

In Fig. 3a, which demonstrates the SEM images depicted from the surface of the materials of the first set, the black regions marked with green arrows are identified as randomly distributed open pores. Porosity can appear because of insufficient melting of the powder (samples S1, S2, Fig. 3) and/or the incomplete flow of material into the melt region; i.e. pores can be classified as metallurgical ones conditioned by

trapped gases, and process-related ones formed due to a high scanning speed providing insufficient time for the molten pool to fill all defects in the previously deposited layer [19]. Fig. 4a–c, e–g shows the microstructural features of the cross-sectioned S4 and its EDS mapping (Fig. 4d) and the XRD pattern (Fig. 4h). Taking into consideration the visible higher concentration of B atoms at the irregular shaped “dark” sites as well as widely reported needle-like morphology of TiB [14,17,19], the presence of 2 ceramic phases can be stated. This fact is also supported by XRD analysis, Fig. 4h.

Samples S4 and S5 prepared at a laser power $\geq 72 \text{ W}$ do not exhibit the unmelted regions; however, they are prone to form solidification cracks during the rapid cooling process as pointed in Fig. 3 by red

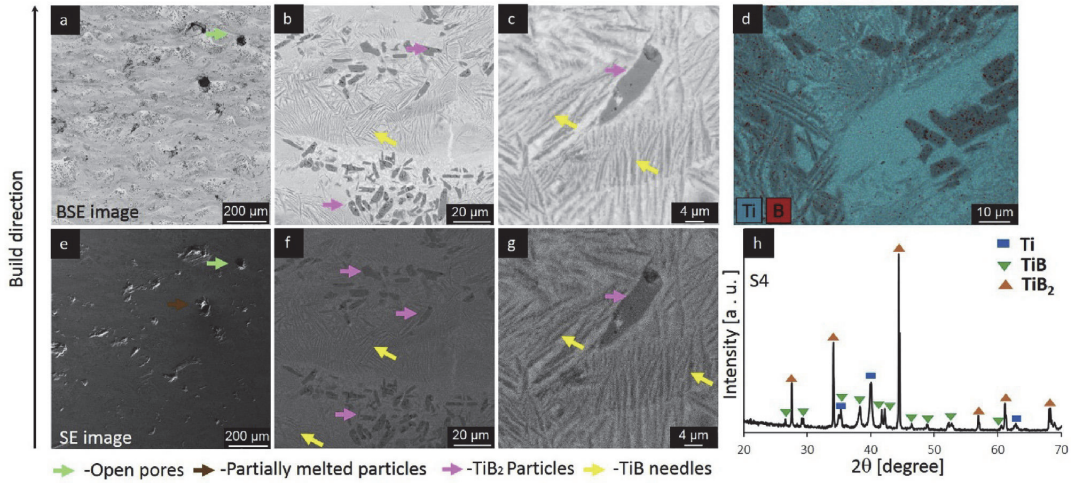


Fig. 4. Backscattered electron (BSE) images (a–c), EDS mapping (d), secondary electron (SE) images (e–g) and the XRD pattern (h) of the Sample 4 longitudinal cross section.

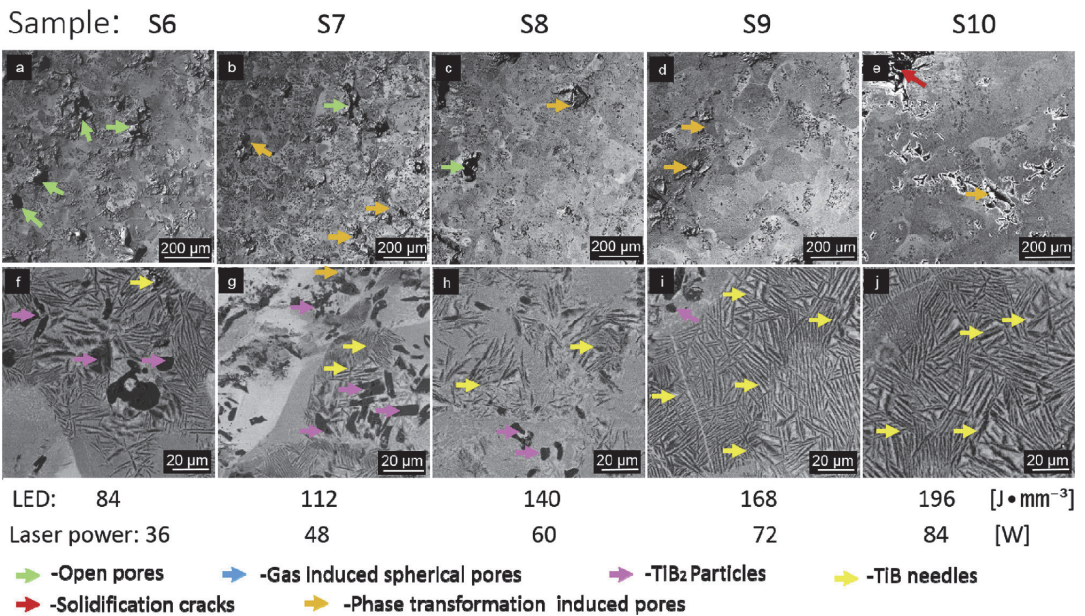


Fig. 5. Top surface SEM images of second set samples sintered at 290 mm s^{-1} scanning speed.

arrows. Applying higher LED, such as 80, 96 and 112 J mm^{-3} , in S3, S4 and S5, the near-spherical shape pores, marked with blue arrows, were formed by the release of entrapped gas from the titanium melting pool during the solidification process. Gas induced pores can be identified because they have a compact spherical shape due to the effect of the pressurized bubble moving route during solidification. Due to the small size of the gas induced pores, they are less harmful for mechanical properties as compared to the open pores. For instance, open pores in S3 appear as a source of cracks, unlike the gas pores, that are found as isolated entities. Open pores are gradually decreasing in size and number with the increasing the LED.

According to $\text{Ti} + \text{TiB}_2 \rightarrow 2\text{TiB}$ in-situ reaction, the development of

TiB phase is detected after the laser treatment. This reaction has negative Gibbs energy value (-43 kJ mol^{-1}) ensuring high probability of the reaction; however, the reaction rate is limited by the low diffusion rate of B in Ti and, therefore, can be controlled. To demonstrate the feasibility of the $\text{Ti} + \text{TiB}_2 = 2\text{TiB}$ reaction further, the existing experimental data was evaluated. TiB_2 particle is difficult to melt, but TiB_2 can be dissolved in liquid Ti, so TiB can be synthesized by an in situ reaction between liquid Ti and the TiB_2 particle. The development of titanium monoborides may be conditioned by melting/solidification process on the hypereutectic side of the eutectic in the binary Ti-B system. Fig. 7a demonstrates the XRD pattern of the initial Ti- TiB_2 mixture and a typical XRD of the sintered material (Sample 9). Apart

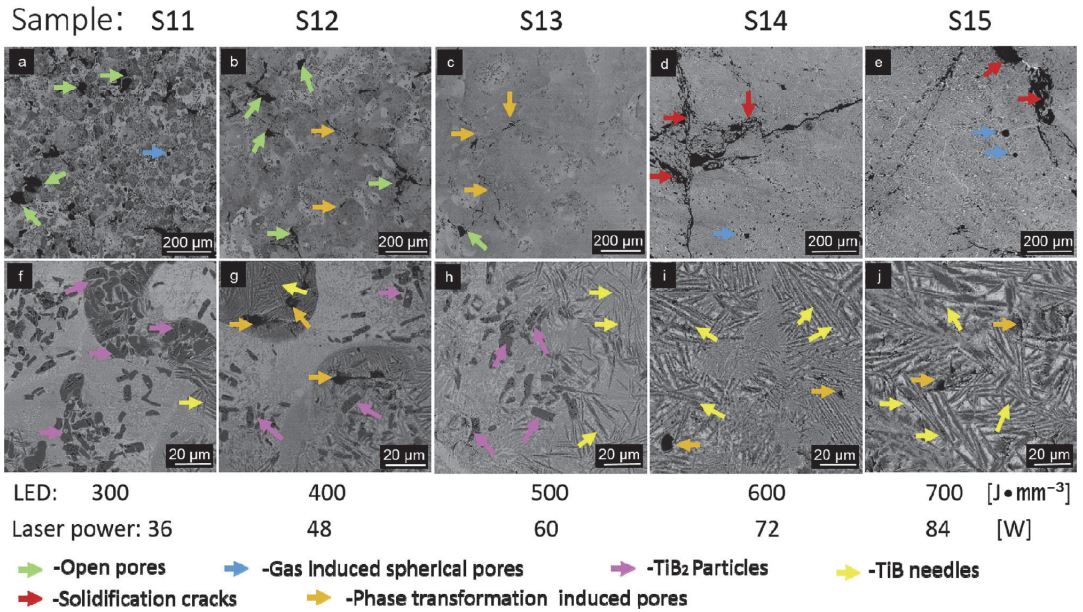


Fig. 6. SEM images of third set samples sintered at 80 mm s⁻¹ scanning speed.

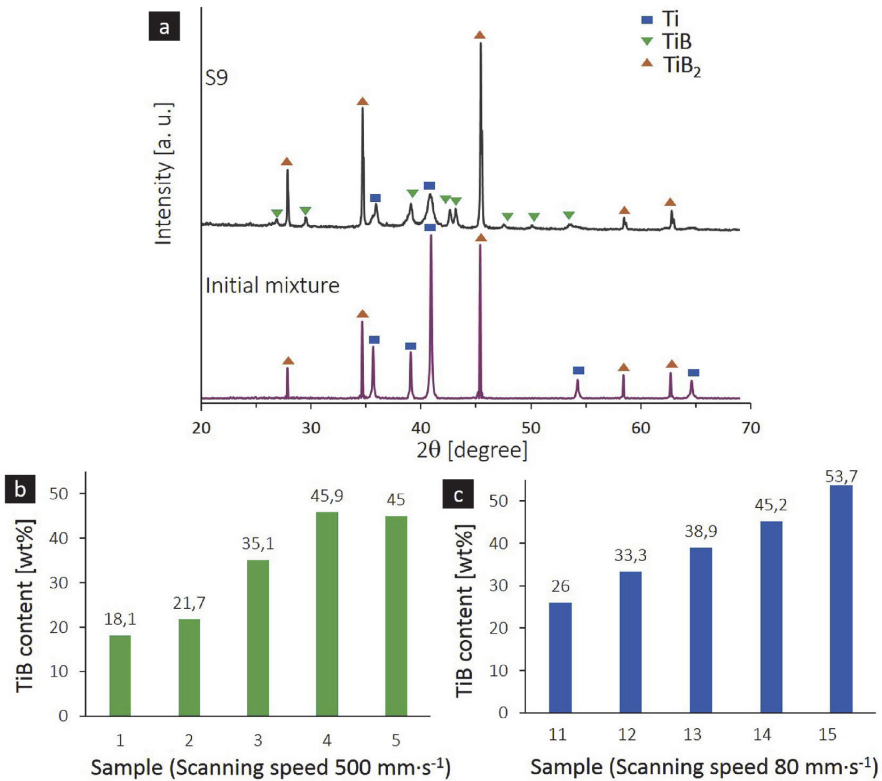


Fig. 7. XRD pattern of initial powder and Sample 9 (a); TiB content (wt. %) in samples S1-S5 (b); and S11-S15 (c) according to Rietveld refinement method.

Table 2
Density and hardness of the TiB₂-TiB-Ti composites.

Sample	S1	S2	S3	S4	S5	S6	S7	S8	S9	S10	S11	S12	S13	S14	S15
Laser energy density (LED) [J·mm ⁻³]	48	64	80	96	112	84	112	140	168	196	300	400	500	600	700
Relative geometric density [%]	~77	~83	~86	~85	~86	~82	~84	~86	~87	~87	~89	~88	~90	~91	~92
Hardness HV5 [GPa]	–	5.5 ± 0.7	9.5 ± 2.3	9.4 ± 2.7	9.6 ± 1.7	5.7 ± 1.0	7.1 ± 0.8	9.6 ± 1.2	12.1 ± 1.1	13.1 ± 1.1	9.4 ± 1.8	10.7 ± 2.5	11.8 ± 1.5	17.2 ± 2.0	20.4 ± 2.5

from the presence of α -Ti, the TiB phase is identified in sintered sample, suggesting reaction between TiB₂ with Ti during SLM. The tiny needle-shaped TiB (marked with bright yellow arrows) and the untransformed TiB₂ (marked with pink arrows) co-exist in many materials, Figs. 3–6. The TiB particles represent either a single “whisker” or a colony of the parallel-oriented whiskers. XRD examinations stated that (010) crystal orientation is faster than that of the (100), (101) and (102) plane directions in the TiB crystal formation process, so a fine needle morphology can be found after SLM process in the TiB₂-Ti system [15]. Several studies reported formation of TiB whiskers with needle-shape morphology inside the Ti matrix [14,17,20]; however, the co-existence of two phases is seldom reported.

Applying a laser scanning speed of 500 mm s⁻¹, the laser treatment time was very short (less than 40 μ m in each exposure point), and the titanium melting pool cannot completely overspread around each TiB₂ particle or entire powder interface, thus generating small pores in the TiB₂ particle transformation areas, marked with orange arrows (Fig. 3). Solidification cracks appear in samples S4 and S5 simultaneously with the phase transformation induced pores (Fig. 3 d,e).

Samples in the second set (Fig. 5) demonstrate a smoother surface of less porosity as compared to the materials of the first set. However, the open porosity in second set of samples (S6-S10) is still noticeable because of the lack of fusion. An increase in LED results in decrease in the level of porosity, while the open pores and phase transformation induced pores co-exist in samples 6–8 produced at the laser power \leq 60 W.

If the applied energy is relatively low, TiB particles are developed as colonies inhomogeneously distributed throughout Ti matrix and alongside TiB₂ (samples S6-S8). At LED > 168 J mm⁻³, the needle-shaped titanium monoborides are relatively uniformly apportioned in the material (samples S9 and S10). The TiB “whiskers” are measured to be 2–5 μ m in width and up to 50 μ m in length representing fibre-like reinforcements.

In the third set, the samples show the same trend regarding a decrease in porosity and an increase in number of cracks. This is because the applied excess energy can result in the formation of solidification cracks propagating across the entire sample (S14 and S15) due to stresses induced between different solidified parts. The areas with a well-recognizable cracks system is demonstrated in Fig. 6d and e. At LED higher than 600 J mm⁻³, it is visible (Fig. 6i and j) that the TiB becomes the dominating phase, and the morphology of needles becomes coarser and uneven. The absence of metallic titanium result in the overall brittleness of the composite; the cracks are unavoidable in the ceramic rich areas.

Fig. 7 comprises the typical XRD pattern of Sample 9 and the TiB content (wt. %) in the SLM processed materials. Fig. 7a reveals α -Ti (hexagonal close packed), TiB₂ and TiB. According to Fig. 7 b,c, the tendency of an increase in TiB amount pointed at the crucial role of the laser power on phase formation. The comparison of the TiB content in the samples treated using the same laser power, but different scanning speed (500 mm s⁻¹ and 80 mm s⁻¹), e.g. S1 with S11 or S5 with S15, although being slightly different, reveals no strict influence of scanning speed on TiB content.

From kinetic point of view, it means the main phase transformation from TiB₂ to TiB is dominated by the reached temperature rather than the cooling speed. Once the temperature is high enough, this transformation is proceeded quickly at excessive Ti condition. In SLM process, the laser power is the main parameter regulating the temperature; and the exposure time (scanning speed) mainly controls the cooling rate of the molten pool. An increase in a laser power results in a higher laser density and, consequently, in a greater effective temperature within a molten pool, providing sufficient energy for TiB “whiskers” growth. For example, at a shorter laser exposure time (fast scanning speed), the cooling rate is fast, the TiB needle-shaped grains appear to be thin and short; while at a longer laser exposure time (slow scanning speed), the cooling rate is slow, the TiB grains have enough time to grow coarse

Table 3
Comparison with other related publications.

Composition (matrix-filler)	Ratio	Method	Relative density [%]	Hardness [GPa]	Ref.
Ti-TiB	91.65/8.35 vol%	SLM	100	3.93 GPa	[14]
316L-TiB ₂	85/15 vol%	SLM	90.03	5.98 GPa	[25]
TiAl-TiB ₂	98/2 wt%	SLM	–	10.57 GPa	[26]
Ti-TiB ₂	93.4/9.6 wt%	SPS	99.55	5.74 GPa	[27]
TiB ₂ -CoCrFeNiTiAl	95/5 wt%	SPS	99.12	23.08 GPa	[28]
TiB ₂ -Si	70/30 wt%	SPS	99.8	10.5 GPa	[29]
TiB ₂ -Ti	50/50 wt%	SLM	92	20.4 GPa	This work

and elongate.

3.3. Mechanical properties

The deviation in diameter of solid cylinder samples after SLM process was estimated to be less than 2%. As specified in Table 2, with an increase in the LED (from 48 to 700 J mm⁻³), the relative geometric density of the bulks increases from 76.7 to 92.0% (about 15%); the hardness increases from 5.53 to 20.38 GPa (about 4 times). As TiB₂, TiB and Ti have very close densities (4.52 g cm⁻³, 4.56 g cm⁻³ and 4.506 g cm⁻³, respectively [21]), the formation of the TiB results in only slight change in density of the obtained TiB₂-TiB-Ti composite.

The measured Vicker's hardness of the SLM processed bulks is ranged from as low as around 5 GPa for porous S1 up to 20 GPa for the densest S15, Table 2, and is below the values reported for pure TiB₂ (~27 GPa) [21,22]. For a composite with 50 wt% of metallic binder of a lower hardness, this decrease in the overall hardness is well understood phenomenon. An increase in fraction of needle-shaped TiB phase with increase in LED and its homogeneous distribution throughout the matrix positively contribute into the overall hardness of the composites. The high-aspect-ratio morphology of reinforcements generally leads to improvement in hardness, stiffness and strength [14,30], hence the samples with a high content of TiB phase exhibit a higher microhardness as compared to other samples of relatively similar level of porosity.

High porosity of the S1 makes the hardness measurements unreliable (Fig. 3 a). Hypothetically, the density of SLM samples should increase with the decrease of the scanning speed [23], such behaviour was observed for the samples S6-S10 sintered at 80 mm s⁻¹ scanning speed, in contrast to the samples S1-S5 sintered at 500 mm s⁻¹. Increasing of LED can generate a larger area of melting pool, which results in a higher density and less cracking. However, an excessive LED supply leads to the solidification cracks (S9, S10).

The dependence of the hardness on porosity level is an established fact – the closed porosity can reduce the hardness exponentially [22]. The hardness correction may roughly be estimated as $H \approx H_0 \times e^{-bP}$, where H is the measured hardness, H_0 is the hardness of the material with no porosity, P is the volume fraction of porosity, and b is a characteristic number for the porosity depending on shape and distribution [24]. In this case, the b factor of 3 was adopted for the dispersed spherical porosity mostly observed in the microstructure of a relatively high density. When the hardness of TiB₂-TiB-Ti composite was corrected for porosity, the value of H_0 was estimated to reach 35 GPa. Table 3 shows a comparison of different Ti-TiB₂ composites, regardless the method of TiB₂ reinforced composite preparation, in which most of the times the content of the metallic matrix was surpassing the content of the filler a couple of times. The measured hardness value of around 20.4 GPa for S15 is comparable with hardness of fully dense TiB₂ – based composites and is much higher than the hardness of other SLM produced samples.

4. Conclusions

In the current work, the TiB₂-TiB-Ti composites were in-situ produced from 50 wt%TiB₂-50 wt%Ti powder mixture by selective laser

melting. The SLM processing resulted in the in-situ development of the multiphase ceramic – metal composites comprising of Ti, TiB and TiB₂ in concentrations controllable by the process parameters. During the laser treatment, needle like TiB colonies were obtained according to TiB₂ + Ti → 2TiB interaction. The size and fraction of TiB phases is affected by the laser energy density and may be tailored with the help of precisely specified process' conditions.

Application of the relatively slow scanning speed (80 mm s⁻¹) and the high laser power (84 mA) results in bulks of > 90% relative geometric density. Hardness of 20.4 GPa, which makes composites to be comparable with similar materials produced by other methods (SPS, for ex.), ensures capability of the SLM to be applied to production of ceramic-metal composites of customized and flexible geometry/architecture. However, further refinement of process parameters is needed for production of fully dense composites.

This study demonstrates the capacity of AM through SLM to produce the composites of high percentage of ceramic phase.

Declaration of competing interest

The authors declare that they have no known competing financial interests or personal relationships that could have appeared to influence the work reported in this paper.

Acknowledgments

This work was supported by the Estonian Research Council grants (PSG220, S. Aydinyan; PRG643, I. Hussainova) and M-ERA.Net project “HOTselflub” MOBERA18. The authors would like to thank also the European Regional Fund, project number 2014-2020.4.01.16-0183 (Smart Industry Centre), as well as Dr. Mart Viljus and Mr. Rainer Traksmaa for SEM and XRD analyses.

Appendix A. Supplementary data

Supplementary data to this article can be found online at <https://doi.org/10.1016/j.ceramint.2020.05.189>.

References

- [1] M. Richardson, B. Haylock, Designer/maker: the rise of additive manufacturing, domestic-scale production and the possible implications for the automotive industry, *Comput. Aided Des. PACE* 2 (2012) 33–48.
- [2] J. Bird, Exploring the 3D printing opportunity, *Financ. Times* (2012) 8–30 Retrieved.
- [3] S. Ford, M. Despeisse, Additive manufacturing and sustainability: an exploratory study of the advantages and challenges, *J. Clean. Prod.* 137 (2016) 1573–1587.
- [4] K.S. Prakash, T. Nancharaih, V.S. Rao, Additive manufacturing techniques in manufacturing-an overview, *Mater. Today: Proc.* 5 (2) (2018) 3873–3882.
- [5] T.D. Ngo, A. Kashani, G. Imbalzano, K.T. Nguyen, D. Hui, Additive manufacturing (3D printing): a review of materials, methods, applications and challenges, *Compos. B Eng.* 143 (2018) 172–196.
- [6] R.G. Munro, Material properties of titanium diboride, *J. Res. Natl. Inst. Stand. Technol.* 105 (5) (2000) 709.
- [7] D. Low, T. Sumii, M. Swain, Thermal expansion coefficient of titanium casting, *J. Oral Rehabil.* 28 (3) (2001) 239–242.
- [8] B. Basu, G.B. Raju, A.K. Suri, Processing and properties of monolithic TiB₂ based materials, *Int. Mater. Rev.* 51 (6) (2006) 352–374.

- [9] S.C. Tjong, K.F. Tam, Mechanical and thermal expansion behavior of hiped aluminum-TiB₂ composites, *Mater. Chem. Phys.* 97 (1) (2006) 91–97.
- [10] A. Anal, T.K. Bandyopadhyay, K. Das, Synthesis and characterization of TiB₂-reinforced iron-based composites, *J. Mater. Process. Technol.* 172 (1) (2006) 70–76.
- [11] S. Kumar, M. Chakraborty, V.S. Sarma, B.S. Murty, Tensile and wear behaviour of in situ Al-7Si/TiB₂ particulate composites, *Wear* 265 (1–2) (2008) 134–142.
- [12] T. Kühnle, K. Partes, In-situ formation of titanium boride and titanium carbide by selective laser melting, *Phys. Procedia* 39 (2012) 432–438.
- [13] Z. Chen, J. Li, et al., 3D printing of ceramics: a review, *J. Eur. Ceram. Soc.* 39 (4) (2019) 661–687.
- [14] H. Attar, M. Bönisch, M. Calin, L.C. Zhang, S. Scudino, J. Eckert, Selective laser melting of in situ titanium–titanium boride composites: processing, microstructure and mechanical properties, *Acta Mater.* 76 (2014) 13–22.
- [15] Z. Lu, J. Cao, et al., Research progress of ceramic matrix composite parts based on additive manufacturing technology, *Virtual Phys. Prototyp.* 14 (4) (2019) 333–348.
- [16] H. Attar, S. Ehtemam-Haghighi, D. Kent, X. Wu, M.S. Dargusch, Comparative study of commercially pure titanium produced by laser engineered net shaping, selective laser melting and casting processes, *Mater. Sci. Eng., A* 705 (2017) 385–393.
- [17] L. Liu, S. Aydinyan, T. Minasyan, I. Hussainova, Selective laser melting of combustion synthesized titanium diboride based composites, *EuroPM 2018* (2018) 978-1-899072-50-7, 3987459.
- [18] X. Ma, C. Li, Z. Du, W. Zhang, Thermodynamic assessment of the Ti–B system, *J. Alloys Compd.* 370 (1–2) (2004) 149–158.
- [19] C. Cai, C. Radoslaw, J.L. Zhang, Q. Yan, S.F. Wen, B. Song, Y.S. Shi, In-situ preparation and formation of TiB/Ti-6Al-4V nanocomposite via laser additive manufacturing: microstructure evolution and tribological behaviour, *Powder Technol.* 342 (2019) 73–84.
- [20] L.J. Huang, F.Y. Yang, H.T. Hu, X.D. Rong, L. Geng, L.Z. Wu, TiB whiskers reinforced high temperature titanium Ti60 alloy composites with novel network microstructure, *Mater. Des.* 51 (2013) 421–426.
- [21] K. Morsi, V.V. Patel, Processing and properties of titanium–titanium boride (TiB_w) matrix composites—a review, *J. Mater. Sci.* 42 (6) (2007) 2037–2047.
- [22] I. Hussainova, N. Voltšihhin, E. Cura, S.P. Hannula, Densification and characterization of spark plasma sintered ZrC–ZrO₂ composites, *Mater. Sci. Eng.* 597 (2014) 75–81.
- [23] M. Badrossamay, E. Yasa, J. Van Vaerenbergh, J.P. Kruth, Improving Productivity Rate in SLM of Commercial Steel Powders, *Technical Paper-Society of Manufacturing Engineers*, 2009, pp. 1–13.
- [24] C.C. Wu, R.W. Rice, Porosity dependence of wear and other mechanical properties on fine-grain alumina and boron carbide (B₄C), *Ceram. Eng. Sci. Proc.* 6 (1985) 977–994.
- [25] B. Al Mangour, D. Grzesiak, J.M. Yang, Rapid fabrication of bulk-form TiB₂/316L stainless steel nanocomposites with novel reinforcement architecture and improved performance by selective laser melting, *J. Alloys Compd.* 680 (2016) 480–493.
- [26] W. Li, Y. Yang, J. Liu, Y. Zhou, M. Li, S. Wen, Y. Shi, Enhanced nanohardness and new insights into texture evolution and phase transformation of TiAl/TiB₂ in-situ metal matrix composites prepared via selective laser melting, *Acta Mater.* 136 (2017) 90–104.
- [27] A.S. Namini, M. Azadbeh, M.S. Asl, Effect of TiB₂ content on the characteristics of spark plasma sintered Ti–TiBw composites, *Adv. Powder Technol.* 28 (6) (2017) 1564–1572.
- [28] W. Ji, J. Zhang, W. Wang, H. Wang, F. Zhang, Y. Wang, Z. Fu, Fabrication and properties of TiB₂-based cermets by spark plasma sintering with CoCrFeNiTiAl high-entropy alloy as sintering aid, *J. Eur. Ceram. Soc.* 35 (3) (2015) 879–886.
- [29] L. Liu, S. Aydinyan, T. Minasyan, J. Baronins, M. Antonov, S. Kharatyan, I. Hussainova, Spark plasma sintering of combustion synthesized TiB₂-Si composite, *Ceram. Modern Tech.* 1 (1) (2019), <https://doi.org/10.29272/cmt.2018.0009>.
- [30] K.B. Panda, K.S. Ravi Chandran, Synthesis of ductile titanium–titanium boride (Ti–TiB) composites with a beta-titanium matrix: the nature of TiB formation and composite properties, *Metall. Mater. Trans.* 34A (2003) 1371.

Publication IV

Liu, L., Minasyan, T., Kamboj, N., Aydinyan, S., Hussainova, I. (2020). Bio-inspired TiB₂-TiB-TiN lattices by selective laser melting. *Materials Letters*, 277, 128337.



ELSEVIER

Contents lists available at ScienceDirect

Materials Letters

journal homepage: www.elsevier.com/locate/mlblueBio-inspired TiB₂-TiB-TiN lattices by selective laser melting

Le Liu, Tatevik Minasyan, Nikhil Kamboj, Sofiya Aydinyan, Irina Hussainova*

Tallinn University of Technology, Ehitajate 5, 19180 Tallinn, Estonia

ARTICLE INFO

Article history:

Received 8 April 2020

Received in revised form 8 July 2020

Accepted 11 July 2020

Available online 15 July 2020

Keywords:

Selective laser melting

Titanium diboride

Titanium monoboride

Titanium nitride

Ceramic composites

Lattice structure

ABSTRACT

Selective laser melting was exploited to fabricate lattice structures from TiB₂-Ti powder mixtures of high ceramic content (50wt.%TiB₂). The lattice structures of 0.8 mm unit cell size were nitridized to produce TiB₂-TiN ceramic-ceramic composite. During processing, TiB₂ is partially transformed into TiB. Lattice structures of the TiB₂-TiB-TiN composite were characterized with ~600 μm pore diameter maintaining 3.5 MPa compressive strength. Due to the viability of TiB₂-TiB-TiN composites, they may be considered as the potential bio-materials.

© 2020 Elsevier B.V. All rights reserved.

1. Introduction

The fast evolution of additive manufacturing (AM) over several decades is a response to the need in complex-shaped products for industry. Metal AM through Laser Powder Bed Fusion (LPBF) has been matured for a wide range of compositions; however, LPBF of ceramic and/or ceramic-based materials is still in infancy [1]. The PBF process of selective laser melting/sintering (SLM/SLS) of ceramics has mostly been focused on alumina and alumina-based composites [2,3]. Recently, an attempt has been made to produce silicon nitride [4], and molybdenum disilicide [5,6] ceramic-matrix composites.

Titanium and titanium-based alloys have been widely used for bio-medical applications due to their unique combination of biocompatibility, high specific strength and good corrosion resistance [7–9]. However, the titanium-based composites can hardly be machined and suffer from low hardness, and poor wear resistance [9,10]. To overcome these obstacles, various ceramic added titanium - matrix composites have been developed. For example, corrosion and wear resistant ceramics of TiB₂, TiC, CrB, SiC and TiN have been predominately linked with commercially pure titanium and Ti6Al4V alloy [8,10–12]. Amongst bio-compatible ceramics, TiB₂ and TiN are considered as the most appropriate materials for the load-bearing implants due to their excellent thermodynamic stability, suitable modulus of elasticity combined with high wear resistance [13,14]. However, the production of porous

titanium-based biomaterials of prescribed porosity and customized design is still a challenging process. A large number of studies is devoted to either bulk samples [15,16] or metal-matrix composites with a high fraction of titanium [17].

Herein, for the first time, we report the fabrication of the bio-inspired TiB₂-TiB-TiN entirely ceramic lattice structures by SLM of TiB₂-Ti powder mixture with a high fraction (50 wt%) of ceramic phase, and subsequent nitridation. As the optimum pore size (300–800 μm) plays a decisive role in osteointegration of the mangled bone to ensure influx of the body fluids and ingrowth of the capillaries, the pore size of 800 μm has been modelled to be applicable of reconstructing bone cavities. However, the bio-response of the materials is out of scope of the present study.

2. Experimental

The mixture of 50 wt.%TiB₂ and Ti was prepared through 2 h mechanical rotation mixing of commercially pure Ti (purity > 99.5%, Alfa Aesar, Germany, particle size-325 mesh) and TiB₂ (>99.5%, Alfa Aesar, Germany, particle size-500 mesh) powders.

SLM process was performed in metal 3D printer (Realizer GmbH SLM-50, Germany) equipped with a Yb:YAG fiber laser of 1070 nm wave length. Lattice structures with 0.8 mm unit cell (tripod structure turn round 90°symmetry with 400 mm diameter strut size to have about 800 μm hexagon pore) and porosity of 60% were designed with SolidWorks software; and were produced in a cylindrical shape with 10 mm diameter and 5 mm height.

Based on the parametric study, the laser current of 2000 mA corresponding to the laser energy density (LED) of 400 J·mm⁻³

* Corresponding author at: Tallinn University of Technology, Estonia.
E-mail address: irina.hussainova@taltech.ee (I. Hussainova).

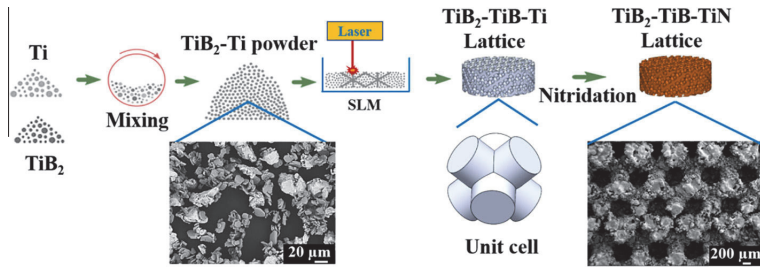


Fig. 1. Schematic of preparation route of the $\text{TiB}_2\text{-TiB-TiN}$ lattices.

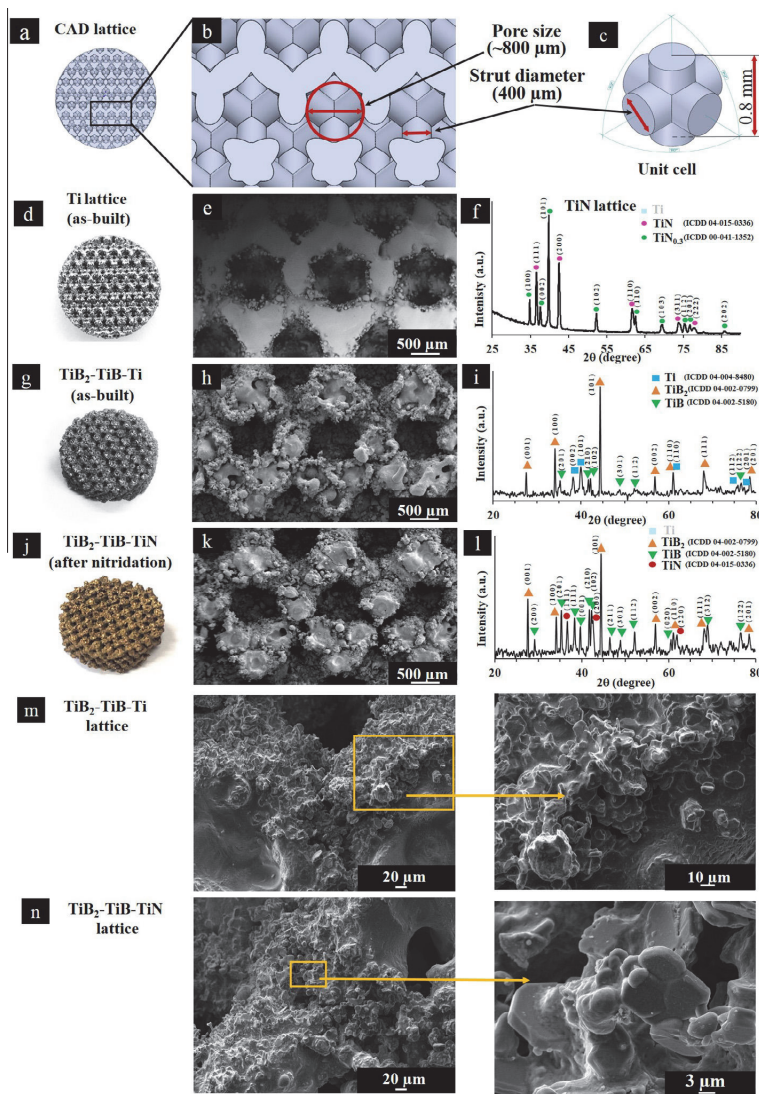


Fig. 2. Top view of CAD model (a,b) and the unit cell (c); general view, SEM images of pure Ti lattice L0 (d,e) and XRD pattern of TiN lattice (f); general view, SEM images and XRD pattern of $\text{TiB}_2\text{-TiB-Ti}$ lattice L1 (g,h,i) and $\text{TiB}_2\text{-TiB-TiN}$ lattice (j,k,l); SEM images of the struts (m,n).

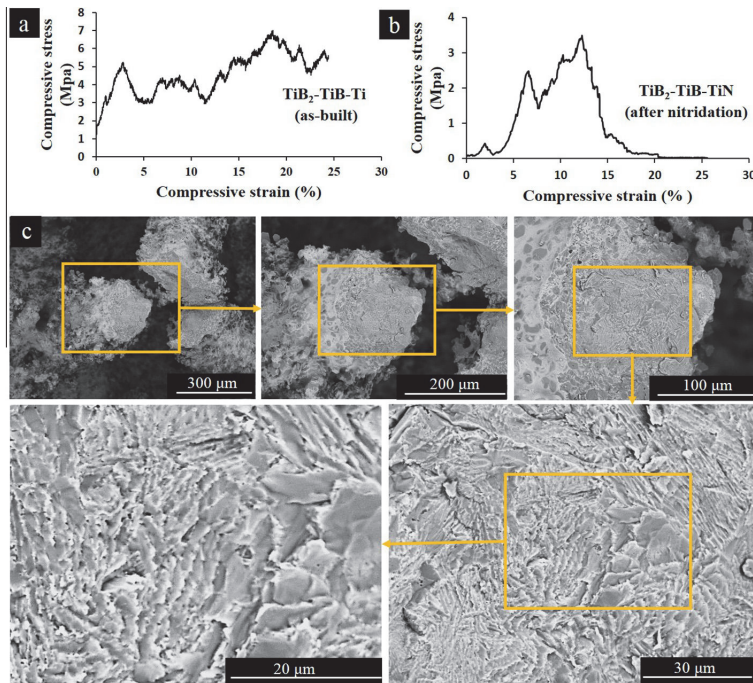


Fig. 3. Compressive stress - strain curves of $\text{TiB}_2\text{-TiB-Ti}$ lattice (L1) before (a) and after (b) nitridation; (c) - SEM image of $\text{TiB}_2\text{-TiB-Ti}$ strut fracture.

was applied at a fixed scanning speed of $80 \text{ mm}\cdot\text{s}^{-1}$ and a hatching distance of $60 \mu\text{m}$, keeping layer thickness of $25 \mu\text{m}$. The lattice sample produced from Ti-TiB_2 mixture was named as L1 and pure Ti lattice sample (L0) fabricated at the same conditions was used as reference.

The printed cellular lattices were heat treated in a furnace (WEBB, USA) at $10 \text{ }^\circ\text{C}\cdot\text{min}^{-1}$ heating rate up to $1100 \text{ }^\circ\text{C}$ in a nitrogen gas flow of $200 \text{ ml}\cdot\text{min}^{-1}$ (purity 99.999 vol%) for 3 h. The nitridation was performed to convert the SLM produced ceramic-metal lattices into completely ceramic structures. The overall scheme of the process is depicted in Fig. 1.

Microstructural analysis was performed by a high-resolution scanning electron microscope (HR-SEM Zeiss Merlin). Phase composition was examined by X-ray diffraction (XRD; D5005, Bruker, USA). The relative content of phases was estimated by the Rietveld refinement method. Compressive strength tests were performed by Zwick universal test machine (ZwischRoell Group, Germany). The maximum load applied is 550 N for $\text{TiB}_2\text{-TiB-Ti}$ and 255 N for $\text{TiB}_2\text{-TiB-TiN}$. The strain rate (0.1 min^{-1}) is chosen according to ISO 13314:2011 standard.

3. Results and discussion

Fig. 2 demonstrates the general view, SEM images and the XRD patterns of the produced structures. The SEM images of the as-built $\text{TiB}_2\text{-Ti}$ structures (L1) demonstrate that the strut diameters are varied in a range of $510\text{--}560 \mu\text{m}$; and, correspondingly, the pore size are from 550 to $630 \mu\text{m}$ (Fig. 2 h). The lattice L1 has relatively thicker struts as compared to the reference lattice (L0, Fig. 2 d, e) and a CAD module (Fig. 2 a, b). This is conditioned by the fact that for the ceramic-metal lattice, the powder mixture was prone to be sintered by the applied heat and powder particles tend to adhere the lattice struts widening the strut diameter.

The XRD pattern of L1 indicates the formation of TiB phase coexisting together with TiB_2 after the SLM processing (Fig. 3i); therefore, the sample composition may be specified as $\text{TiB}_2\text{-TiB-Ti}$. After nitridation of lattices, an appearance of yellow-brownish colour points at the formation of TiN phase in account of titanium (Fig. 2 j). However, for the nitridized L0 lattice, $\text{TiN}_{0.3}$ phase along with TiN was observed (Fig. 3f) stating incomplete nitridation of Ti under the same heating conditions as were used for L1 (Table 1). After the nitridation of $\text{TiB}_2\text{-TiB-Ti}$ lattice (L1), an increase of TiB and decrease of TiB_2 content was detected (Table 1), which attribute to Ti participation in formation of both TiN and TiB phases according to $\text{TiB}_2 + \text{Ti} \rightarrow 2\text{TiB}$ reaction started during room temperature ball milling; and $2\text{Ti} + \text{N}_2 \rightarrow 2\text{TiN}$ reaction at $T > 800 \text{ }^\circ\text{C}$. In principal, the chemical bonding positively affects the maintenance of structures; and, since the density and the coefficient of thermal expansion (CTE) of the TiN ($5.22 \text{ g}\cdot\text{cm}^{-3}$, $9.35 \times 10^{-6} \text{ }^\circ\text{C}^{-1}$) does not significantly differ from the density and CTE of TiB_2 ($4.52 \text{ g}\cdot\text{cm}^{-3}$, $-7.2 \times 10^{-6} \text{ }^\circ\text{C}^{-1}$), TiB ($4.56 \text{ g}\cdot\text{cm}^{-3}$, $7.15 \times 10^{-6} \text{ }^\circ\text{C}^{-1}$) and Ti ($4.506 \text{ g}\cdot\text{cm}^{-3}$, $8.4\text{--}10.8 \times 10^{-6} \text{ }^\circ\text{C}^{-1}$), the change in geometrical

Table 1
Phase composition of L0 and L1 lattices after SLM and nitridation.

Sample ID	Phase Composition	Content (wt.%)	
		After SLM	After nitridation
L0	Ti	100	0
	TiN	0	54.4
	$\text{TiN}_{0.3}$	0	45.6
L1	Ti	21.1	0
	TiB_2	46.3	23.5
	TiB	32.6	37.3
	TiN	0	39.2

parameters of the lattices after the nitridation is not noticeable (Fig. 2 h,k,n).

The compressive stress – strain curves of the produced structures are given in Fig. 3. Commonly, the cellular structures demonstrate three characteristic regions: (i) linear or non-linear elastic deformation, which is followed by (ii) drop-in to a short plateau experienced stress fluctuations, and (iii) densification (not observed here). In all probability, the first peak is associated with crush of some struts, where the overall load-bearing capacity is significantly less as compared to other struts due to internal defects of the structure. According to the compression tests, the ultimate strengths (σ_u) are 7 MPa and 3.5 MPa, the estimated compressive moduli of elasticity are 0.53 ± 0.15 and 0.28 ± 0.16 GPa, the compressive strains $\sim 25\%$, correspondingly, for lattices before and after nitridation. The fracture surface of strut (Fig. 3c) demonstrates regular stepped cleavage planes indicating typical brittle fracture.

Trabecular bone with porosity of 50–90% and pores of 200–600 μm possesses compressive strength of 2–12 MPa and modulus of elasticity of 0.3–17 GPa [18,19]. Therefore, the composites of TiB₂-TiB-TiN, comprising the similar properties, may be considered as the potential substitutes to fill and reconstruct bone cavities or areas of bone loss caused by traumas or bone disease.

4. Conclusions

The TiB₂-TiB-Ti cellular structures were successfully produced from the 50 wt%TiB₂-50 wt%Ti powder mixtures by selective laser melting exploiting the laser current of 2000 mA corresponding to the laser energy density (LED) of 400 J·mm⁻³. Nitridation of the structures resulted in the development of TiN and formation of the TiB₂-TiB-TiN ceramic lattices without significant deterioration of the geometrical parameters of the designed product. A potential of the material for bio-applications is the next step of the study.

CRediT authorship contribution statement

Le Liu: Methodology, Software, Investigation, Writing - original draft. **Tatevik Minasyan:** Methodology, Formal analysis, Investigation, Writing - original draft. **Nikhil Kamboj:** Investigation. **Sofiya Aydinyan:** Conceptualization, Validation, Formal analysis, Resources, Data curation, Writing - review & editing, Supervision, Funding acquisition. **Irina Hussainova:** Conceptualization, Validation, Formal analysis, Resources, Data curation, Writing - review & editing, Supervision, Project administration, Funding acquisition.

Declaration of Competing Interest

The authors declare that they have no known competing financial interests or personal relationships that could have appeared to influence the work reported in this paper.

Acknowledgment

This work was supported by the Estonian Research Council grants (PSG220, S. Aydinyan and PRG643, I. Hussainova). The authors would like to thank PhD Mart Viljus and Rainer Traksmaa for SEM and XRD analyses.

References

- [1] S. Ford, M. Despeisse, Additive manufacturing and sustainability: an exploratory study of the advantages and challenges, *J. Clean. Prod.* 137 (2016) 1573–1587, <https://doi.org/10.1016/j.jclepro.2016.04.150>.
- [2] T.D. Ngo et al., Additive manufacturing (3D printing): A review of materials, methods, applications and challenges, *Compos. B. Eng.* 143 (2018) 172–196, <https://doi.org/10.1016/j.compositesb.2018.02.012>.
- [3] E. Santecchia et al., Laser Powder Bed Fusion: tailoring the microstructure of alloys for biomedical applications, *Mater. Today: Proceedings.* 19 (2019) 24–32, <https://doi.org/10.1016/j.matpr.2019.07.652>.
- [4] T. Minasyan et al., A novel approach to fabricate Si₃N₄ by selective laser melting, *Ceram. Int.* 44 (2018) 13689–13694, <https://doi.org/10.1016/j.ceramint.2018.04.208>.
- [5] T. Minasyan et al., Additively manufactured mesostructured MoSi₂-Si₃N₄ ceramic lattice, *Ceram. Int.* 45 (8) (2019) 9926–9933, <https://doi.org/10.1016/j.ceramint.2019.02.035>.
- [6] T. Minasyan, M. Aghayan, S. Aydinyan, L. Liu, I. Hussainova, Combustion synthesis of MoSi₂ based composite and selective laser sintering thereof, *J. Eur. Ceram. Soc.* 38 (11) (2018) 3814–3821, <https://doi.org/10.1016/j.jeurceramsoc.2018.04.043>.
- [7] M. Geetha, et al., Ti based biomaterials, the ultimate choice for orthopaedic implants—a review, *Prog. Mater. Sci.* 54(3) (2009) 397–425, <https://doi.org/10.1016/j.pmatsci.2008.06.004>.
- [8] L.C. Zhang, H. Attar, Selective laser melting of titanium alloys and titanium matrix composites for biomedical applications: a review, *Adv. Eng. Mater.* 18 (4) (2016) 463–475, <https://doi.org/10.1002/adem.201500419>.
- [9] H. Attar et al., Mechanical behavior of porous pure Ti and Ti-TiB composite materials manufactured by selective laser melting, *Mater. Sci. Eng. A.* 625 (2015) 350–356, <https://doi.org/10.1016/j.msea.2014.12.036>.
- [10] C. Yan et al., Microstructural and surface modifications and hydroxyapatite coating of Ti-6Al-4V triply periodic minimal surface lattices fabricated by selective laser melting, *Mater. Sci. Eng. C* 75 (2017) 1515–1524.
- [11] R.P. van Hove et al., Titanium-nitride coating of orthopaedic implants: a review of the literature, *Biomed. Res. Int.* (2015), <https://doi.org/10.1155/2015/485975>.
- [12] F.M. Makau et al., Viability of titanium-titanium boride composite as a biomaterial, *ISRN Biomaterials.* (2013), <https://doi.org/10.5402/2013/970535>.
- [13] Y. Li, K. Su, P. Bai, L. Wu, Microstructure and property characterization of Ti/TiBCN reinforced Ti based composite coatings fabricated by laser cladding with different scanning speed, *Mater. Charact.* 159 (2020), <https://doi.org/10.1016/j.matchar.2019.110023> 110023.
- [14] T. Kühnle, K. Partes, In-situ formation of titanium boride and titanium carbide by selective laser melting, *Phys. Procedia.* 39 (2012) 432–438, <https://doi.org/10.1016/j.phpro.2012.10.058>.
- [15] H. Attar et al., Selective laser melting of in situ titanium-titanium boride composites: processing, microstructure and mechanical properties, *Acta Mater.* 76 (2014) 13–22, <https://doi.org/10.1016/j.actamat.2014.05.022>.
- [16] L. Liu, et al., Selective laser melting of combustion synthesized titanium diboride based composites, *EuroPM* (2018). ISBN: 978-1-899072-50-7, 3987459.
- [17] C. Cai et al., In-situ preparation and formation of TiB/Ti-6Al-4V nanocomposite via laser additive manufacturing: Microstructure evolution and tribological behaviour, *Powder Technol.* 342 (2019) 73–84, <https://doi.org/10.1016/j.powtec.2018.09.088>.
- [18] N. Kamboj et al., Novel silicon-wollastonite scaffolds for bone tissue engineering, *Ceram. Int.* <https://doi.org/10.1016/j.ceramint.2019.08.208>.
- [19] D. Wu et al., Young's modulus of trabecular bone at the tissue level: a review, *Acta Biomaterialia* 78 (2018) 1–12.

Publication V

Liu, L., Aydinyan, S., Minasyan, T., Hussainova, I. (2020). SHS Produced TiB₂-Si Powders for Selective Laser Melting of Ceramic-Based Composite. Applied Sciences, 10 (9), 3283.

Article

SHS Produced TiB₂-Si Powders for Selective Laser Melting of Ceramic-Based Composite

Le Liu, Sofiya Aydinian, Tatevik Minasyan and Irina Hussainova *

Department of Industrial and Mechanical Engineering, Tallinn University of Technology, Ehitajate 5, 19180 Tallinn, Estonia; le.liu@taltech.ee (L.L.); sofiya.aydinian@taltech.ee (S.A.); tatevik.minasyan@taltech.ee (T.M.)

* Correspondence: irina.hussainova@taltech.ee; Tel.: +372-58143868

Received: 9 March 2020; Accepted: 4 May 2020; Published: 8 May 2020

Abstract: One of the main limitations for widespread additive manufacturing is availability and processability of the precursor materials feedstock. For the first time, this study reports the development of a “pomegranate-like” structured TiB₂-Si ceramic-metalloid powder feedstock suitable for selective laser melting (SLM) of ceramic-based composite. The powder was produced via self-propagating high temperature synthesis (SHS) at a moderate combustion temperature of 1530 °C. The effective activation energy in the Ti-B-Si system for the slow step of the combustion process was estimated as 184 kJ. Conditions of SHS process demonstrated a strong influence on the properties of produced powders and, therefore, on SLM parameters and properties of the printed materials. The powders have demonstrated a high performance for manufacturing bulks of 56 wt%TiB₂-44 wt%Si ceramic-based composite.

Keywords: titanium diboride; ceramic composite; selective laser melting; self-propagating high-temperature synthesis

1. Introduction

Recent progress in materials science and technology has established a new paradigm in producing visual models of 3D architectures by additive manufacturing (AM) or 3D printing. AM represents a continuously growing multi-billion-dollar industry and has a profound impact on society and culture [1–3] as this technology allows for the fabrication of precisely dimensioned high-value products with specified internal features without extensive tooling.

The growing interest in the manufacturing of high-performance components for applications in biomedical, aerospace, and automotive industries exemplifies the need for development of high-temperature (HT) ceramic materials with the help of AM [4]. While still at its infancy, direct AM processing of ceramics or ceramic-based composites requires the development of specific precursor materials and procedures to sinter them.

Thorough selection of feedstock powders, which highly affect structures, properties, and performance of final product, is urgently needed for the fabrication of defect-free, structurally sound, and reliable AM parts. An ability to add functionality requires not only the precise control over the process, but also the efficiency of powders used. Production of AM parts with consistent, repeatable, and predictable characteristics depends on input materials. Although a wide variety of available methods offer powerful features and impressive capabilities, one of the key hurdles impeding wider application of AM is the current severe limitation of materials feedstock suitable for direct or indirect AM processing [4,5]. The main advantage of the direct AM route is a simultaneous combination of forming and densification steps, which allows generation of the final component without any post-treatment. The direct selective laser melting (SLM) is one of the most convenient and reliable methods for producing polymer- and/or metal-matrix composites [3,4]. A relatively wide range of metallic

powders has been developed for AM; however, there is a lack of ceramic or ceramic-based powders available for AM through SLM. The process of building defect-free dense ceramic parts by SLM remains challenging due to the extremely high melting point, poor thermal shock resistance, and low or no plasticity of ceramics [5,6]. Commonly, the components fabricated by the direct SLM exhibit a high level of porosity and poor mechanical properties. One of the approaches is combining ceramic particles with a metal/metalloid binder, which ideally represents core-shell structures with a ceramic core responsible for mechanical properties and a metallic shell needed for laser absorptivity and material ductility. Production of custom-made items of a high performance and economic efficiency necessitates the utilization of powdered feedstock, which meets the requirements posed by the AM process conditions [7]. Therefore, the development of powder materials with tailorable physical and chemical properties has attracted a great deal of attention in the research community and industry.

The quality of the feedstock powders largely depends on manufacturing process. The alloy powders are mainly prepared with the help of either the gas atomization process, rotary atomization process, or plasma rotating electrode process (PREP) [8]. The importance of a cost-effective production of powders with controlled particle size distribution and purity is a driving force for the development of several innovative concepts.

We report on the exploitation of the energy-efficient and time-saving method of self-propagating high-temperature synthesis (SHS) or combustion synthesis (CS) [9,10] to design and produce the ceramic-metal powders for AM process [11,12]. We demonstrate the “pomegranate-like” TiB₂-Si powder particulates to be suitable for SLM of the ceramic-based composite of high ceramic fraction.

The main characteristics of the feedstock materials, which govern the powders flowability during the layer building, include shape, size distribution, surface morphology, and composition [8]. Fine particles may undergo a significant aggregation, while large particles reduce the maximum layer packing density. Optimization and precise control of combustion synthesis (e.g., combustion temperature, velocity, cooling rate, etc.) ensure production of the feedstock exhibiting the prerequisite characteristics.

An increasing demand for properly designed engineering ceramics needed for armor, hypersonic aerospace vehicles, and electronically conductive ceramics has resumed an interest in titanium diboride-based materials due to their high melting point and high temperature stability, remarkable hardness and stiffness combined with a good fracture toughness, and their electrical- and thermal-conductivity [13]. The main limiting factor for wide application of these materials is their poor sinterability related to the exaggerated grain growth and spontaneous mechanical degradation by an internal stress-induced cracking during cooling from a high sintering temperature [13,14]. Another disadvantage is reasoned by the economic factors, particularly the high cost of the consolidation ongoing at temperatures in the range of 1800–2300 °C. One of the approaches to fabricate the materials of high density is a liquid phase sintering with metallic additives, which promotes a fast particle re-arrangement and further densification [15]. The liquid phase sintering, however, also fosters rapid mass transport through the melt and considerably accelerates grain growth. Therefore, to prevent the grain growth, the use of a minimum volume of liquid phase or the implementation of grain growth retarding additives is needed.

The drawbacks in producing and shaping products are the main concerns, which can be solved by a powder-based AM technique such as SLM enabling layer-by-layer fabrication of complex 3D structures. In [16], the fabrication of TiB₂ reinforced Al-matrix composites by the combustion synthesis was reported; however, the printed parts of uncontrolled porosity were obtained. TiB₂ decorated AlSi10Mg composite (NTD-Al) powder was prepared in [17] using a gas-atomization procedure. Ti-TiB (monoboride) cermets were in situ produced from Ti-(5–15 wt%TiB₂) mixtures using SLM, and they demonstrated promising results for future developments [18–20]; however, titanium diboride based ceramics have not yet been produced with the help of AM.

The present work reports a strategy for the preparation of TiB₂-Si powders for AM by the self-propagating high temperature synthesis (SHS). TiB₂-Si bulks were fabricated out of the combustion synthesized “pomegranate-like” TiB₂-Si precursor powders, which, to the best of our knowledge, are unique and have not been yet documented elsewhere.

Laser melting of a single-component powder (either Si or TiB₂) is a rather complicated process due to a very narrow processing window, especially for ceramics of a high melting point. A tendency of melt surface to shrink and minimize the surface energy results in the formation of re-solidified droplets. Therefore, the high-melting point powders (such as TiB₂) are usually mixed with the relatively low-melting point binding powders (here Si). The addition of silicon to TiB₂ yields to increase fluidity, which reduces cracking during solidification and minimizes shrinkage porosity. The presence of silicon significantly decreases the surface tension and viscosity of the pool. The optical properties of silicon, studied in a broad range of laser wavelength (500–1500 nm) under the atmospheric pressure, demonstrated that an average absorption of a silicon slab (20–260 μm) makes 61%, 41%, and 0.5% at 500 nm, 1000 nm, and 1500 nm of laser wavelength, respectively [21]. Generally, powdered materials exhibit a significantly higher absorptance than their dense form; thus, silicon absorption at 1.07 μm wavelength of Yb-fiber laser is > 41%. On the other hand, borides have been shown to be good absorbers in the range of 500–900 nm with the reflectance of about 50%. Based on the estimation of borides absorption given in [22], the absorptance of TiB₂-Si powder mixture can be roughly assessed to be ~ 45% for materials comprising of 60 vol%Si. Therefore, the composition of 56 wt%TiB₂-44 wt%Si has been chosen for consideration.

2. Materials and Methods

2.1. Self-Propagating High Temperature Synthesis of TiB₂-Si Composite Powder

The commercially pure materials listed in Table 1 were used for the combustion synthesis of the precursor powder. The density of the synthesized powder in its reference state is 1.2 g mL⁻¹. A green mixture of reactants was homogenized in a ceramic mortar for 15 min to prepare the cylindrical samples of 2.1–2.3 g·cm⁻³ density, 30–35 mm height, and 20 mm diameter with the help of uniaxial pressing of 5 kN. Two C-type tungsten-rhenium thermocouples (wire diameter 0.1 mm) covered with a thin layer of boron nitride were positioned in the holes (diameter 1 mm, depth 10 mm) drilled in each sample to record the temperature-time profiles of the combustion process.

Table 1. Precursor powders.

No	Precursor	Particle size, μm	Producer	Purity, %
1	Ti	20	Alfa Aesar	> 99
2	B	< 1	amorphous powder (Sigma-Aldrich)	> 95
3	Si	20	Sigma-Aldrich	> 98

The samples were placed into a reaction chamber CPR-3.5I, which was sealed, evacuated, purged, and filled with argon of 99.999% purity to the pressure of 0.5–2 MPa. To initiate the combustion reaction, a short-term annealing of a tungsten coil (12 V, 1–2 s) positioned on the upper surface of a sample was employed. Maximum combustion temperature (T_c) for each sample was calculated as an average of the maximum for two temperature profiles. The average value of combustion velocity was calculated as $U_c = L \cdot t^{-1}$, where L is a distance between the thermocouples, and t is a time between the signals of the thermocouples. The standard error of measurement for T_c and U_c was $\pm 20^\circ\text{C}$ and 5%, respectively. After the combustion process, TiB₂-Si samples were ground into powder in a laboratory porcelain mortar by pestle and sieved to the fraction of 20–45 μm.

2.2. Selective Laser Melting of TiB₂-Si

The SHS-ed TiB₂-Si powders were printed as solid cylinders (Ø10×5 mm) with the help of SLM apparatus (ReaLizer 50 GmbH, Germany) at the conditions listed in Table 2. The SLM machine employs a high powered continuous-wave laser, which is modulated to function like a pulsed laser system. The Yb:YAG fiber laser with a maximum power of 120 W and wavelength of 1.07 μm was used to solidify the structures under consideration. The process of SLM was performed in the argon atmosphere of high purity (99.999 vol.%) using 1400–2200 mA, at a scanning speed of 80 mm·s⁻¹. Point distance and exposure time were chosen as 10 μm and 125 μs, respectively. As median diameter (D50)

of the synthesized TiB₂-Si particles was measured to be 21 μm , the single layer thickness of 25 μm was chosen accordingly. A “zig-zag” scan strategy, in which the laser pattern rotates by 60° after each layer, was used to fabricate the samples.

Table 2. Laser current and volumetric energy density applied to produce TiB₂-Si solid parts.

No.	Laser Current (mA)	Volumetric energy density (J·mm ⁻³)
Cylinder 1	1400	280
Cylinder 2	1800	360
Cylinder 3	2200	440

2.3. Characterization of Powders and Printed Parts

Standard feedstock characterization techniques for industry are defined in ASTM F3049 (Standard Guide for Characterizing Properties of Metal Powders), which is specified for the powder metallurgy. Nevertheless, these techniques may be used to estimate powders flowability for AM processing. In this work, the flowability was evaluated using the Hall Flowmeter test as a time of 50 g of powder flowing through the $\varnothing 2.5$ mm hole in a funnel according to the EVS-EN ISO 4490:2018 standard. At least five measurements were carried out and values were averaged. The particle size distribution was assessed with the help of laser diffraction using a Malvern Mastersizer 3000.

The bulk density of the prepared composites was measured by Archimedes’ method (Mettler Toledo ME204, Australia) using distilled water as the immersion medium. The theoretical density was estimated assuming a rule of mixture and taking the density of TiB₂ and Si as 4.49 g cm⁻³ and 2.33 g cm⁻³, respectively. Phases analysis of the samples, which were crashed into powders, was performed by X-ray diffraction (XRD) using a Philips X’Pert PRO diffractometer (40 mA, 40 kV, CuK α radiation, $\lambda = 0.1542$ nm, step size of 0.02°, PANalytical, Netherlands) for both powders and as-printed specimens. The XRD peaks were determined from the HighScore Plus software database (ICSD-cross referenced). The relative contents of the phases presented in the structures were estimated by the Rietveld refinement method, which was performed by quantitative analysis of the crystalline phases detected by corresponding XRD patterns (TiB₂-ICDD card No. 04-002-0799 and Si-ICDD card No. 04-014-8844).

For microstructural analysis, a field-emission scanning electron microscope (FE-SEM, Zeiss Evo MA15, Germany) equipped with an EDS (energy dispersive spectroscopy) detector was utilized. Samples were subjected to a hot conductive (resin) mounting, polished with the diamond abrasives down to 0.5 μm finish and coated with a thin layer of Pt for better conductivity.

Micro-hardness measurements were conducted using the Vickers microhardness tester (Indentec 5030 SKV) at a load of 1 kg for a dwell time of 10 s. The measured hardness value for each specimen was taken as the average of 10 indents.

The surface roughness analysis was performed by a Keyence VK-X250 profile-analyzing confocal laser microscope (Keyence Corporation, Osaka, Japan). Maximum height (Sz) and arithmetical mean height (Sa) were averaged for four scanned areas with the dimensions of 500 μm \times 700 μm . Sz is a sum of the maximum peak height and the maximum valley depth in the defined area, and Sa is the average value of the absolute height at each point.

3. Results and Discussion

3.1. Combustion Dynthesis in the Ti-B-Si System

The SHS process is a self-sustained combustion where the heat is generated by the direct synthesis reaction to support combustion wave propagation. The combustion synthesis was performed based on thermodynamic calculations taking into consideration a temperature of TiB₂/Si formation (~ 1430 °C) [15]. The combustion limit was achieved for the mixture with n (Si) = 2.75 regardless to the ambient gas pressure (0.1–2 MPa) and the relative density of the initial specimen (30–60%). Combustion temperature was 100–500 °C lower than the adiabatic temperature, which is

conditioned by large heat losses through radiation and the geometrical set-up of the apparatus. According to the thermodynamic model of the Ti-B-Si system, the formation of TiB_2 is a spontaneous process due to negative Gibbs free energy (ΔG^0_T) at the calculated temperature interval (1500–2000 K). At temperatures exceeding 1700 K, the evolution of titanium monoboride (TiB) and titanium silicides (TiSi) may be considered as the competitive processes to TiB_2 formation. Therefore, the combustion synthesis was performed in the Ti-2B- n Si system at a temperature around 1700 K to avoid by-products and to provide formation of TiB_2 -Si fine particles. An amount of silicon was varied from 1 up to 3 moles to ensure a sufficient quantity of liquid silicon fuse to cover titanium diboride particulates.

Parameters of the combustion process in the Ti-B- n Si mixtures are highly affected by the amount of silicon. At a silicon content of $n = 2.75$ moles, Si occupies ~ 63 vol.% of the Ti-B-Si mixture. Considering the packing geometry of Ti, B, Si particles, a heat transfer at the Ti-B interface mostly occurs through silicon particles during the combustion reaction.

Low thermal conductivity of boron ($0.26 \text{ W}\cdot\text{cm}^{-1}\cdot\text{K}^{-1}$ at 300 K) and silicon ($1.42 \text{ W}\cdot\text{cm}^{-1}\cdot\text{K}^{-1}$ at 300 K and $0.287 \text{ W}\cdot\text{cm}^{-1}\cdot\text{K}^{-1}$ at 1400 K) may result in an inhomogeneous heat transfer and consequent interruption of the CS reaction. Both combustion temperature and velocity decrease with an increase in Si amount in the initial mixture. As illustrated in Figure 1a, a combustion limit is achieved below the melting point of silicon. The combustion wave propagation in the Ti-B-Si system is also governed by the size of the specimen. Pilot batches of $30 \times 40 \times 120 \text{ mm}^3$ provided a complete conversion of reagents attributed to decreased radial heat losses; therefore, the combustion temperature was equal to the adiabatic temperature.

At a lower than stoichiometric amount of the boron source, the formation of titanium silicides ($TiSi$, Ti_5Si_3) and titanium monoboride (TiB) becomes favorable. In terms of preparation of the TiB_2 -Si composite powder, where nano- or ultra-fine scaled TiB_2 particles are held together by molten silicon, the stoichiometric amounts of titanium and boron are relevant at the silicon amount of 2 moles at the combustion temperature over the melting point of silicon. The interaction of the solid Ti particles with the melt of Si or eutectics in the combustion wave was reported in the temperature interval $1330 \text{ }^\circ\text{C} < T < 1670 \text{ }^\circ\text{C}$ [23,24] accompanied by the formation of $TiSi_2$ and $TiSi$. In these works, it was shown that the interaction between the reagents at a temperature of $1330 \text{ }^\circ\text{C}$, which is below all reactant melting points, occurs through the eutectic reaction, $L = TiSi_2 + Si$ (L-liquid). At higher temperatures, the fusion of both silicon and titanium appears to proceed almost simultaneously and results in the formation of Ti_5Si_3 . In the system under consideration, the formation of only trace amounts of $TiSi$ was observed in the non-stoichiometric mixtures. At a high temperature, the amount of silicon is deficient for $TiSi_2$ formation, while at a low temperature, the $TiSi_2$ formation is unlikely. At a temperature below the Si melting point (1414°C), the eutectic reaction ($L = Ti + TiSi_3$) is not detected.

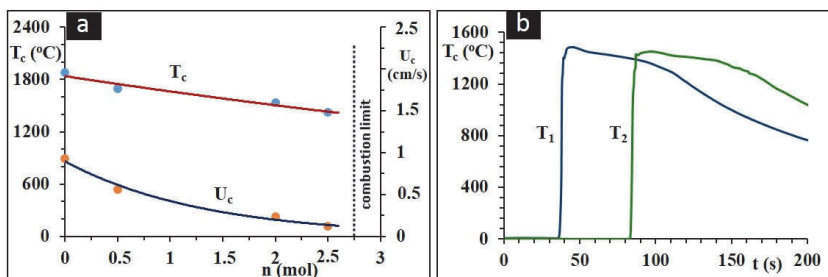


Figure 1. Combustion law for $Ti + 2B + nSi$ system (a), and combustion thermograms of $Ti + 2B + 2Si$ mixture (b) at $P_{(Ar)} = 1 \text{ MPa}$.

The combustion front progresses from top to bottom of the specimen with an undulating movement in the presence of silicon. This combustion mode differs from the smooth planar wave

observed in an undiluted Ti-B. As the combustion temperature is decreased by the silicon diluent, the wave propagation is recorded to be unstable. The undulating movement produces a layered structure in the product as shown in Figure S1. This type of wave propagation is influenced by a liquid phase in the front; thus, the Arrhenius plot of the activation energy for the slow step in the combustion reaction may be determined. The effective activation energy was estimated as 184 kJ assuming no change in the phase composition, Figure S1.

In [25], the effective activation energy of 539 kJ and 318 kJ has been reported for the reaction to form TiB_2 and 410 kJ for the combustion of $\text{Ti} + 1.5\text{B}$ with the formation of the $\text{TiB}_2 + \text{TiB}$ mixture. Inferior values of the activation energy suggest a liquid state mechanism rather than the participation of a solid phase in the combustion reaction in the Ti-B-Si system. During the combustion of the $\text{Ti} + 2\text{B} + 2\text{Si}$ mixture, a wave is propagated with a velocity of $0.24 \text{ cm}\cdot\text{s}^{-1}$ reaching the maximum combustion temperature of $1530 \text{ }^\circ\text{C}$, as in Figure 1b. Figure 2 represents the product after the SHS process demonstrating a highly porous bulk, which easily can be powdered by milling. Figure 2b demonstrates the SEM image of the product of $\text{Ti} + 2\text{B} + n\text{Si}$ ($n = 1.5\text{--}2$ moles) mixture after milling, which represents a collection of particles ($< 50 \text{ }\mu\text{m}$) and their agglomerates ($\sim 0.1 \text{ mm}$). The diameters of the chosen particulates, labelled as $Da1$, $Da2$, $Da3$ in Fig 2c, were estimated to be 436 nm, 349 nm, and 267 nm, respectively, asserting particulates sizes in the 200–450 nm range.

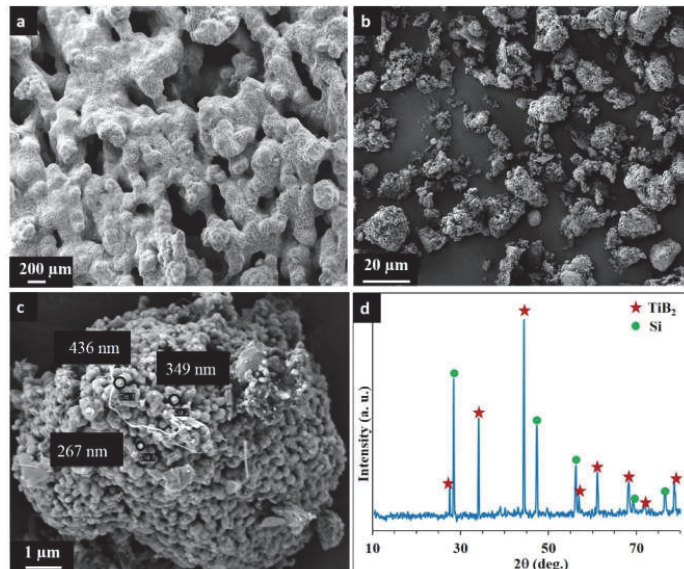


Figure 2. Scanning electron microscope (SEM) images of porous bulk $\text{TiB}_2\text{-Si}$ product produced by SHS (a), the $\text{TiB}_2\text{-Si}$ powder after milling (b and c), and the X-ray diffraction (XRD) pattern of the combustion product (d).

Morphology of the starting powders defines the degree of particles packing throughout the deposited layer. It is well-documented that spherical particles improve the flowability of powders and, therefore, highly affect the quality of the printed product. The SHS method utilized for the preparation of the $\text{TiB}_2\text{-Si}$ feedstock allows for the production of irregular-shaped particles with the required size. The “pomegranate-like” particle represents the collection of nano- and ultra-fine TiB_2 particulates “gluing” together by silicon, as in Figure 2c. This kind of structure may positively contribute to the process of melting/solidification. During laser heating, the ceramic phase TiB_2 , which is tightly embedded in Si without formation of the chemical bonds, attains affinity to viscous

silicon, thus promoting the sintering and compaction process. Figure 2d displays the XRD pattern of the powder revealing the presence of hexagonal titanium diboride (PDF#65-1073) and no spurious phase formation.

The as-synthesized products of Ti+2B+2Si, corresponding to a composition of 56 wt.%TiB₂–44 wt.%Si, were grinded and sieved to the powder fractions of 90 μm, 45 μm, and 20 μm particle size. Particle size distribution (PSD) and shape factor influence flowability; moreover, the quality of the final product is affected by the thickness and uniformity of each powder layer in the build box [26]. The PSD and flowability of the powders are specified in Table 3. The flowability of the powders with a particle size less than 20 μm was negligible, and no meaningful result was recorded. The powders with a particle size in the range of 20–45 μm demonstrated moderate flowability, which nevertheless was acceptable for the SLM processing to ensure a homogenous and non-porous microstructure.

Table 3. Particle size distribution (PSD) and Hall flow rate of TiB₂-Si powders.

Powder size, μ m	PSD, μ m	Hall flow rate (FR _H), s/50g
μ < 20	-	-
20 < μ < 45	Dv10 – 5.48	29.75 ± 0.31
	Dv50 – 21.2	
	Dv90 – 41.4	
45 < μ < 90	Dv10 – 12.3	24.68 ± 0.34
	Dv50 – 57.56	
	Dv90 – 85.4	

3.2. Selective Laser Melting

The structures designed by CAD were adjusted to optimize the SLM procedure in terms of a laser current (I, mA).

The X-ray diffraction pattern of the SLM-ed sample reveals no new or spurious phase formation during the SLM process (Figure 3). The XRD patterns of the SHS powder indicate the presence of 44.1 %Si, while after the SLM process, the amount of Si is calculated to be 43.5%. The difference might be attributed to the accuracy of the Rietveld refinement method; moreover, some evaporation of silicon during the SLM process cannot be avoided at 10–20 mbar pressure. Comparative analysis of the XRD patterns of the powders and printed parts revealed no changes of peak shapes.

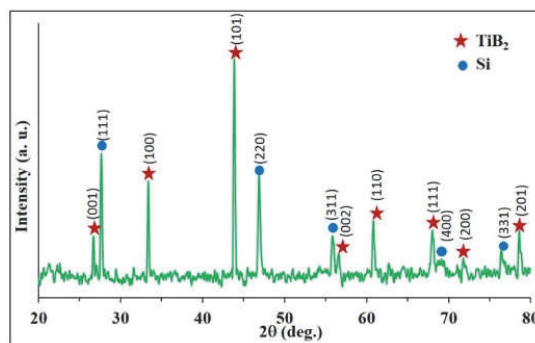


Figure 3. XRD pattern of TiB₂-Si composite after selective laser melting (SLM) (I = 1400mA).

The geometric density of the TiB₂-Si compacts printed at the laser current ranging from 1400 to 2200 mA is specified in Table 4. Taking into consideration the theoretical density of the 56 wt.%TiB₂–44 wt.%Si composite (3.19 g·cm⁻³), the density of the bulks varies from 2.77 to 3.05 g·cm⁻³ corresponding to a relative density range from ~ 87 to ~ 97%. Therefore, a laser current of a high

intensity (at least $I = 2200$ mA) is needed for the production of a high-density material. Cylinder 3, printed at a high energy input, exhibits the highest density due to larger/deeper melt pools, which provides sufficient stitching, melt track overlapping, and improved interlayer connection, resulting in the elimination of the defects caused by lack of fusion. Rapid infiltration of liquid Si into the pores implies readiness of Si to wet TiB_2 , assuming a low contact angle resulting in the restricted removal of TiB_2 solid inclusions from silicon [17]. With an increase in a laser current, the viscosity of liquid silicon decreases, and the flattened silicon inclusions homogeneously occupy the distance between the titanium diboride particles being promoted by the “pomegranate-like” morphology of the feedstock. Due to the “pomegranate-like” structure of the initial powder particles, during the process of cooling, ultra-fine grained TiB_2 particles serve as nucleation centers making the solidification of molten silicon more homogeneous. This prevents the coarsening of silicon grains and decreases the chance of cracking during shrinkage.

Table 4. Density and hardness results of TiB_2 -Si solid parts.

No.	Geom. Density ($g \cdot cm^{-3}$)	Relative Density (%)	Vickers Hardness (GPa)
Cylinder 1	2.77	87	-
Cylinder 2	2.86	90	4.4 ± 1
Cylinder 3	3.05	97	7.6 ± 1

The microstructures of the composites processed at different laser currents are shown in Figure 4 and Figure 5, which demonstrate some reduction in porosity level with increase in the laser current.

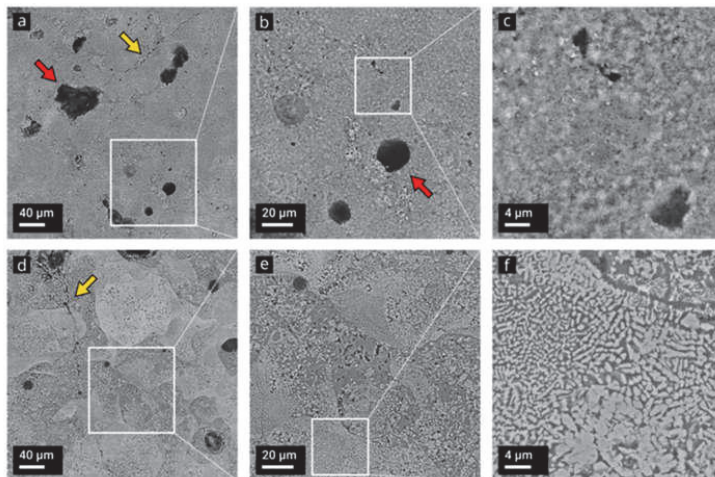


Figure 4. Top surface backscattered electron (BSE) images of TiB_2 -Si bulks printed by SLM at 1400 mA (a–c, Cylinder 1) and 1800 mA laser current (d–f, Cylinder 2). Cracks and pores are pointed out by yellow and red arrows, respectively.

Process induced non-spherical (irregular shaped) porosity was substantiated by an insufficient energy density (or unexpected disturbances during the printing process) that is needed for complete melting of the feedstock and for promoting consolidation (Figure 4a). If insufficient power is supplied, a lack of fusion regions is identifiable by un-melted powder particles visible near the pores. During the powder bed fusion process, the powder layer and some amount of the underlying substrate undergoes melting; however, an insufficient energy input can result in a decrease in molten

pool dimensions and, therefore, in the deficient melting of powder particles and/or re-melting of previously solidified layers.

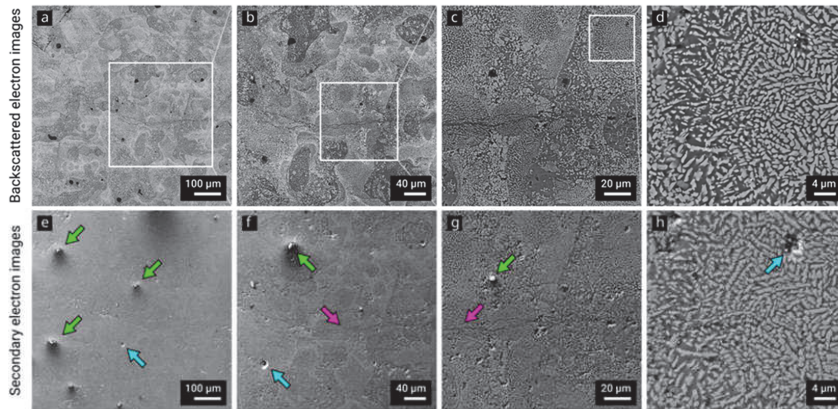


Figure 5. Top surface backscattered electron (a–d) and secondary electron (SE) images (e–h) of TiB₂-Si bulks printed by SLM at 2200 mA laser current. Unmelted or partially melted particles are pointed out by green arrows; pores and surface defects are pointed out by blue and pink arrows, respectively.

With the application of a high-power laser, the powder absorbs higher energy as compared to a solidified layer; hence, the temperature of the molten pool increases above the boiling point leading to the vaporization of silicon and possible formation of a plasma state during the SLM process. This immoderate vaporization of silicon melt causes a different kind of defect in the microstructure of the as-built part due to the interplay between the thermo-capillary force introduced by the temperature gradient, drag force induced by the melt flow, and recoil pressure due to material vaporization. The excessive heat input results in enhanced Marangoni flow and the probability of dragging gaseous species (formed by the turbulence of the molten pool or transferred from the as-synthesized TiB₂-Si) into the molten mass. The pressure applied by the silicon vapors leads to the development of spherical pores, which are well-recognized in Figure 4.

At a higher laser current (1800 mA), the specimens with a smoother surface and a higher density can be produced; however, the surface cracks are found in both samples, as seen in Figure 4d–f. In the system under discussion, the fusion defects were observed in the samples produced at 1400–1800 mA laser current, while the spherical pores are identifiable in all bulks caused by the absorbed gas release or by evaporation of the melt.

Hot-tearing porosity is related to the shrinkage during solidification. Upon cooling through the mushy zone, there is an insufficient amount of material to fill the voids in the solidifying material (Figure 4 a–d). No clearly recognizable large cracks were observed in the probed region of the sample produced at 2200 mA laser current. The overall microstructure mostly consists of the columnar dendritic grains (Figure 5d and h) with an average spacing in the submicron range, which is formed along the deposited direction due to the high thermal gradients of around 10^3 – 10^8 K·s⁻¹ [27].

An influence of the residual porosity onto the hardness is a well-established phenomenon. Expectedly, the hardness of Cylinder 2 is lower as compared to Cylinder 3. For the sample produced at the lowest laser current (1400 mA), no reliable hardness values were measured due to a high porosity.

The microstructures of the 56 wt.%TiB₂–44 wt.%Si composites are comprised of relatively large columnar grains with 2–10 microns length and hundreds of sub-microns of rather equiaxed grains of TiB₂ distributed in the silicon matrix. On the SE images of Cylinder 3, the unmelted or partially melted particles (marked with green arrows in Figure 5) trapped on the surface of the sample are clearly recognizable. The relatively large grooves (marked with blue arrows) are generated by material chips

removal from the surface, and a few surface defects (marked with pink arrows) are either scratches essentially produced during polishing or segregated silicon in a solidified melt pool; however, further detailed analysis is required to prove or disapprove this statement.

EDS mapping of 3D printed solid parts is shown in Figure 6. Figure 6b–e demonstrates the prevailing presence of Si and a minor concentration of Ti atoms (possible formation of TiSi or TiSi₃ is not detectable by XRD) between TiB₂ grains. The images indicate Ti and B atoms mostly located at the TiB₂ sites.

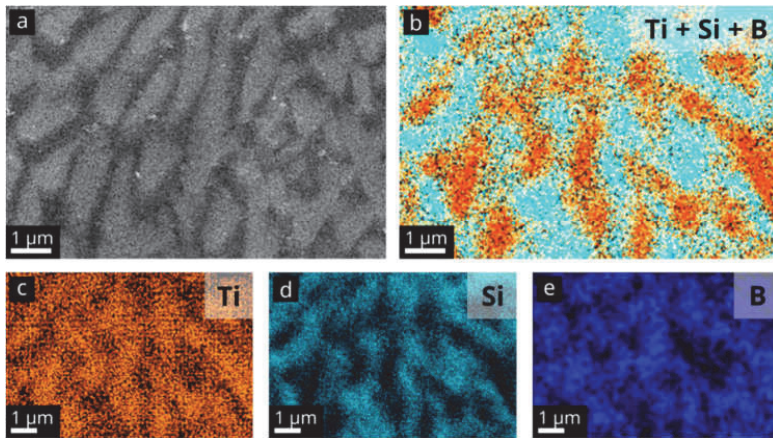


Figure 6. SEM and EDS mapping analysis of selective laser melted TiB₂-Si Cylinder 3 (2200 mA laser current): (a) SEM morphology, and (b–e) is the TiB₂-Si-B map (TiB₂ is marked by orange, Si by blue, top view).

The evaluation of side surface profiles (500 μm × 700 μm) and surface roughness has indicated that both Sa and Sz values are prone to gradually decrease with an increase in the applied laser power, as seen in Figure 7. Cylinder 3 prepared at a laser current of 2200 mA demonstrates the lowest Sa (11.92 μm) and Sz (117.69 μm) for the side surface, i.e., the outer boundary is properly sintered and comprises insignificant surface irregularities.

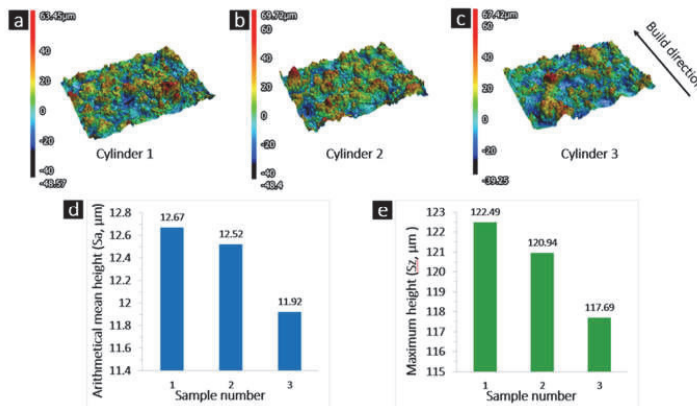


Figure 7. Surface profiles of Cylinders 1, 2, and 3 (a, b, c). Average arithmetical mean height (Sa) (d), and average maximum height (Sz) (e) for Cylinders 1, 2, and 3.

4. Conclusions

For the first time, the “pomegranate-like” structured TiB₂-Si ceramic-metalloid powder feedstock suitable for AM process was prepared by combustion synthesis at a moderate combustion temperature of 1530 °C. As for SHS process, an effective activation energy in the Ti-B-Si system for the slow step was estimated to be 184 kJ. The powder particulates consist of huge amount of nano-scaled TiB₂ particles glued together by silicon. No spurious phases were detected assuming no phase transformation or reaction between the constituents during processing. The powders consisting particles in the range of 20–45 µm demonstrated flowability that may be considered to be acceptable for AM through SLM without any post-treatment/atomization.

The “pomegranate-like” powders demonstrated a high efficiency for manufacturing solid bulks. The 56 wt.%TiB₂–44 wt.%Si composites with a relative density of around 97% and hardness of 6.7 ± 1 GPa (HV1) were processed employing a laser current of 2200 mA and a scanning speed of 80 mm s⁻¹.

Supplementary Materials: The following are available online at www.mdpi.com/2076-3417/10/9/3283/s1, Figure S1. Arrhenius plot for the effective activation energy of the Ti-B-Si combustion reaction.

Author Contributions: Conceptualization – I.H. and S.A.; methodology, S.A. and L.L.; software, L.L.; validation, I.H., S.A., T.M., and L.L.; formal analysis, I.H., T.M. S.A.; investigation, S.A., T.M., and L.L.; resources, I.H. and S.A.; data curation, I.H. and S.A.; writing—original draft preparation, T.M., and L.L.; writing—review and editing, I.H. and S.A.; supervision, I.H. and S.A.; project administration, I.H.; funding acquisition, I.H. and S.A. All authors have read and agreed to the published version of the manuscript.

Funding: This research was funded by the Estonian Research Council, grants number PSG220 and PRG643, and M-ERA.Net project “HOTselflub” N.20097582-CA.

Acknowledgments: This work was supported by the Estonian Research Council grants (PSG220, S. Aydinyan; and PRG643, I. Hussainova) and M-ERA.Net project “HOTselflub”. The authors highly appreciate the European Regional Fund, project number 2014-2020.4.01.16-0183 (Smart Industry Centre), and PhD M. Hussainov from Department of Civil Engineering and Architecture, TalTech, for powder analysis).

Conflicts of Interest: The authors declare no conflict of interest. The funders had no role in the design of the study; in the collection, analyses, or interpretation of data; in the writing of the manuscript, or in the decision to publish the results.

References

1. Rayna, T.; Striukova, L. From rapid prototyping to home fabrication: How 3D printing is changing business model innovation. *Technol. Forecast. Soc. Chang.* **2016**, *102*, 214–224, doi:10.1016/j.techfore.2015.07.023.
2. Kietzmann, J.; Pitt, L.; Berthon, P. Disruptions, decisions, and destinations: Enter the age of 3D printing and additive manufacturing. *Bus. Horiz.* **2015**, *58*, 209–215, doi:10.1016/j.bushor.2014.11.005.
3. Yap, C.Y.; Chua, C.K.; Dong, Z.L.; Liu, Z.H.; Zhang, D.Q.; Loh, L.E.; Sing, S.L. Review of selective laser melting: Materials and applications. *Appl. Phys. Rev.* **2015**, *2*, 041101, doi:10.1063/1.4935926.
4. Gao, W.; Zhang, Y.; Ramanujan, D.; Ramani, K.; Chen, Y.; Williams, C.B.; Wang, C.C.; Shin, Y.C.; Zhang, S.; Zavattieri, P.D. The status, challenges, and future of additive manufacturing in engineering. *Comput. Aided Design.* **2015**, *69*, 65–89, doi:10.1016/j.cad.2015.04.001.
5. Sing, S.L.; Yeong, W.Y.; Wiriya, F.E.; Tay, B.Y.; Zhao, Z.; Zhao, L.; Tian, Z.; Yang, S. Direct selective laser sintering and melting of ceramics: A review. *Rapid Prototyp. J.* **2017**, *23*, 611–623, doi:10.1108/RPJ-11-2015-0178.
6. Bourell, D.; Kruth, J.P.; Leu, M.; Levy, G.; Rosen, D.; Beese, A.M.; Clare, A. Materials for additive manufacturing. *CIRP Ann.* **2017**, *66*, 659–681, doi:10.1016/j.cirp.2017.05.009.
7. Travitzky, N.; Bonet, A.; Dermeik, B.; Fey, T.; Demut, I.F.; Schlier, L.; Schlordt, T.; Greil, P. Additive Manufacturing of Ceramic-Based Materials. *Adv. Eng. Mater.* **2014**, *16*, 729–754, doi:10.1002/adem.201400097.
8. DebRoy, T.; Wei, H.L.; Zuback, J.S.; Mukherjee, T.; Elmer, J.W.; Milewski, J.O.; Beese, A.M.; Wilson-Heid, A.; Ded, A.; Zhang, W. Additive manufacturing of metallic components—Process, structure and properties. *Prog. Mater. Sci.* **2018**, *92*, 112–224.

9. Minasyan, T.; Aghayan, M.; Aydinyan, S.; Liu, L.; Hussainova, I. Combustion synthesis of MoSi₂ based composite and selective laser sintering thereof. *J. Eur. Ceram. Soc.* **2018**, *38*, 3814–3821, doi:10.1016/j.jeurceramsoc.2018.04.043.
10. Varma, A.; Rogachev, A.S.; Mukasyan, A.S.; Hwang, S. Combustion synthesis of advanced materials: Principles and applications, In *Advances in Chemical Engineering*; Academic Press; Cambridge Massachusetts; USA: 1998; Volume 24, pp. 79–226, doi:10.1016/S0065-2377(08)60093-9.
11. Bogdanov, S.P.; Sychov, M.M.; Lebedev, L.A.; Mjakin, S.V.; Gravit, M.V. Core-shell powders for additive manufacturing of articles for underground construction. *Procedia Eng.* **2016**, *165*, 1579–1586.
12. Minasyan, T.; Liu, L.; Holovenko, Y.; Aydinyan, S.; Hussainova, I. Additively manufactured mesostructured MoSi₂-Si₃N₄ ceramic lattice. *Ceram. Int.* **2019**, *45*, 9926–9933, doi:10.1016/j.ceramint.2019.02.035.
13. Telle, R. Analysis of pressureless sintering of titanium diboride ceramics with nickel, cobalt, and tungsten carbide additives. *J. Eur. Ceram. Soc.* **2019**, *39*, 2266–2276, doi:10.1016/j.jeurceramsoc.2019.02.036.
14. Basu, B.; Raju, G.B.; Suri, A.K. Processing and properties of monolithic TiB₂ based materials. *Int. Mater. Rev.* **2006**, *51*, 352–374, doi:10.1179/174328006X102529.
15. Liu, L.; Aydinyan, S.; Minasyan, T.; Baronins, J.; Antonov, M.; Kharatyan, S.; Hussainova, I. Spark plasma sintering of combustion synthesized TiB₂-Si composite. *Ceram. Mod. Technol.* **2019**, *1*, doi:10.29272/cmt.2018.0009.
16. Bertrand, P.; Bayle, F.; Combe, C.; Gœuriot, P.; Smurov, I. Ceramic components manufacturing by selective laser sintering. *Appl. Surf. Sci.* **2007**, *254*, 989–992, doi:10.1016/j.apsusc.2007.08.085.
17. Li, X.P.; Ji, G.; Chen, Z.; Addad, A.; Wu, Y.; Wang, H.W.; Vleugels, J.; van Humbeeck, J.; Kruth, J.P. Selective laser melting of nano-TiB₂ decorated AlSi10Mg alloy with high fracture strength and ductility. *Acta Mater.* **2017**, *129*, 183–193, doi:10.1016/j.actamat.2017.02.062.
18. Attar, H.; Bönisch, M.; Calin, M.; Zhang, L.C.; Scudino, S.; Eckert, J. Selective laser melting of in situ titanium–titanium boride composites: Processing, microstructure and mechanical properties. *Acta Mater.* **2014**, *76*, 13–22, doi:10.1016/j.actamat.2014.05.022.
19. Shishkovsky, I.; Kakovkina, N.; Sherbakov, V. Graded layered titanium composite structures with TiB₂ inclusions fabricated by selective laser melting. *Compos. Struct.* **2017**, *169*, 90–96, doi:10.1016/j.compstruct.2016.11.013.
20. Xia, M.; Liu, A.; Hou, Z.; Li, N.; Chen, Z.; Ding, H. Microstructure growth behavior and its evolution mechanism during laser additive manufacture of in-situ reinforced (TiB+TiC)/Ti composite. *J. Alloy. Compd.* **2017**, *728*, 436–444, doi:10.1016/j.jallcom.2017.09.033.
21. Lee, H.; Lim, C.H.J.; Low, M.J.; Tham, N.; Murukeshan, V.M.; Kim, Y.J. Lasers in additive manufacturing: A review. *Int. J. Precis. Eng. Manuf. Green Technol.* **2017**, *4*, 307–322, doi:10.1007/s40684-018-0069-7.
22. Sani, E.; Meucci, M.; Mercatelli, L.; Jafrancesco, D.; Sans, J.L.; Silvestroni, L.; Sciti, D. Optical properties of boride ultrahigh-temperature ceramics for solar thermal absorbers. *J. Photonics Energy* **2014**, *4*, 045599, doi:10.1117/1.JPE.4.045599.
23. Riley, D.P.; Oliver, C.P.; Kisi, E.H. In-situ neutron diffraction of titanium silicide, Ti₅Si₃, during self-propagating high-temperature synthesis (SHS). *Intermetallics* **2006**, *14*, 33–38, doi:10.1016/j.intermet.2005.04.004.
24. Li, H.P. The numerical simulation of the heterogeneous composition effect on the combustion synthesis of TiB₂ compound. *Acta Mater.* **2003**, *51*, 3213–3224, doi:10.1016/S1359-6454(03)00142-3.
25. Li, H.P. A numerical investigation of the ignition power on micropyretic synthesis of TiB₂. *Model. Simul. Mater. Sci. Eng.* **2005**, *13*, 1331, doi:10.1088/0965-0393/13/8/009.
26. Kennedy, S.K.; Dalley, A.M.; Kotyk, G.J. Additive Manufacturing: Assessing Metal Powder Quality through Characterizing Feedstock and Contaminants. *JMEPEG* **2019**, *28*, 728–740, doi:10.1007/s11665-018-3841-5.
27. Gu, D.D.; Meiners, W.; Wissenbach, K.; Poprawe, R. Laser additive manufacturing of metallic components: Materials, processes and mechanisms. *Inter. Mater. Rev.* **2012**, *57*, 133–164, doi:10.1179/1743280411Y.0000000014.



Curriculum vitae

Personal data

Name: Le Liu
Date of birth: 24.12.1982
Place of birth: China
Citizenship: China

Contact data

E-mail: le.liu@taltech.ee
liule0826@gmail.com

Education

2017-2021 Tallinn University of Technology - PhD
2015-2017 Tallinn University of Technology - MSC (Cum Laude)
2001-2005 Hebei Polytechnic University - BSC

Language competence

Chinese Native
English Fluent
Estonia Basic

Professional employment

2020-2021 Tallinn University of Technology, School of Engineering,
Department of Mechanical and Industrial Engineering,
Engineer
2017-2018 Tallinn University of Technology, School of Engineering,
Department of Mechanical and Industrial Engineering,
Early Stage Researcher

Projects

PRG643 "Bio-replicating Engineering Structures for Tribo-applications (BEST) (1.01.2020-31.12.2024)", Irina Hussainova, Tallinn University of Technology

PUT1063 "Nanonet of ceramic fibers with targeted functionalities (1.01.2016-31.12.2019)", Irina Hussainova, Tallinn University of Technology

IUT19-29 "Multi-scale structured ceramic-based composites for extreme applications (1.01.2014-31.12.2019)", Jakob Kübarsepp, Tallinn University of Technology

Elulookirjeldus

Isikuandmed

Nimi:	Le Liu
Sünniaeg:	24.12.1982
Sünnikoht:	Hiina
Kodakondsus:	Hiina

Kontaktandmed

E-post:	le.liu@taltech.ee liule0826@gmail.com
---------	--

Hariduskäik

2017-2021	Tallinna Tehnikaülikool - PhD
2015-2017	Tallinna Tehnikaülikool - MSC (Cum Laude)
2001-2005	Hebei Polütehnikauülikool - BSC

Keelteoskus

Hiina keel	Emakeel
Inglise keel	Kõrgtase
Eesti keel	Hea

Teenistuskäik

2020-2021	Tallinna Tehnikaülikool, Inseneriteaduskond, Mehaanika ja tööstustehnika instituut, Insener
2017-2018	Tallinna Tehnikaülikool, Inseneriteaduskond, Mehaanika ja tööstustehnika instituut, doktorant-nooremteadur

Projektid

PRG643 "Biojäljendatud tehnostruktuurid triboloogilisteks rakendusteks (1.01.2020-31.12.2024)", Irina Hussainova, Tallinna Tehnikaülikool

PUT1063 "Keraamika kiudude nanovõrgustik sihitute funktsioonidega (1.01.2016-31.12.2019)", Irina Hussainova, Tallinna Tehnikaülikool

IUT19-29 "Mitmeastmeliselt struktureeritud keraamika-baasil komposiitmaterjalid kasutamiseks ekstreemtingimustes (1.01.2014-31.12.2019)", Jakob Kübarsepp, Tallinna Tehnikaülikool

ISSN 2585-6901 (PDF)
ISBN 978-9949-83-745-8 (PDF)